Experimental investigations of the neutron contamination in high-energy photon fields at medical linear accelerators

Dissertation
zur Erlangung des Doktorgrades
des Department Physik
der Universität Hamburg

vorgelegt von

Elin Brunckhorst

aus Hamburg

Hamburg
2009

Gutachter der Dissertation:	Dr. Florian Cremers Prof. Dr. Peter Schleper
Gutachter der Disputation:	Dr. Florian Cremers Prof. Dr. Wolfgang Scobel
Datum der Disputation:	26. Februar 2009
Vorsitzender des Prüfungsausschusses:	Dr. Klaus Petermann
Vorsitzender des Promotionsausschusses:	Prof. Dr. Robert Klanner
Leiter des Department Physik:	Prof. Dr. Jochen Bartels
Dekan der MIN-Fakultät:	Prof. Dr. Arno Frühwald

Abstract

Linear accelerators are usually used for the radiotherapeutic treatment of cancer. If photons with energies above 7 MeV are selected for the treatment, they can exceed the threshold energy for photoneutron production, e.g. for isotopes of the heavy metals of the accelerator head. The produced neutrons contaminate the photon field. For conventional treatment techniques, the contamination is neglected for the patient and only accounted for in radiation protection. However, for techniques with increased beam-on time (e.g. intensity modulated radiotherapy) the additional dose delivery may be no longer negligible. The biological effectiveness of neutrons is substantially higher than that of photons and even a small neutron dose will increase the risk for secondary cancer. Until now only a few direct measurements of the neutron dose inside a photon field and inside a phantom were reported in the literature. The scope of this thesis was to develop a device for the detection of the photoneutron dose inside the high-energy photon field. The device can be applied at any linear accelerator in radiotherapy.

The photoneutron contamination of a Siemens PRIMUS linear accelerator was investigated in detail in its 15 MV photon mode. The experimental examinations were performed with three ionisation chambers (a tissue equivalent chamber, a magnesium chamber and a ^{10}B-coated magnesium chamber) and two types of thermoluminescence detectors (enriched with ^{6}Li and ^{7}Li, respectively). The detectors have different sensitivities to photons and neutrons and their combination allows the dose separation in a mixed neutron/photon field. The application of the ionisation chamber system, as well as the present TLD system for photoneutron detection in high-energy photon beams is a new approach. The TLD neutron sensitivity was found to be too low for a measurement inside the open photon field and the further investigation focused on the ionisation chambers.

The three ionisation chambers were calibrated at different photon and neutron sources and a the borated magnesium chamber showed a very high response to thermal neutrons. For a cross check of the calibration, the three chambers were also used for dose separation of a boron neutron capture therapy beam where the exact determination of the thermal neutron dose is essential. Very accurate results were achieved for the thermal neutron dose component. At the linear accelerator the chamber system was reduced to a paired chamber system utilising the two magnesium chambers, since the fast neutron component was to small to be separated. The neutron calibration of the three chambers could not be applied, instead a conversion of measured thermal neutron signal by the borated chamber to Monte Carlo simulated total neutron dose was performed. Measurements for open fields in solid water and liquid water were performed with the paired chamber system. In larger depths the neutron dose could be determined with an uncertainty of 20 % at two different linear accelerators. The measured thermal neutron dose showed a gaseous distribution and was independent of the field size. Different realistic treatment plans were examined and the additional equivalent neutron dose was found to be less than 30 mSv whole body dose for a whole treatment series. The neutron dose increased with the number of monitor units per applied photon dose.

Finally, the additional neutron dose that results from metal protheses in the beamline during radiotherapy was investigated with Monte Carlo simulations and the paired chamber system. The additional neutron dose was calculated by the simulations to be less than 0.0005 % of the photon dose and was not detectable in the irradiation experiments.

Zusammenfassung

In der strahlentherapeutischen Krebsbehandlung werden üblicherweise Linearbeschleuniger verwendet. Bei Photonenstrahlung mit Energien oberhalb von 7 MeV kann die Schwellenenergie für Photoneutronenproduktion, z.B. der Isotope einiger Metallkomponenten des Beschleunigerkopfes, überschritten werden und die produzierten Neutronen kontaminieren das Photonenfeld. Für konventionelle Techniken bleibt der zusätzliche Dosisbeitrag dieser Neutronen unberücksichtigt, nur in Strahlenschutzberechnungen fließt eine Abschätzung ein. Werden Bestrahlungstechniken mit längerer Strahlzeit (z.B. intensitätsmodulierte Strahlentherapie) angewendet, könnte die zusätzliche Dosisbelastung nicht mehr vernachlässigbar sein. Neutronen haben eine deutlich höhere biologische Wirksamkeit als Photonen und daher trägt auch eine geringe Neutronendosis zur Erhöhung des Sekundärtumor-Risikos bei. Nur wenige direkte Messungen innerhalb des Photonenfeldes und innerhalb von Phantomen sind publiziert. Ziel dieser Arbeit war die Entwicklung eines Detektorsystems, welches die Messung der Neutronenkomponenete innerhalb des Photonenfeldes eines beliebigen Beschleunigers erlaubt.

Die Neutronenkontamination des Siemens PRIMUS im 15 MV Photonenmodus wurde detailliert untersucht. Für die experimentellen Untersuchungen wurden drei Ionisationskammern (eine gewebeäquivalente Kammer, eine Magnesiumkammer und eine ^{10}B-ausgekleidete Magnesiumkammer), sowie zwei Typen Thermolumineszenz-Detektoren (angereichert mit ^{6}Li bzw. ^{7}Li) angewendet. Die Detektoren besitzen unterschiedliche Photonen- und Neutronensensitivität und durch ihre Kombination lassen sich die Dosisbeiträge in einem gemischten Neutronen-/Photonen-Feld separieren. Die Anwendung des Ionisationskammersystems, und des verwendeten TLD-Systems für Photoneutronen-Messungen sind neue Ansätze. Die Neutronenempfindlichkeit der TLD zeigte sich als zu gering für eine Messung im offenen Photonenfeld, daher wurden die folgenden Messungen nur mit Ionisationskammern durchgeführt.

Die drei Ionisationskammern wurden an verschiedenen Photonen- und Neutronen-Quellen kalibriert, wobei sich ein sehr hohes Ansprechen der borausgekleideten Ionisationskammer gegenüber thermischen Neutronen zeigte. Um die Kalibrierung zu überprüfen wurden die drei Kammern in dieser Arbeit auch zur Messung der thermischen Neutronendosis eines Boreinfangtherapie-Strahls genutzt und es wurden sehr genaue Ergebnisse erreicht. Am Beschleuniger wurde das Ionisationskammersystem auf ein Zweikammer-System aus Magnesium- und borausgekleideter Magnesium-Ionisationskammer reduziert, da die schnelle Neutronenkomponente aufgrund ihres geringen Beitrages zum Detektorsignal nicht separiert werden konnte. Die Kalibrierung der drei Ionisationskammern gegenüber Neutronen konnte nicht angewendet werden, stattdessen erfolgte eine Umrechnung von gemessenem thermischen Neutronensignal in Monte-Carlo simulierte Gesamt-Neutronendosis. Messungen mit diesem System wurden in Fest- und Flüssigwasser für offene Felder durchgeführt. In großer Phantomtiefe konnte die Neutronendosis an zwei unterschiedlichen Beschleunigern mit einer Unsicherheit von 20 % bestimmt werden. Die gemessene thermische Neutronendosis zeigte eine gasartige räumliche Verteilung und keine Feldgrößenabhängigkeit. Verschiedene realistische Bestrahlungspläne wurden untersucht und die zusätzliche zu berücksichtigende Äquivalenzdosis durch Neutronen wurde für die gesamte Behandlung zu einer Ganzkörperdosis von kleiner 30 mSv bestimmt. Die Neutronendosis stieg mit der Anzahl der Monitorimpulse pro applizierter Photonendosis an.

Schließlich wurde die zusätzliche Neutronendosis die durch Metallimplantate im Strahlgang verursacht wird mit Monte Carlo Simulationen und dem Zweikammer-System untersucht. Die zusätzlich entstehende durch Simulationen bestimmte Dosis von 0.0005 % der applizierten Photonendosis konnte in entsprechenden Experimenten nicht nachgewiesen werden.

Contents

1 Introduction

The main challenge in tumour treatment using radiotherapy is the application of high doses to the tumorous body regions by simultaneous sparing of the healthy tissue. Several different treatment techniques are established today, the selection is depending on the type of tumour to be treated. Independent of the used technique, accurate dosimetry of the used fields prior to the treatment of a patient is required. Even small scatter doses to the organs at risk (OAR)[1] can elevate the probability to induce secondary cancer [1]. Precise knowledge of these small dose components is therefore necessary.

One way of irradiation is the use of a medical linear accelerator (linac) generating photon beams by bremsstrahlung production. Photon beams with energies higher than 10 MeV are preferred if doses should be delivered to larger depths (e.g. for the treatment of prostate cancer) and to enhance the skin sparing. For photon energies above a threshold of approximately 7 MeV, photonuclear reactions of the heavy metals of the accelerator head lead to the production of unwanted neutrons that contaminate the photon field. Neutrons have a substantially higher biological effectiveness than photons, therefore even a small number of neutrons can lead to a non-negligible dose component [2].

Unwanted neutrons in high-energy photon beams are usually considered negligible for radiotherapy patients using conventional techniques, they are taken into account for radiation protection purposes only. However, if precision radiation treatments like intensity modulated radiation therapy (IMRT) are used, the leakage and neutron radiation increases, as these techniques require longer beam-on times. It is predicted in the literature that the additional dose due to the produced photoneutrons is proportional to the beam-on time [3] and there is an ongoing discussion whether these techniques should be used at all utilising high-energy photons [4]. At present only a few direct measurements of the neutron component and especially inside a phantom could be performed up to now. The ratio between photon fluence and neutron fluence is about $\phi_\gamma/\phi_\mathrm{n} = 10^5$ and the detectors which can be used to obtain either neutron or the gamma dose only, are often sensitive to the other component present in the beam as well. These factors prevent the separation of both, gamma and neutron dose component and therefore mixed n,γ fields require at least the use of two detectors, one of which is sensitive to the photon component only and one to both components.

The goal of this work was to develop a system for the simple and fast determination of the photoneutron contamination at any desired linac. The suitability of an ionisation chamber system and a thermoluminescence detector (TLD) system had to be investigated. These detection systems are made of materials such as ^{10}B and ^{6}Li, which have high thermal neutron cross sections. The ionisation chamber system was expected to allow fast and pointwise separation of the neutron contamination in the photon beam and has already been used for dose

[1] For abbreviations see also the chapter 'Abbreviations' on page 99.

separation in a fast neutron beam [5, 6]. The application of the chambers and the present TLD system for photoneutron detection is a new approach.

In addition to the neutrons produced in the accelerator head, (heavy) metal implants in the patient give rise to photoneutrons and could affect the therapy. The number of patients with metal hip protheses that undergo radiotherapy is more and more increasing, up to 4 % of all patients already have an implant. Only a few direct measurements and Monte Carlo simulations of the additional dose due to the photoneutrons are reported. In this thesis Monte Carlo simulations will be used to estimate the additional neutron dose generated by the presence of a prothesis and the capabilities of an ionisation chamber system for low neutron dose measurements will be investigated.

The question whether an ionisation chamber system is capable to separate the dose components of an epithermal neutron beam used for boron neutron capture therapy (BNCT) will be dealt with. In a therapeutical neutron field, photons from the $^{1}H(n,\gamma)^{2}H$ capture reaction at hydrogen atoms in the patient or photons from the neutron source itself deliver a non-negligible dose contribution. The three dose components of interest are (1) thermal neutron dose, (2) epithermal and fast neutron dose and (3) photon dose. All three components are in the same order of magnitude and their separation requires three detectors of each different neutron and photon sensitivity. The thermal neutron dose component is of vital interest in the dosimetry of a BNCT beam, as the boron enriched tissue in the patient has a high cross section for these neutrons. A borated ionisation chamber will be used as a new approach for an exact detection of the thermal neutrons.

In **Chapter 2** the physical basics of photons and neutrons fields, radiation sources relevant for this thesis and the biological importance of their discrimination are described. The essential dosimetric quantities are introduced and the used dosimetric devices are discussed in **Chapter 3**. Formalisms for the dose separation of different mixed fields using these detection devices are presented. In **Chapter 4** the calibration procedure of the detectors to photons and neutrons of different energies and the obtained results are shown. In **Chapter 5** the validation of the calibration and the suitability of a specific detector system at an epithermal neutron beam are presented. In the central part of this thesis, **Chapter 6**, two detection devices, an ionisation chamber system and a thermoluminescence detector system, for the photoneutron separation in a high-energy photon beam are explored first. Monte Carlo simulations of a specific medical linear accelerator provided fundamental characteristics and the suitability of both detection devices for the experimental verification is validated. Thereafter the use of the ionisation chamber system for continuous measurements and the examination of special realistic treatment plans of radiotherapy patients is illustrated and the capability of the system to be used at any desired linac in radiotherapy is discussed. In **Chapter 7** the problem of the influence of metal protheses on the neutron dose is tackled. Finally, in **Chapter 8** all results are summarised and an outlook on improvements and further fields of application for the developed detection system is given.

2 Photons and neutrons

To understand the dosimetry of mixed n,γ fields some fundamental knowledge of photons and neutrons is necessary. Therefore the physical basics of photon and neutron interactions, their production and biological effectiveness are explained first to the extent needed here.

2.1 Photon interactions

Ionising radiation consists of direct and indirect ionisation. Indirectly ionising radiation is radiation of chargeless particles and therefore includes photon radiation. Interaction of particles without charge and the surrounding matter is rare compared to that of charged particles. The ionisation is primarily performed by secondary charged particles. Photon radiation emerges from several processes: characteristic X-rays, resulting from electron transitions between atomic shells, bremsstrahlung, resulting from electron-nucleus Coulomb interactions and γ-rays, resulting from nuclear transitions, etc. The types of interaction with matter are the same for all, as each of the mentioned types consists of photons. Photons may be considered as electromagnetic waves with a wavelength

$$\lambda = \frac{hc}{E_\gamma}, \tag{2.1}$$

where h is the Planck's constant, c is the speed of light and E_γ is the energy of the photon. Photons can interact electromagnetically with shell electrons, nuclei or other electromagnetic fields either elastically (preserving λ) or inelastically (changing λ). The three following types are the main interactions. Their dependences on the atomic number Z and their dependences on the energy E_γ differ considerably:

1. Photoelectric effect, $\sim \mathrm{Z}^4$, $\sim E_\gamma^{-3}$ ($E < 511\,\mathrm{keV}$), $\sim E_\gamma^{-1}$ ($E > 511\,\mathrm{keV}$)
2. Compton effect, $\sim \mathrm{Z}$, $\sim E_\gamma^n$ ($0.5 < \mathrm{n} < 1$)
3. Pair production, $\sim \mathrm{Z}^2$, $\sim \log(E_\gamma)$ ($E > 1022\,\mathrm{keV}$)

The Compton effect is the predominant interaction effect in the therapeutic energy range of the used photons here ($\overline{E} \sim 2$ – $4\,\mathrm{MeV}$, see Figure 2.1).

The probability for photonuclear reactions is much smaller than that for other photon interactions. The photonuclear reaction (γ,n) is the interaction of a photon with the nucleus. The photon energy has to be larger than the binding energy of the last neutron in the nucleus. It results in an emission of a neutron and in most cases a transformation of the nucleus into a radioactive reaction product:

$$\mathrm{X}_\mathrm{Z}^\mathrm{A}(\gamma, \mathrm{n})\mathrm{X}_\mathrm{Z}^{\mathrm{A}-1}. \tag{2.2}$$

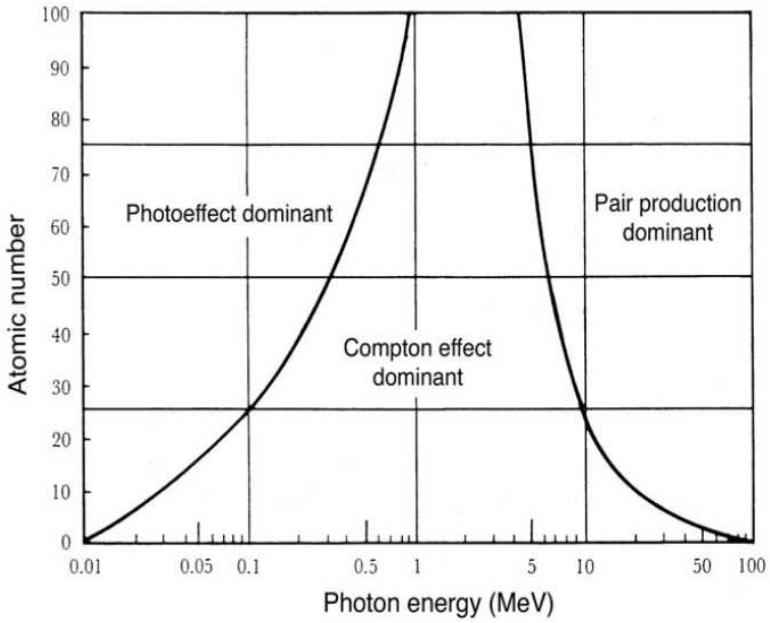

Figure 2.1: Regions of the dominance of each of the three main forms of photon interaction with matter [2].

2.2 Neutron interactions

Neutrons are massive particles without charge. These characteristics allow the neutrons to travel relatively free in matter even at very low energies. Neutrons are classified with respect to their energy (see Table 2.1).

denotation	**energy**
thermal neutrons	less than 0.5 eV
intermediate neutrons	0.5 – 10 keV
fast neutrons	10 keV – 20 MeV
relativistic neutrons	more than 20 MeV

Table 2.1: The classification of neutrons is done with respect to their energy.

A neutron can have several types of interactions with a nucleus. An interaction may be one of two major types, scattering or absorption. The cross sections of the interactions vary with neutron energy and with the target nucleus, sometimes in a dramatic way.

Scattering events can be subdivided into elastic and inelastic scattering. In elastic scattering the total kinetic energy of the neutron and nucleus is unchanged by the interaction. Inelastic scattering is similar to elastic scattering except that the nucleus undergoes an internal rearrangement into an excited state from which it eventually releases radiation when returning

to its ground state.

Instead of being scattered by a nucleus, the neutron may be absorbed or captured. A variety of emissions may follow. The nucleus may rearrange its internal structure and release one or more gamma quanta. Charged particles may also be emitted, the more common ones are protons, deuterons and alpha particles. Three capture reactions are of special interest here: (a) radiative capture by hydrogen ^{1}H, (b) (n,p) reaction by nitrogen ^{14}N and (c) thermal neutron capture by boron ^{10}B.

(a) Radiative capture by hydrogen:
In this case an incoming neutron is bound to the proton, forming deuterium. The binding energy is released as a single photon of 2.23 MeV energy:

$$^{1}\mathrm{H}(\mathrm{n},\gamma)^{2}\mathrm{H} \tag{2.3}$$

(b) (n,p) reaction by nitrogen:
Nitrogen captures thermal neutrons and releases a proton of 580 keV energy. This reaction is the major contribution to the KERMA factor[2] of thermal neutrons in tissue leaving a ^{14}C nucleus, which is a beta emitter with a half life of 5730 years:

$$^{14}\mathrm{N}(\mathrm{n},\mathrm{p})^{14}\mathrm{C} \tag{2.4}$$

(c) Boron thermal neutron capture:
^{10}B (20 % abundance in natural boron) has a high cross section to thermal neutron capture. The compound nucleus is instable and decays instantly into an alpha particle and a lithium nucleus. The following decay reaction occurs in 93.9 % of all collisions:

$$\mathrm{n} + {}^{10}\mathrm{B} \longrightarrow {}^{7}\mathrm{Li}^{*} + \alpha \qquad Q = 2.314\,\mathrm{MeV} \tag{2.5}$$

$$^{7}\mathrm{Li}^{*} \longrightarrow {}^{7}\mathrm{Li} + \gamma \qquad E_{\gamma} = 480\,\mathrm{keV} \tag{2.6}$$

Momentum conservation causes a distribution of the released energy Q in inverse proportion to their masses, i.e. roughly 1/3 to 2/3 ($E_{\mathrm{Li}} = 0.84\,\mathrm{MeV}$, $E_{\alpha} = 1.47\,\mathrm{MeV}$).

In the remaining 6.1% of incidence the photon is not emitted:

$$\mathrm{n} + {}^{10}\mathrm{B} \longrightarrow {}^{7}\mathrm{Li} + \alpha \qquad Q = 2.796\,\mathrm{MeV} \tag{2.7}$$

and the kinetic energies are $E_{\mathrm{Li}} = 1.01\,\mathrm{MeV}$ and $E_{\alpha} = 1.77\,\mathrm{MeV}$.

This reaction releases high LET (linear energy transfer) particles with a short penetration range in human tissue and is used in BNCT treatments to receive a dose boost in areas enriched with ^{10}B.

[2] see Chapter 3.1, eq. 3.7.

2.3 Sources for mixed n,γ fields

Different sources for photon or neutron radiation exist. In some cases both, photons and neutrons, are present in a therapeutic radiation field. Two specific sources for these mixed neutron/photon fields which are of interest for this work are described in the following sections.

2.3.1 Nuclear reactors

Free neutrons do not occur naturally as they are unstable with an average life time of about 15 minutes and cannot be accelerated like charged particles nor easily stored. Therefore neutrons have to be produced in nuclear reactions with photons or charged particles. Frequently used sources are the DD (d + d $\rightarrow$ ^{3}He + n) and DT (d + t $\rightarrow$ α + n) reactions and the neutron induced fission in nuclear reactors.

Nuclear reactors usually use ^{235}U and ^{239}Pu as fuel for the fission process. In slow-neutron reactors the fuel absorbs a thermal neutron and converts into an excited compound nucleus. The compound nucleus decays on a time scale 10^{-16} s or less with a high decay width for the fission into two (excited) fragments. The Q value of this process is in the order of 200 MeV, a substantial fraction of which is carried by the fragment as kinetic energy. Their excitation energy is released by neutron emission, gamma emission and β decay. The originally fast neutrons can be moderated to thermal energies by water, graphite, or heavy water and start in a subsequent chain reaction the fission process again.

Fast neutrons can also be used for radiotherapy treatment for instance in boron neutron capture therapy (BNCT), for which the fast neutrons are moderated to epithermal energies first and become thermal inside the patient. However, the neutron beam is already contaminated by photons originating from the source; moreover the neutrons will also be captured in the hydrogen of the human tissue and induce additional photon emission. In this thesis the High Flux Reactor (HFR) in Petten, The Netherlands, was used as a source, therefore the main principle of the reactor and its BNCT facility will be described in the following section.

High Flux Reactor, Petten/The Netherlands

The High Flux Reactor in Petten, The Netherlands, is a powerful multi-purpose research and test reactor and is owned by the Institute for Energy (IE) of the Joint Research Centre (JRC) of the European Commission (EC). Low enriched uranium is used for the fission process. The HFR has 20 in-core and 12 poolside irradiation positions, plus 12 horizontal beam (HB) tubes. The BNCT facility consists of one of these beams (HB11) and an irradiation room with a patient and facility monitoring area (see Figure 2.2).

A suitable beam for BNCT should have (i) an energy of less than 10 keV to avoid possible high doses by proton recoil, (ii) a gamma and a fast neutron component of each approximately 1.0 Gy and (iii) an adequate fluence of thermal neutrons resulting from the moderation of epithermal neutrons in tissue to allow a patient treatment in a reasonable amount of time. To achieve these characteristics, a specially designed filtered neutron beamline has been installed consisting of materials placed inside the beam tube between the reactor and the patient treatment position. The filter materials and thicknesses to produce the radiation beam char-

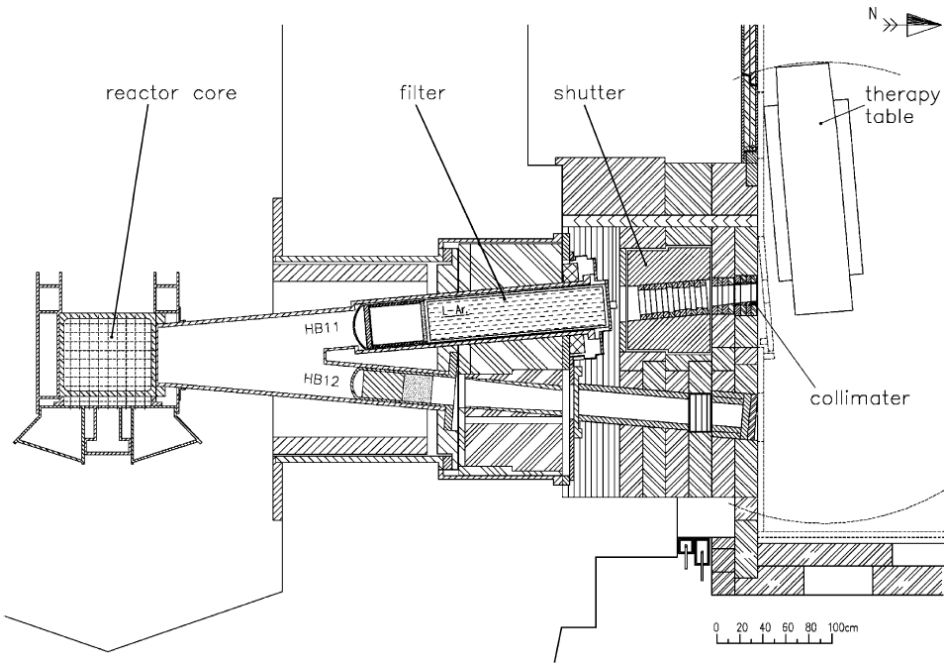

Figure 2.2: Horizontal cross section of beam channel HB11 [7].

acteristics consist of: 15 cm Al; 5 cm S; 1 cm Ti; 0.1 cm Cd; and 150 cm liquid Air. The therapy position is 5.5 m from the reactor core. The mean neutron energy of the beam is 10.4 keV. The epithermal neutrons thermalise in the tissue of the patient and interact with the boron containing tissue via the boron neutron capture process [8].

2.3.2 Medical linear accelerators

Today the most common beam source for external radiotherapy is a medical linear accelerator (linac). In general, modern linacs can be used in two operation modes, electron mode and photon mode. As only the high-energy photon mode is of interest in this thesis, the electron mode is not presented here.

For the photon mode electrons originating from an electron gun are accelerated and directed onto a target, which usually consists of gold or tungsten. The target creates bremsstrahlung photons which can be collimated and used for therapy purposes. In the accelerator head, several components are made of materials with a high cross section to photonuclear interactions. Photoneutrons are produced if the photon energy reaches a threshold of approximately 7 MeV, depending on the material. These neutrons contaminate the photon field. The important components of the linear accelerator for photoneutron production will be explained in detail in the following section.

Siemens PRIMUS, 15 MV photon mode

The investigated linac in this thesis is a Siemens PRIMUS (see Figure 2.3) installed at the University Medical Center Hamburg-Eppendorf. The Siemens PRIMUS delivers electron and photon radiation. In the photon mode, the user can select photon radiation with a maximum

Figure 2.3: The medical linear accelerator Siemens PRIMUS, studio still.

energy of 6 MeV or 15 MeV. As the threshold energy for photoneutron production is about 7 MeV, only the 15 MV mode[3] is of interest here.

Thermal primary electrons are extracted from a heated cathode, used as electron source. The emitted electrons are first accelerated electrically towards an anode. Afterwards, the electrons are entering the horizontal accelerating cavity waveguide where high-frequency electromagnetic field waves are used for further acceleration to an energy of 15 MeV maximum. The Siemens PRIMUS uses a klystron as a radiofrequency power source. The klystron requires high voltage (≈ 100 kV), high current (≈ 100 A), and short duration (≈ 1 s) pulses that can only be produced by a pulsed modulator. Therefore the accelerator works in pulsed mode. The horizontal beam has to be directed in vertical direction to treat the patient. The Siemens PRIMUS machine uses a 270° bending magnet for this purpose. A 270° bending magnet deflects the electrons achromatically independent of their energy. Special 'energy slits' inside the magnet can work as an energy filter which block the electrons having larger or less energy than the target energy. At the Siemens PRIMUS the bending magnet has physical dimensions of approximately 40 cm × 25 cm × 25 cm and consists of steel and copper with an outer tungsten and lead shielding.

In the next step the electrons are directed to a 1 mm thick target disc made of tungsten to create the bremsstrahlung photons. The cooling of the target is achieved by a special copper mounting which is in contact with the cooling water. A primary tungsten collimator is located directly underneath the target and defines the maximum field size. It absorbs the photons that were scattered out of the treatment field. Also housed in the primary collimator, is an aluminium absorber. Its main purpose is to absorb remaining high-energy electrons. As the spectral distribution of bremsstrahlung photons has an angular dependence, the dose distri-

[3]The photon beam consists of a spectrum of energies, the maximum energy is approximately equal to the maximum energy of the primary electrons. Thus a 15 MV beam will produce photons of no more than about 15 MeV.

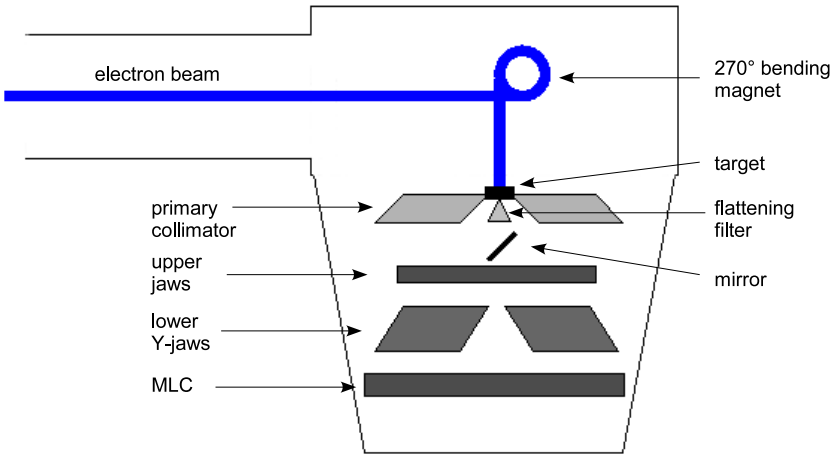

Figure 2.4: The main components of a linac head.

bution has a strong peak at the central axis. A flattening filter, housed inside the primary collimator allows the creation of a flat dose profile. This filter scatters the photons, absorbs low energy photons and therefore hardens the beam. Furthermore, it reduces the overall intensity of the photon beam. The Siemens PRIMUS flattening filter is made of steel. Afterwards the photon beam is collimated by focussing so-called Y-jaws and a focussing multileaf collimator (MLC) made of tungsten to create an individual field geometry. Two ionisation chambers are installed in the beam axis to monitor the radiation. The unit of their signal is the monitor unit (MU). The usual definition is that 100 MU comply to the dose of 1 Gy in the dose maximum in water with a source-surface-distance (SSD) of 100 cm. The mean energy of the photons at SSD 100 cm is about 4 MeV. A schematic plot of the relevant linac head components is shown in Figure 2.4.

The components consisting of materials with high atomic numbers in the accelerator head have a high cross section for photonuclear reactions. Figure 2.5 shows the cross sections for photonuclear reactions for materials of the PRIMUS head. It can be seen in Figure 2.6 that the main elements of the organic tissue have substantial lower cross sections and start at higher energies. Therefore their contribution to the total photoneutron production in a radiotherapy with 15 MV photons is negligible.

2.4 Biological effectiveness of photons and neutrons

The ability of radiation to produce biological damage varies for different types of radiation. The relative biological effectiveness (RBE) compares the dose of a certain radiation to the dose of a standard radiation, such as ^{60}Co γ-rays. The RBE is mainly used in radiobiology.

$$\mathrm{RBE} = \frac{\text{Dose of standard radiation to produce a given biological effect}}{\text{Dose of test radiation to produce the same biological effect}} \tag{2.8}$$

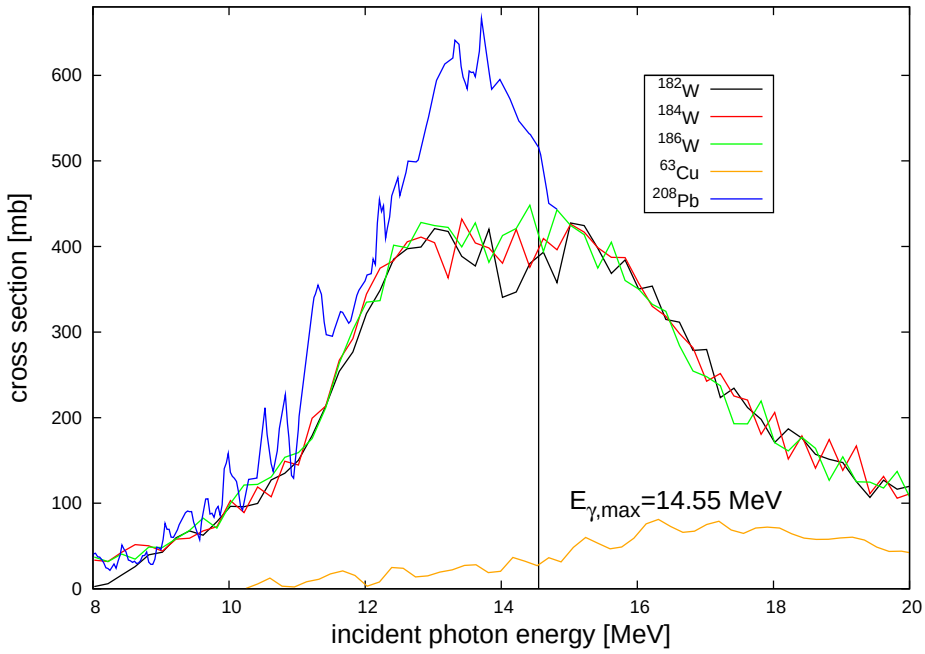

Figure 2.5: Photonuclear cross sections (γ,xn) for selected materials. Values were taken from the EXFOR database of the Nuclear Energy Agency [9]. The maximum photon energy of the studied Siemens PRIMUS is marked by the vertical solid line.

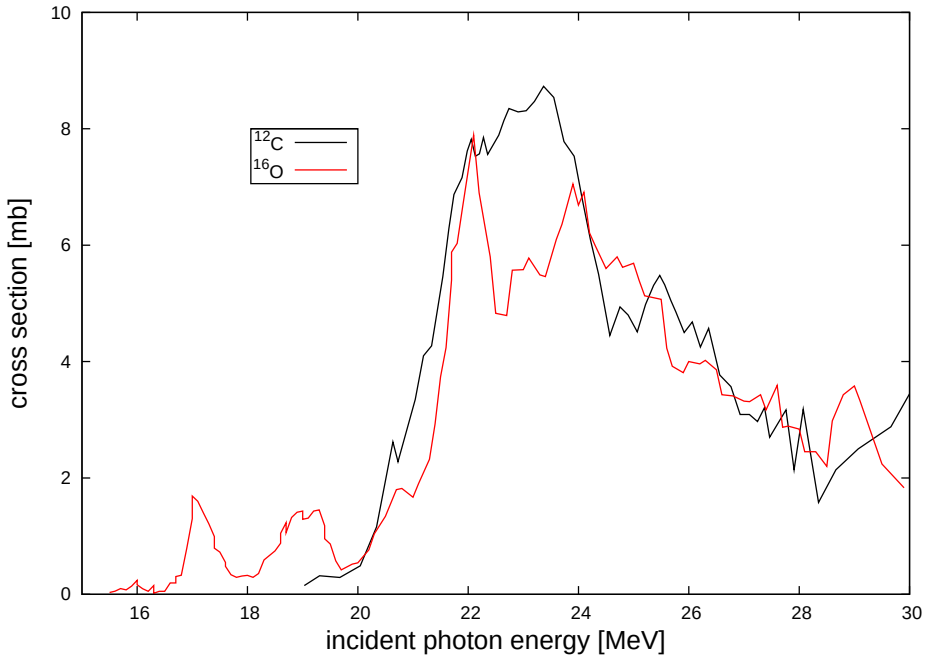

Figure 2.6: Photonuclear cross sections (γ,xn) for carbon and oxygen. Values were taken from the EXFOR database of the Nuclear Energy Agency [9]. The cross sections are negligible for energies below 15 MeV.

The RBE varies not only with the type of radiation but also with the type of cell or tissue, biologic effect under investigation, dose, dose rate and fractionation. As therefore several RBE factors exist, the factor is not suitable for a radiobiological model that can be used for radiation protection purposes. To account nevertheless for the different biological effectiveness, a radiation quality factor w_r is used, which is independent of most of the described factors. It relates the biological effectiveness of a certain type of radiation to the biological effectiveness of photons (quality factor = 1).

type of radiation	**energy**	**quality factor** w_r
photons, electrons	all energies	1
neutrons	less than 10 keV	5
	10 keV – 100 keV	10
	100 keV – 2 MeV	20
	2 MeV – 20 MeV	10
	more than 20 MeV	5
protons	all energies	5
alpha particles	all energies	20

Table 2.2: Quality factors w_r for different types of radiation used to account for their different biological effectiveness.

The higher effectiveness of neutrons in contrast to photons is shown in Table 2.2. Therefore even small contributions from neutrons can deliver a non-negligible dose component. The mean energy of the neutrons produced at the studied linac in this thesis is in the energy range of 0.5 to 1 MeV (see Chapter 6.1). For neutrons within this energy range the quality factor is the highest with a value of 20. Thus a separation of neutrons and photons in a mixed field is necessary. In the next chapter the procedure and the formalism for the dose separation will be explained.

3 Dosimetry of mixed n,γ fields

Dosimetry of mixed n,γ fields requires the separation of the field components. For the quantitative description of the interactions of each of the components the main terms of clinical dosimetry have to be introduced first.

3.1 Dosimetric quantities for clinical dosimetry

The following quantities are used to describe a monoenergetic ionising radiation beam: particle fluence and energy fluence.

The particle fluence ϕ is the number of particles dN incident on a sphere per cross sectional area dA:

$$\phi = \frac{dN}{dA} \tag{3.1}$$

The unit of particle fluence is m^{-2}.

The energy fluence ψ is the radiant energy dR incident on a sphere per cross sectional area dA:

$$\psi = \frac{dR}{dA} \tag{3.2}$$

The unit of energy fluence is $\mathrm{J\,m}^{-2}$.

Almost all realistic photon or particle beams are polyenergetic and the above defined quantities need to be adapted to such beams. They are defined as follows:

$$\Phi_E(E) = \frac{d\Phi}{dE}(E) \tag{3.3}$$

and

$$\Psi_E(E) = \frac{d\Psi}{dE}(E) \tag{3.4}$$

where $\Phi_\mathrm{E}(\mathrm{E})$ and $\Psi_\mathrm{E}(\mathrm{E})$ are notations for the spectral particle fluence and the spectral energy fluence, respectively.

The main purpose of clinical dosimetry is to measure the absorbed energy E_abs of a given radiation per unit mass. This quantity is called absorbed dose D.

$$D_\mathrm{mat} = \frac{dE_\mathrm{abs}}{dm_\mathrm{mat}} = \frac{dE_\mathrm{abs}}{\rho_\mathrm{mat} \cdot dV} \tag{3.5}$$

The SI unit of dose is Gray ($1\,\mathrm{Gy} = 1\,\mathrm{J\,kg}^{-1}$). All dose values depend on the absorber material. In clinical photon dosimetry absorbed dose to water is frequently used as a reference.

For indirect ionising radiation an additional term is used in dosimetry called the KERMA. It stands for **K**inetic **E**nergy **R**eleased per unit **MA**ss. It is defined as the mean kinetic energy transferred from the indirectly ionising radiation to the secondary charged particles per unit mass dm:

$$K_{\mathrm{mat}} = \frac{dE_{\mathrm{trans}}}{dm_{\mathrm{mat}}} = \frac{dE_{\mathrm{trans}}}{\rho_{\mathrm{mat}} \cdot dV} \tag{3.6}$$

The unit of the KERMA is Gy.

The KERMA factor $K(E)$ is the kinetic energy of charged secondary particles released per unit mass per unit fluence of monoenergetic particles.

$$K_{\mathrm{mat}}(E) = \frac{dE_{\mathrm{trans}}}{dm_{\mathrm{mat}} \cdot \phi} = \frac{dE_{\mathrm{trans}}}{\rho_{\mathrm{mat}} \cdot dV \cdot \phi} \tag{3.7}$$

The unit of the KERMA factor is $\mathrm{Gy\,m^2}$. KERMA and KERMA factors are no direct estimations for the absorbed dose, as secondary particles can deposit energy outside of the measuring volume. If a charged particle equilibrium (CPE) exists and no losses due to bremsstrahlung occur, the following equation will be valid:

$$D_{\mathrm{mat}} \overset{\mathrm{CPE}}{=} K_{\mathrm{mat}} = \int_0^\infty K(E)\Phi_E(E)dE \tag{3.8}$$

3.2 Quantities for radiation protection

For radiation protection an equivalent dose H is defined. The unit of equivalent dose is Sievert (Sv). The equivalent dose is derived from absorbed dose but weighted with the quality factor w_{r} (see Chapter 2.4) for the radiation type.

$$H_{\mathrm{mat}} = w_{\mathrm{r}} \cdot D_{\mathrm{mat}} \tag{3.9}$$

The relationship between the probability of stochastic effects and equivalent dose is found to depend on the organ or tissue irradiated. This implies that for the same equivalent dose the detriments from the exposure of different organs or tissues are different. To account for these differences, tissue weighting factors w_{t} are needed. The effective dose E is defined as the summation of tissue equivalent doses, each multiplied by the appropriate tissue weighting factor w_{t}.

$$E = \sum_{\mathrm{t}} w_{\mathrm{t}} \cdot H_{\mathrm{mat}} \tag{3.10}$$

3.3 Radiation detectors and dose separation formalism

For the direct or indirect determination of the dosimetric quantities described above different radiation dosimeters can be used. To be used as a radiation dosimeter, the dosimeter must have at least one physical property that is a function of the measured dosimetric quantity and that can be used for radiation dosimetry via a calibration.

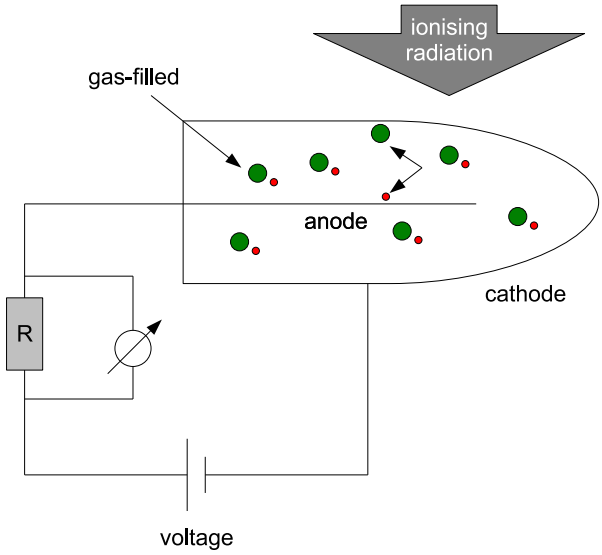

Figure 3.1: The functionality of an ionisation chamber.

For a mixed n,γ field, a system of at least two detectors is necessary. If similar detectors with different sensitivities to neutron and photon radiation are used, the individual beam components can be determined by solving an equation system. For the investigations here, three ionisation chambers and two TLD types were used. Their principle will be introduced in the following sections and the description of the detectors used in this thesis are introduced thereafter. The formalism for the dose separation using the detector signal is explained simultaneously.

3.3.1 Principle of ionisation chambers

A very common dosimeter is the ionisation chamber. Ionisation chambers are gas-filled (e.g. air) detectors in which ionising radiation causes ionisation in the gas, which is detected by applying an electric field to the gas cavity (see Figure 3.1). The collected charge is proportional to the absorbed dose.

For an air-filled ionisation chamber, the measured quantity is the ionisation charge Q produced by radiation in the chamber cavity with the air mass m_{air}. Charge Q and air mass m_{air} are related to absorbed dose in air D_{air} by:

$$D_{\text{air}} = \frac{Q}{m_{\text{air}}} \cdot \frac{W_{\text{air}}}{e} \tag{3.11}$$

where $\frac{W_{\text{air}}}{e}$ is the mean energy required to produce an ion pair in air per unit charge. The conversion of the air cavity dose D_{air} to dose to medium (usually water) D_{w} is based on the Bragg-Gray conditions [2]:

1. the cavity must be small in comparison with the range of charged particles incident on it so that its presence does not perturb the fluence of charged particles in the medium;

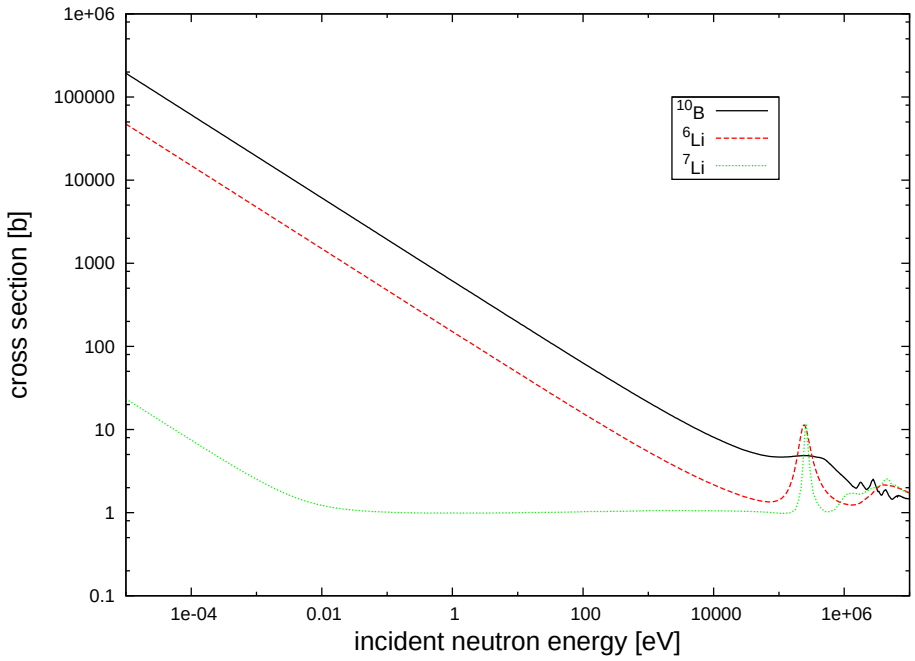

Figure 3.2: Total neutron cross sections for ^{10}B, ^{6}Li and ^{7}Li (ENDF/B-6.8).

2. the absorbed dose in the cavity is deposited only by charged particles crossing it, i.e., photon interactions in the cavity are assumed to be negligible and therefore ignored.

Under these two conditions the dose to an arbitrary medium D_{m} is related to the dose in the air cavity D_{air} as follows:

$$D_{\mathrm{m}} = D_{\mathrm{air}} \cdot (\overline{S}/\rho)_{\mathrm{m,air}} \tag{3.12}$$

where $(\overline{S}/\rho)_{\mathrm{m,air}}$ is the ratio of the average mass collision stopping powers of the arbitrary medium and that of the cavity medium (here air). The mass collision stopping power expresses the average rate of energy loss by a charged particle in all collisions [2].

3.3.2 Special ionisation chambers: TE/TE, Mg/Ar, MgB/Ar chamber

Three specific ionisation chambers were used in this work, a tissue equivalent chamber, a magnesium chamber and a boron coated magnesium chamber. They are denoted as TE/TE, Mg/Ar and MgB/Ar chamber, respectively. Their specifications can be found in Appendix A.

The TE/TE chamber is almost equally sensitive to all dose components (photons, thermal neutrons, epithermal neutrons, fast neutrons) in a mixed n,γ beam and therefore detects total dose. The Mg/Ar chamber is mainly sensitive to the γ-dose and less sensitive to fast neutrons, the sensitivity to thermal neutrons is small, but not negligible for an accurate dose determination. The boron-coated magnesium chamber is very sensitive to thermal neutrons because of the high cross section of ^{10}B to thermal neutrons (see Figure 3.2). The sensitivity to photons and fast neutrons is the same as for the Mg/Ar chamber.

Depending on the composition of the beam, different combinations of these chambers can be

used to separate the dose components. Three possibilities will be introduced here. Neutron and photon contributions can be separated with the well introduced twin chamber system [10, 11]; thermal neutron, epithermal and fast neutron and photon contributions can be separated with a new approach of this thesis, a triple chamber system. A second new approach of this thesis is a paired chamber system to be used for photon fields with very low neutron contamination.

Twin chamber system

The twin chamber system allows for dose separation into gamma contribution and neutron contribution. Both components have to be in the same order of magnitude. The TE/TE chamber is used because it is almost equally sensitive to photons and neutrons. As a neutron insensitive chamber the Mg/Ar chamber is applied. The use of this twin chamber technique has been well established for many years in fast neutron beams [10, 11].

The following equation system has to be solved to determine the dose components:

$$R_{\mathrm{TE}} = h_{\mathrm{TE}} \cdot D_{\gamma} + k_{\mathrm{TE}} \cdot D_{\mathrm{n}}, \tag{3.13}$$

$$R_{\mathrm{Mg}} = h_{\mathrm{Mg}} \cdot D_{\gamma} + k_{\mathrm{Mg}} \cdot D_{\mathrm{n}}, \tag{3.14}$$

where R is the chamber reading corrected for temperature and pressure multiplied by $N_{\mathrm{D,W}}$. $N_{\mathrm{D,W}}$ is the conversion factor of the detector reading into absorbed dose to water obtained during calibration with ^{60}Co radiation (see Chapter 4). D_{γ} and D_n are the dose components from photons and neutrons, respectively. h and k are the relative sensitivities to photons and neutrons compared to the sensitivity to ^{60}Co radiation for each of the chambers.

Triple chamber system

In BNCT treatments it is essential to know the thermal neutron contribution in a mixed neutron/photon field. To separate dose components in these fields, the response of each chamber has to be separated into (1) gamma, (2) epithermal and fast neutron and (3) thermal neutron contribution. A triple chamber system of TE/TE, Mg/Ar and MgB/Ar chamber shall be used for this purpose in this thesis. The following equations, derived from the twin chamber system, have to be solved for dose separation:

$$R_{\mathrm{TE}} = h_{\mathrm{TE}} \cdot D_{\gamma} + k_{\mathrm{TE}} \cdot D_{\mathrm{n}} + i_{\mathrm{TE}} \cdot D_{\mathrm{th}} \tag{3.15}$$

$$R_{\mathrm{Mg}} = h_{\mathrm{Mg}} \cdot D_{\gamma} + k_{\mathrm{Mg}} \cdot D_{\mathrm{n}} + i_{\mathrm{Mg}} \cdot D_{\mathrm{th}} \tag{3.16}$$

$$R_{\mathrm{MgB}} = h_{\mathrm{MgB}} \cdot D_{\gamma} + k_{\mathrm{MgB}} \cdot D_{\mathrm{n}} + i_{\mathrm{MgB}} \cdot D_{\mathrm{th}} \tag{3.17}$$

The notations from the twin chamber system are used with the addition of D_{th}, the dose component from thermal neutrons, and i, the relative sensitivity to thermal neutrons compared to the sensitivity to ^{60}Co radiation for the individual chambers.

Paired chamber system

To estimate the neutron contamination in a photon field, the paired chamber system, using both magnesium chambers, shall be used in this thesis. The neutron flux is very small

compared to the photon flux in this case. The neutron-insensitive magnesium chamber reading is related to the total dose in the usual way:

$$D_{\text{total}} = k_{\text{Q}} \cdot N_{\text{D,W}} \cdot M_{\text{Mg}}, \tag{3.18}$$

where M_{Mg} is the chamber reading corrected for temperature and pressure, $N_{\text{D,W}}$ the cobalt calibration factor and k_{Q} the photon quality correction factor. When a measurement is performed with both chambers under the same conditions, the neutron signal, in form of excess charge, can be calculated in the following way:

$$\Delta Q = M_{\text{MgB}} - k_{\text{rel}} \cdot M_{\text{Mg}} \tag{3.19}$$

k_{rel} considers the different response of both chambers to a pure photon beam.

The resulting value of ΔQ is proportional to the (n,α) reaction rate in ^{10}B at the chamber location. This reaction rate is the convolution of the neutron spectrum and the cross section $\sigma(^{10}\text{B}(\text{n},\alpha))$.

$$\Delta Q = C \cdot \int_0^\infty \sigma(^{10}\text{B}(\text{n},\alpha))(E)\Phi_{\text{n},E}(E)dE, \tag{3.20}$$

where C is a constant and $\Phi_{\text{n},E}(E) = \frac{d\Phi_{\text{n}}(E)}{dE}$ is the differential flux of neutrons with the energy E.

As the boron coated Mg chamber is selectively sensitive to the thermal neutrons, special techniques (e.g. albedo techniques) have to be applied to determine the dose component from faster neutrons. How accurate the determination can be performed has to be studied and will be discussed in Chapter 6.

3.3.3 Principle of thermoluminescence detectors

Another detector type is the thermoluminescence detector (TLD). A TLD measures ionising radiation exposure by measuring the amount of visible emitted light from a crystal in the detector when the crystal is heated. The amount of light emitted depends on the radiation exposure. As the radiation interacts with the crystal it causes electrons in the crystal's atoms to jump to higher energy states, where they stay trapped due to impurities (often magnesium) in the crystal, until heated. Heating the crystal causes the electrons to become thermally excited and drop back to their ground state, releasing a photon of energy equal to the energy difference between the trap state and the ground state.

The theory of thermoluminescence can be explained by the help of the band theory. A schematic illustration of the process is shown in Figure 3.3:
In a pure insulator there are two relevant energy bands: an almost completely filled valence band and an almost empty conduction band. The two energy bands are separated by a forbidden gap with no electronic energy levels. Elevations of electrons from the valence band to the conduction band are allowed and they produce free electrons in the conduction band and free holes in the valence band. The energy difference between the two bands is denoted by the band-gap energy E_{g}. Impurities create new energy levels in the band gap. These defects are capable to trap an electron or a hole. Ionisation transfers electrons from the valence band to

the conduction band, which leads to the presence of significant concentrations of free electrons in the conduction band and free holes in the valence band. Due to their high mobility, the free electrons and holes can migrate in the crystal and are trapped by the impurities or the luminescence centres. When heated the trapped electrons get enough energy to escape from the trap into the conduction band again before they can either be retrapped again, fall radiatively or non-radiatively into the valence band or recombine radiatively with a hole-activated luminescence centre. The light emission from the last processes is called thermoluminescence (TL).

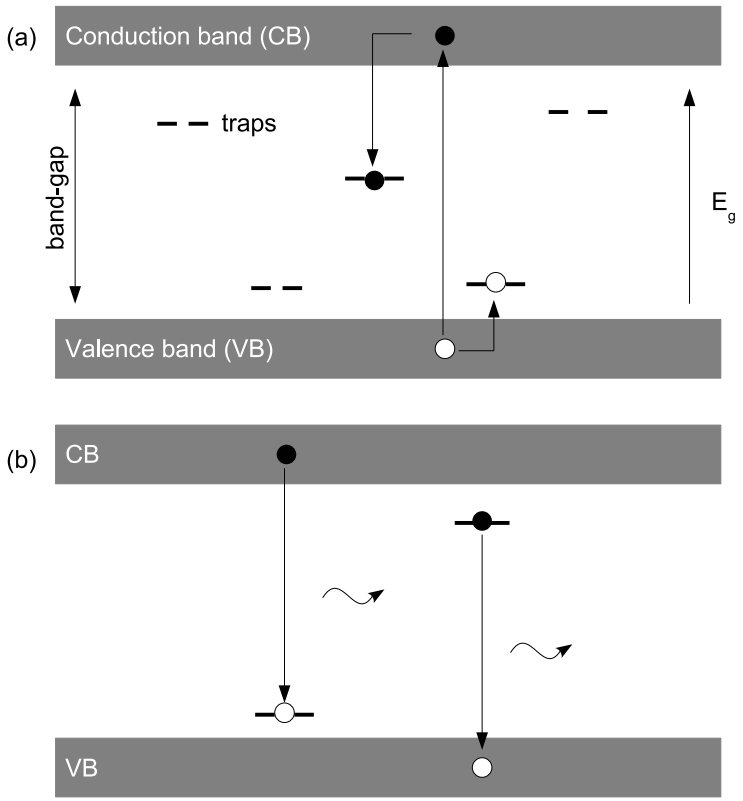

Figure 3.3: The band theory of the thermoluminescence: Irradiation causes excitation (a) of electrons from the valence band to the conduction band, leaving holes and the formation of traps (horizontal lines) within the band gap. The traps are partially filled by electrons (solid circles) and holes (open circles). Heating (b) causes trap release and recombination of free electrons with hole-activated luminescence centres or trapped electrons with free holes and emission of visible light.

A plot of thermoluminescence versus temperature is called glow curve (see Figure 3.4). If the temperature of the TL material is increased, the probability of releasing trapped electrons increases. The TL light increases, reaches a maximum value and then falls to zero as a function of temperature. Since a material may contain several traps at different energy levels, the glow curve will have several glow peaks. The total area under the glow curve can be related to absorbed dose with a proper calibration.

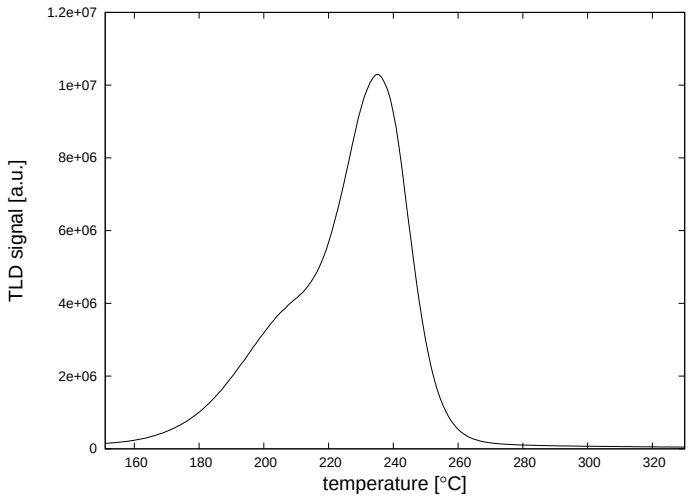

Figure 3.4: The plot of TLD signal versus temperature is called glow curve.

3.3.4 Special TL detectors: MCP-600D and MCP-700D

The thermoluminescence material LiF:Mg,Cu,P is a very sensitive detector material, that is mainly used for radiation protection purposes. Two special types are ^{6}Li- and ^{7}Li-enriched. Using them as a paired system allows separation of dose components in mixed photon/neutron fields as one is sensitive to photons and neutrons and the other one to photons only. Two specific TLD types were used for the investigations of this thesis. Their names MCP-600D and MCP-700D, respectively, refer to their enrichment with ^{6}Li and ^{7}Li, respectively. Their specifications can be found in Appendix B.

Due to the different cross sections for ^{6}Li and ^{7}Li to neutrons (see Figure 3.2) and the similar photon sensitivity of both detectors, both TLD types offer the possibility for dose separation in mixed n,γ fields in the same way as the paired chamber system. However, the neutron sensitivity of the MCP-600D is lower than that of the borated ionisation chamber. Therefore the suitability for its use in beams where the neutron flux is very small compared to the photon flux has to be investigated and is shown in Chapter 6.2.

The TLDs have to be pre-heated in an TLD oven after exposure to delete the low temperature peaks and minimise the fading effect. For TLD read-out, a computer-controlled automatic reader is used. It has a linear, programmable heating system and a cooled photomultiplier tube with associated electronics to measure the TL light output. Heating is performed by hot gas (e.g. nitrogen). After read out, a pre-irradiation heating in the TLD oven is done to be sure that there is no signal remaining on the TLD.

3.4 Phantom materials

Measurements in the therapeutic fields are normally performed in phantoms to simulate the conditions in a human tissue. Water is the standard reference material for photon and electron dosimetry and dose is given as dose to water. However, more practical (homogeneous or inhomogeneous) solid phantoms exist. One common phantom material in Germany is the solid

water named RW3 [12]. Its properties for photon and electron dosimetry in the therapeutic energy range are the same as for liquid water. In radiotherapy the main interaction of photons is the Compton effect. Therefore the electron density of a material and its substitute has to be identical if it is used for photon dosimetry. The electron density (relative to that of liquid water) $\rho_{\mathrm{e,w}}$, the mass density ρ and the chemical composition in percentage by mass for liquid water and RW3 are given below.

$$\mathrm{H_2O} : \rho_{\mathrm{e,w}} = 1.000, \rho = 1.000\,\mathrm{g/cm^3}, \mathrm{H}(11.11\,\%), \mathrm{O}(88.89\,\%)$$

$$\mathrm{RW3} : \rho_{\mathrm{e,w}} = 1.013, \rho = 1.045\,\mathrm{g/cm^3}, \mathrm{H}(7.59\,\%), \mathrm{C}(90.41\,\%), \mathrm{O}(0.80\,\%), \mathrm{Ti}(1.20\,\%)$$

Unfortunately, RW3 is not water equivalent for neutrons. For neutrons a special solid water named A150 exist. The concentration of hydrogen is nearly that of liquid water. This is necessary for the exact simulation of the neutron capture at the hydrogen.

$$\mathrm{A150} : \rho = 1.120\,\mathrm{g/cm^3}, \mathrm{H}(10.1\,\%), \mathrm{C}(77.7\,\%), \mathrm{N}(3.5\,\%), \mathrm{O}(5.2\,\%), \mathrm{F}(1.7\,\%), \mathrm{Ca}(1.8\,\%)$$

Special care has to be taken, if neutron measurements are performed in RW3 as the detector signal does not deliver neutron dose to water. In neutron dosimetry, the dose is often given as dose to muscle tissue, while in BNCT it is given as dose to brain tissue. A special calibration is necessary to assign a measured detector signal in RW3 to dose in water, muscle tissue or brain tissue.

Figure 3.5 shows the RW3 phantom 'Easy Cube' extended to an abdominal shape (Eurome-chanics medical GmbH/Schwarzenbruck, Germany). The phantom has several possibilities to include adaptors for ionisation chambers (specially drilled for each type) and TLDs.

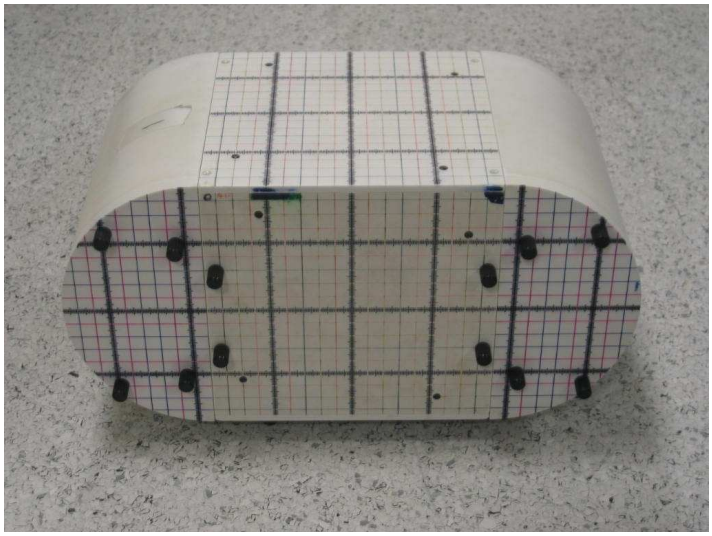

Figure 3.5: Easy Cube extended to an abdominal shape. The phantom is made from RW3 and has dimensions of $36 \times 18 \times 18\,\mathrm{cm^3}$ and is used for some investigations of this thesis.

4 Detector calibration

The determination of the calibration factors below is required before using the detector system in clinical dosimetry. For photon dosimetry, $N_{\mathrm{D,W}}$ and k_{Q} values (eq. 3.18), for mixed field dosimetry h-, k- and i-values (eq. 3.15 – 3.17) have to be determined for each detector individually.

Photon dosimetry

The $N_{\mathrm{D,W}}$ factors for the three investigated ionisation chambers are determined at a Cobalt source and calculated using the measured dose of a calibrated Farmer ionisation chamber ($D_{\mathrm{W,Farmer}}$). The used Farmer chamber from Wellhofer Dosimetry has an active volume of $0.65\,\mathrm{cm}^3$ and has a graphite wall. According to eq. 3.18 $N_{\mathrm{D,W}}$ can be calculated, whereas at a ^{60}Co source $k_{\mathrm{Q}} = 1$ per definition for all chambers.

$$N_{\mathrm{D,W,chamber}} = \frac{D_{\mathrm{W,Farmer}}}{M_{\mathrm{chamber}}}, \tag{4.1}$$

where M_{chamber} is the reading of the chamber to be calibrated.

Neutron dosimetry

The h-values are correlated with the correction for beam quality k_{Q}, known from photon dosimetry. The k_{Q} formalism is described by the IAEA technical reports series no. 398 [13]. If it is assumed that the absorbed dose to muscle tissue and the absorbed dose to water are equivalent for photons, the following equation will be valid:

$$h = \frac{1}{k_{\mathrm{Q}}} \tag{4.2}$$

The experimental determination of the k-values is very difficult and therefore the k-values for the three chambers have been taken from the paper of Waterman *et al.* [14]. A comparison of Monte Carlo simulations with that data was already presented in [15]. Good agreement was achieved for the k-value of the TE/TE chamber. The agreement for the Mg/Ar and the MgB/Ar chamber was acceptable concerning that Waterman *et al.* used a different chamber type and rather small chamber details like the shape of the anode, can have an important influence on the neutron sensitivity.

The i-values can be derived in the following two ways:

(a) Direct approach

In an environment where gamma and fast neutron dose are negligible with respect to the thermal neutron dose, the chamber signal can be expressed as follows. Φ_{th} is the thermal

neutron fluence.

$$M \cdot N_{\mathrm{D,W}} = h \cdot D_\gamma + k \cdot D_\mathrm{n} + i \cdot D_\mathrm{th}; \tag{4.3}$$

$$\text{inserting } D_\gamma = D_\mathrm{n} = 0 \text{ and } D_\mathrm{th} = K(E) \cdot \Phi_\mathrm{th},$$

$$M \cdot N_{\mathrm{D,W}} = i \cdot K(E) \cdot \Phi_\mathrm{th}. \tag{4.4}$$

$$\text{With } M = R(E) \cdot \Phi_\mathrm{th},$$

$$i = \frac{R(E)}{K(E)} \cdot N_{\mathrm{D,W}} \tag{4.5}$$

(b) Indirect approach

An indirect approach can be applied if gamma and fast neutron doses are not negligible compared to the thermal neutron dose. A lithium cap for the chambers is used with the assumption that for photons and fast neutrons the disturbance by this cap is negligible, whereas the thermal neutron flux is reduced by the cap. The reduction factor of thermal neutrons can be estimated by determining the reduction of the response of the MgB/Ar chamber. At the used reference sources (explained in detail in Section 4.1), the MgB/Ar chamber could be considered selectively sensitive to thermal neutrons. Therefore the chamber reading can be expressed as:

$$R = h \cdot D_\gamma + k \cdot D_\mathrm{n} + i \cdot D_\mathrm{th} \tag{4.6}$$

$$R_\mathrm{Li} = h \cdot D_\gamma + k \cdot D_\mathrm{n} + i \cdot \frac{D_\mathrm{th}}{\text{reduction factor}} \tag{4.7}$$

$$i = \frac{R - R_\mathrm{Li}}{(1 - \frac{1}{\text{reduction factor}})} \cdot D_\mathrm{th} \tag{4.8}$$

where the reduction factor is the ratio of the MgB/Ar chamber reading without and with lithium cap (reduction factor = $M_\mathrm{MgB}/M_\mathrm{MgB+Li}$).

4.1 Ionisation chambers

The three ionisation chambers were calibrated at different sources. For photon dosimetry a cobalt source in Petten, The Netherlands, and photon fields of different energies at linacs in the University Medical Center Hamburg-Eppendorf were available. Furthermore a thermal neutron beam at the Low Flux Reactor (LFR) in Petten, The Netherlands and an epithermal neutron beam at the High Flux Reactor (HFR) could be used. A pure thermal neutron beam at the GKSS in Geesthacht (POLDI) was also available. The calibration has already been published in [16].

4.1.1 Calibration to photons

The three ionisation chambers were first calibrated at a cobalt source (^{60}Co: $\mathrm{E}_\gamma = 1.25\,\mathrm{MeV}$, $\mathrm{T}_{1/2} = 5.27\,\mathrm{a}$) against a Farmer chamber. Measurements were performed free-in-air in 50 cm distance to the source, the beam axis of the chambers was positioned perpendicular to the beam axis for each chamber. Due to its calibration the Farmer chamber delivers absorbed dose to water. Table 4.1 lists the obtained $N_{\mathrm{D,W}}$ factors for the three ionisation chambers.

TE/TE chamber	Mg/Ar chamber	MgB/Ar chamber
0.0889 ± 0.0020	0.0686 ± 0.0001	0.0636 ± 0.0003

Table 4.1: $N_{D,W}$ values determined at a cobalt source against a Farmer chamber. Values are given in Gy/nC. The uncertainties are obtained by statistical analysis of a set of measurements ($1\,\sigma$).

h-values were determined for 4 MV, 6 MV and 15 MV photons at linacs. The photon fields were provided by two clinical accelerators installed at the University Medical Center Hamburg-Eppendorf, a Siemens MEVATRON MDX-2 offering 4 MV and 6 MV fields and a Siemens PRIMUS offering 6 MV and 15 MV fields. Each chamber was exposed inside a RW3 phantom in a $10\times10\,\mathrm{cm}^2$ field. A Farmer chamber was used again as a reference. For the 15 MV field a contamination of neutrons is already present and a calibration of the neutron sensitive MgB/Ar chamber was therefore not suitable. The contamination is small enough to be neglected for the TE/TE and the Mg/Ar chamber. The h-value of the MgB/Ar chamber for the 15 MV mode of the Siemens PRIMUS accelerator could nevertheless be estimated as follows. The ratio of of h_{MgB}/h_{Mg} is assumed to be energy independent:

$$h_{MgB}(15\,\mathrm{MV}) = h_{Mg}(15\,\mathrm{MV}) \cdot \frac{h_{MgB}(6\,\mathrm{MV})}{h_{Mg}(6\,\mathrm{MV})} \tag{4.9}$$

All k_Q-values obtained are listed in Table 4.2. The corresponding h-values derived by eq. 4.2 are summarised in Table 4.3. The k_Q-value for the MgB/Ar chamber was derived from the estimated h-value. To calibrate the chambers to the photons at the BNCT beam line at the HFR (HB11 = horizontal beam line No. 11), it was assumed that the neutron contamination in the HB11 beam becomes negligible after passing through 35 cm of water. The ratio of h_{Mg}/h_{TE} was determined to be 1.079 ± 0.005. As neither h_{Mg} nor h_{TE} could be determined separately in the HB11 beam, unity was assumed for h_{TE}, as also suggested by other authors [17, 18].

beam quality	TE/TE chamber	Mg/Ar chamber	MgB/Ar chamber
4 MV, MDX-2	0.992 ± 0.005	0.955 ± 0.005	1.023 ± 0.005
6 MV, MDX-2	0.983 ± 0.005	0.947 ± 0.005	1.010 ± 0.005
6 MV, PRIMUS	0.977 ± 0.005	0.938 ± 0.005	1.004 ± 0.005
15 MV, PRIMUS	0.946 ± 0.005	0.901 ± 0.005	0.964*

Table 4.2: k_Q-values for the three chambers obtained for different photon energies at linear accelerators. The value with * could not be determined directly as there is a non negligible neutron contamination in the high energy photon field. It has been calculated by the estimated h-value using the assumption in eq. 4.9. The given uncertainties are estimated values concerning all systematic errors.

beam quality	TE/TE chamber	Mg/Ar chamber	MgB/Ar chamber
HB11	1.000 ± 0.005	1.079 ± 0.005	1.008 ± 0.005
4 MV, MDX-2	1.008 ± 0.005	1.047 ± 0.005	0.977 ± 0.005
6 MV, MDX-2	1.017 ± 0.005	1.055 ± 0.005	0.990 ± 0.005
6 MV, PRIMUS	1.024 ± 0.005	1.066 ± 0.005	0.996 ± 0.005
15 MV, PRIMUS	1.057 ± 0.005	1.110 ± 0.005	1.037*

Table 4.3: Summary of the obtained h-values. Values at the HFR have been estimated with the assumption of a neutron free HB11 beam line in larger depths. The value with * is an estimation using eq. 4.9. The given uncertainties result from the uncertainties in the determination of the k_{Q}-value.

4.1.2 Calibration to neutrons

For the calibration of the chamber response to neutron irradiation, three neutron sources were available: (1) a pure thermal neutron beam at the GKSS, (2) the thermal neutron beam at the LFR, and (3) the epithermal neutron beam at the HFR. Their characteristics are described below. KERMA factors for muscle tissue for each spectrum were calculated by convolution of the neutron spectrum (Maxwellian distribution) with the KERMA factor for the individual energies. As the KERMA factors provided by ICRU Report 44 [11] were available at discrete energies only, they were continuously interpolated prior to convolution.

(1) Thermal neutron beam at GKSS (POLDI):
A neutron reference field operated by the Physikalisch-Technische Bundesanstalt (PTB) at the POLDI beamline of the GKSS facility in Geesthacht, Germany, was used for calibration. The beam has been described in detail by Boettger *et al.* [19]. The spectrum at a reference point is described by a Maxwellian distribution with $kT = 22.25\,\mathrm{meV}$ (see Figure 4.1); no neutrons with energies higher than 1 MeV can be detected with a highly enriched ^{238}U fission chamber and a Cd-plate in the beam. Moreover, the gamma dose rate at the reference position measured by Boettger *et al.* [19] is about $2\,\mu\mathrm{Sv/h}$. The average thermal neutron flux is $8.5 \times 10^4\,\mathrm{cm^{-2}\,s^{-1}} \pm 5\,\%$. The KERMA factor for this spectrum is $3.213 \times 10^{-13}\,\mathrm{Gy\,cm^2}$. The calibration measurements for this work were performed free in air at the reference position, with the beam axis perpendicular to the chamber axis.

(2) Thermal neutron beam at LFR:
The LFR beam is a mixed neutron/photon field with a high thermal neutron flux. It is located at the Low Flux Reactor (LFR) of the Petten nuclear facility and is operated by the Nuclear Research and Consultancy Group (NRG). Measurements were performed with a set of three foils consisting of AuAl (1wt% Au), Cu and MnNi (88wt% Mn) encapsulated in rice paper. The foils were analyzed by A. Paardekooper from NRG Fermi-lab at the Petten nuclear facility and the data was provided for this work. The spectrum at the LFR can be described by a Maxwellian spectrum with $kT = 27\,\mathrm{meV}$. The KERMA factor for this thermal spectrum is $2.916 \times 10^{-13}\,\mathrm{Gy\,cm^2}$. The average flux has been determined by foil measurements to be $6.925 \times 10^8\,\mathrm{cm^{-2}\,s^{-1}}$ with a relative uncertainty of 2.5 %. There are only 0.5 % neutrons faster

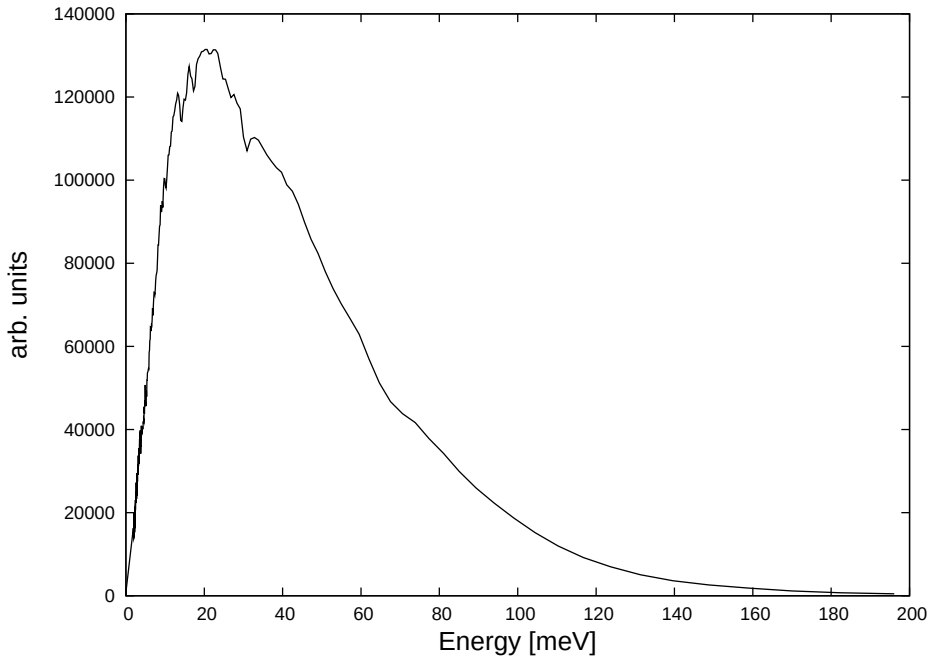

Figure 4.1: Measured neutron spectrum of the PTB reference field POLDI at the GKSS [19].

than thermal. These neutrons are assumed to be epithermal following a $1/E$ distribution. There is a significant contamination of photons, with a dose rate of about 1 Gy/h in the beam [20]. The calibration measurements for this work were set up on a trolley that was inserted into the reactor. The chambers were positioned free in air on this trolley with the chamber axis perpendicular to the beam axis.

(3) Epithermal neutron beam at the HFR:
The HFR has already been described in Chapter 2.3.1. Measurements were performed inside a water phantom at a reference point in 3 cm depth. The average flux of thermal neutrons, determined by foil measurements, is $8.401 \times 10^8\,\mathrm{cm^{-2}\,s^{-1}} \pm 2.5\,\%$. The KERMA factor for the beam with $kT = 45\,\mathrm{meV}$ is $2.283 \times 10^{-13}\,\mathrm{Gy\,cm^2}$. The chambers were positioned again with their chamber axis perpendicular to the beam axis.

Determination of k-values

Waterman *et al.* [14] studied the energy dependence of a TE/TE and a Mg/Ar chamber for neutron energies from 1 MeV to 50 MeV. Epithermal neutron beams have lower energies and obviously lower k-values are needed. Raaijmakers *et al.* [21] studied the k-value for their TE/TE chamber extensively. They determined a value of 0.87 ± 0.03 for the HB11 beam (KERMA-weighted mean energy 10.4 keV). The values are summarised in Table 4.4.

Determination of i-values

The i-values of the MgB/Ar chamber were determined directly, whereas these of TE/TE and Mg/Ar chamber were determined by the indirect method. The reduction factors using a lithium cap were determined with the MgB/Ar chamber by dividing the charge collected

neutron energy	TE/TE chamber	Mg/Ar chamber	MgB/Ar chamber
10 keV (Raaijmakers)	0.87 ± 0.03	-	-
1 MeV (Waterman)	0.96 ± 0.10	0.021 ± 0.002	0.021 ± 0.002
2 MeV (Waterman)	0.96 ± 0.10	0.030 ± 0.003	0.030 ± 0.003
3 MeV (Waterman)	0.96 ± 0.10	0.035 ± 0.004	0.035 ± 0.004

Table 4.4: k-values (and their uncertainties) taken from Waterman *et al.* [14] and Raaijmakers *et al.* [21]. The k-values from Waterman *et al.* for the Mg/Ar chamber is also assumed for the MgB/Ar chamber, as the contribution of ^{10}B is insignificant at high neutron energies.

field	kT [meV]	measured reduction factor
POLDI	22.25	1445.9 ± 0.1
LFR	27	179.5 ± 0.3
HB11	45	42.0 ± 0.1

Table 4.5: Reduction factors of the lithium cap determined with the MgB/Ar chamber in different neutron fields. Uncertainties are a result of the statistical uncertainties in the measured detector response with and without lithium cap.

without cap by the charge collected with cap. The reduction factors are listed in Table 4.5. The lithium cap (^{6}LiF embedded in epoxy resin) for the Mg/Ar and MgB/Ar chamber is of cylindrical design with a minimum wall thickness of 3.5 mm and has an area density of 328 mg cm^{-2} ^{6}LiF.

All obtained i-values are listed in Table 4.6. The MgB/Ar chamber is sensitive to the orientation of the chamber in relation to the direction of the neutrons. Luedemann *et al.* [6] studied this effect and determined a value of 0.835 for the compensation of an isotropic irradiation. Therefore the values from HB11 were divided by 0.835 to compensate for the isotropic distribution of thermal neutrons inside the water phantom.

field	TE/TE chamber	Mg/Ar chamber	MgB/Ar chamber
POLDI	-	-	23150 ± 2000
LFR	2.47 ± 0.05	1.32 ± 0.3	23350 ± 2000
HB11*	-	2.88 ± 0.5*	25950 ± 2000*
mean	2.47 ± 0.05	2.10 ± 0.5	24150 ± 2000

Table 4.6: i-values were determined directly for the MgB/Ar chamber, indirectly for the other chambers. Values marked with * were divided by 0.835. Uncertainties are estimations taking the statistical uncertainties and further systematic errors into account.

4.2 TL detectors

The TLDs MCP-600D and MCP-700D were characterised during this work. The results can be found in Appendix B and were already published in [22].

Calibration to photons

Several TLDs have to be used for a measurement to improve the quality of the datum. Due to the wide spread of the individual response of the detectors, the raw data has always to be corrected for this. Otherwise up to 60 % difference in the sensitivity ($2\,\sigma$) of the MCP-600D will prevent reasonable dosimetry. Therefore a general calibration is not possible. Each TLD has to be corrected for its individual response to a reference radiation first. Exposure to photons with a maximum energy of 6 MV were used for this purpose. The calibration was performed against a calibrated ionisation chamber of the type Wellhofer CC01 with an active volume of $0.01\,\mathrm{cm}^3$. The individual calibration factor for each TLD was applied for all further measurements.

Calibration to neutrons

The TLDs were not available at the time the measurements at the neutron sources in Petten and Geesthacht were performed. Therefore a calibration of the TL detectors to neutrons was only performed in the high-energy photon mode at the linac. The procedure will be explained in Chapter 6.2.

5 Epithermal neutron beams

For BNCT treatments, the knowledge of the thermal neutron component in the used epithermal neutron beam is essential, because the tumorous tissue is enriched with ^{10}B and captures the thermal neutrons. With this procedure a dose boost selectively to the tumorous cells can be achieved. The use of a boron coated magnesium chamber for the dosimetry of BNCT beam is a new promising approach and is investigated in this thesis. These investigations function as an additional cross check of the already obtained ionisation chamber calibration.

5.1 Application of a triple chamber system

The epithermal neutron beam HB11 at the High Flux Reactor (HFR) in Petten, used for boron neutron capture therapy (BNCT), has already been introduced in Chapter 2.3.1. The total absorbed dose in irradiated tissue originates from different components: thermal neutrons, intermediate and fast neutrons and gamma rays. The different biological effectiveness makes a quantitative decomposition necessary to accurately calculate the dose prior to the treatment of a patient. In particular, the determination of the thermal neutron component is essential, as boron-containing tissue has an increased cross section for thermal neutrons.

Detectors which can be used to obtain the neutron or the gamma dose are often also sensitive to the other component present in the beam. Therefore a mixed field requires generally the use of paired detectors. Several authors described the use of a paired-chamber technique that has been well established for many years in fast neutron beams [10, 11]. It should be noted that there are no ICRU recommendations for the mixed-field dosimetry of BNCT. However, recommendations were generated by a large European BNCT-consortium coordinated by the Petten group, Voorbraak *et al.* [23]. Earlier, Raaijmakers and Konijnenberg [17] investigated the dose using TE/TE and Mg/Ar chambers, TLDs and activation foils to separate the components. Rogus *et al.* [24] also used a paired-chamber technique of TE/TE and carbon graphite chambers, as well as gold foils.

As the thermal neutron component is of vital interest in BNCT, the suitability of a triple chamber technique, using TE/TE, Mg/Ar and MgB/Ar chamber, was validated during this thesis. Schmidt and Hess [5] validated a triple chamber technique for a fast neutron beam that consisted of a TE/TE chamber, an unshielded and a shielded GM counter. The MgB/Ar chamber is of interest as it is selectively sensitive to thermal neutrons. This chamber was already investigated by Luedemann *et al.* [6] for fast neutron therapy and was also used in a ^{252}Cf-neutron field [18]. A paired Mg/Ar and MgB/Ar chamber technique for BNCT dosimetry has already been described by Burmeister *et al.* [25], but with a chamber that was not as highly loaded with ^{10}B as compared to the chamber used here (3.6 % vs. 92 % ^{10}B). Therefore the response of their borated chamber to photons and non-thermal neutrons was not negligible.

The calibration of the triple chamber system was described in detail in Chapter 4 and has already been published in [15]. The calibration data was applied for the measurements here. The dose from intermediate and fast neutrons is treated as one component as the division of both is not practical for the present beam. Therefore a separate determination of (1) thermal neutron dose, (2) intermediate and fast neutron dose and (3) gamma dose is performed. The gamma component also contains the gammas from the capture process. The thermal neutron component includes all other secondary particles. Absolute depth-dose distributions, beam profiles and 2-dimensional dose distributions for each of the three dose components for a 12 cm field of the epithermal neutron beam HB11, used for BNCT in the HFR, were measured with the triple chamber system.

A computer-controlled water phantom WP 700 (Wellhofer Dosimetry, Schwarzenbruck/ Germany, see Figure 5.1) was used for the measurements. Its outer dimensions are 64.5 × 67.5 × 56 cm^3. A circular, 12 cm diameter beam collimator was used to form the field. For all measurements, the water phantom was placed at 30 cm distance to the beam exit. The outer wall of the phantom was defined as depth of 0 cm. Due to the lucite wall of the phantom and the holding device of the chamber, the measurements could not be performed at depths below 2.5 cm. The lucite wall thickness of the phantom is 1.5 cm. As the beam is horizontal, it has to pass through the lucite wall. The depth was not corrected for the dosimetric differences of lucite to water. The chambers were always positioned with their axis perpendicular to the beam axis and were preflushed for about 60 minutes before the first measurement was started, with the flow rate was checked during the whole measurement.

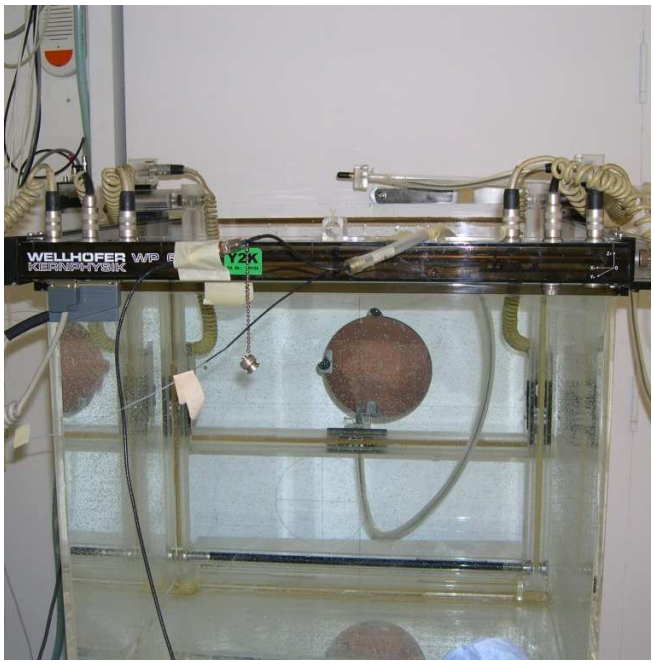

Figure 5.1: Set up of the computer-controlled water phantom WP 700 in the HB11. The circular beam exit behind the water phantom can be seen. The holding device for the chamber can be used for scanning in x-, y- and z-direction.

An absolute dose measurement was performed at a reference depth of 3 cm for each chamber. Thereafter, depth dose rate distributions, beam profiles (in-plane = horizontal) and isodoses were obtained by using the corresponding scanning option in the WP 700 software. The scanning signal was normalised to the signal at the reference point. For the absolute dose measurement, a Farmer electrometer 2570 was used for charge collection and operated with a negative voltage of 250 V. The signal was corrected for temperature and pressure. For the measurements in the water phantom, the electrometer WP 5006 was used. Absorbed dose is given as absorbed dose to muscle tissue [11]. During the measurements, the stability of the beam output was monitored with the beam monitor system of the BNCT facility. As it was stable within 1 % ($2\,\sigma$), no renormalisation was necessary. The measurements were performed with a permanently opened beam shutter. Therefore the opening and closing procedure did not influence the measurements.

The h-, k- and i-factors from Table 5.1 were applied for the chambers (see also Chapter 4). As the MgB/Ar chamber is sensitive to its orientation in relation to the neutron direction, the i-values for the measurement here have been multiplied by the factor 0.835 as recommended by Luedemann *et al.* [6]. It is used to compensate the isotropic distribution of thermal neutrons inside the water phantom.

chamber	h	k	i
TE/TE	1.000	0.96	2.47
Mg/Ar	1.079	0.021	2.41
MgB/Ar	1.008	0.021	21693

Table 5.1: Applied k-, h- and i- values for the TE/TE, Mg/Ar and MgB/Ar chamber.

With these relative sensitivities, the measured beam profiles, depth-dose distributions and isodoses were separated into the different dose components using the formalism introduced in Chapter 3.3.2 (eq. 3.15 – 3.17). As the γ-ray component as well as the fast and intermediate neutron component are negligible for the signal of the MgB/Ar chamber, the formalism is reduced to:

$$D_{\mathrm{th}} = R_{\mathrm{MgB}}/i_{\mathrm{MgB}} \tag{5.1}$$

$$D_{\mathrm{n}} = \frac{h_{\mathrm{TE}}}{h_{\mathrm{TE}}k_{\mathrm{Mg}} - h_{\mathrm{Mg}}k_{\mathrm{TE}}} \cdot R_{\mathrm{Mg}} - \frac{h_{\mathrm{Mg}}}{h_{\mathrm{TE}}k_{\mathrm{Mg}} - h_{\mathrm{Mg}}k_{\mathrm{TE}}} \cdot R_{\mathrm{TE}} + \frac{h_{\mathrm{Mg}}i_{\mathrm{TE}} - h_{\mathrm{TE}}i_{\mathrm{Mg}}}{h_{\mathrm{TE}}k_{\mathrm{Mg}} - h_{\mathrm{Mg}}k_{\mathrm{TE}}} \cdot D_{\mathrm{th}} \tag{5.2}$$

$$D_{\gamma} = \frac{R_{\mathrm{TE}}}{h_{\mathrm{TE}}} - \frac{i_{\mathrm{TE}}}{h_{\mathrm{TE}}} \cdot D_{\mathrm{th}} - \frac{k_{\mathrm{TE}}}{h_{\mathrm{TE}}} \cdot D_{\mathrm{n}} \tag{5.3}$$

The measured depth-dose rates along the central axis are presented in Figure 5.2. Separate curves are shown for thermal neutron dose rate D_{th}, fast and intermediate neutron dose rate D_{n}, and photon dose rate D_{γ}. Figure 5.3 shows the in-plane profiles at a depth of 5 cm.

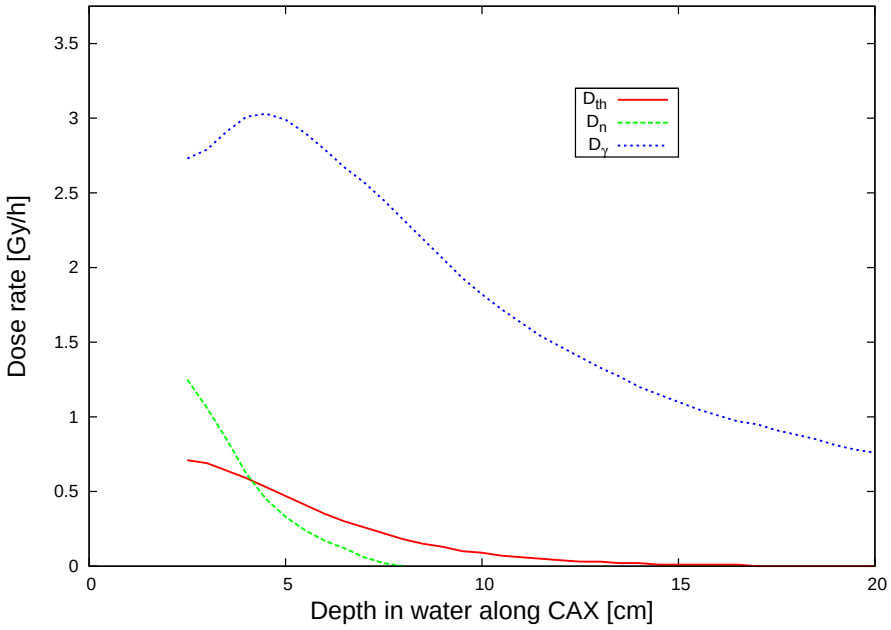

Figure 5.2: Depth-dose rate of the 12 cm field along the central axis measured with the triple chamber system. Dose due to: thermal neutrons D_{th}, fast and intermediate neutrons D_{n} and photons D_{γ}.

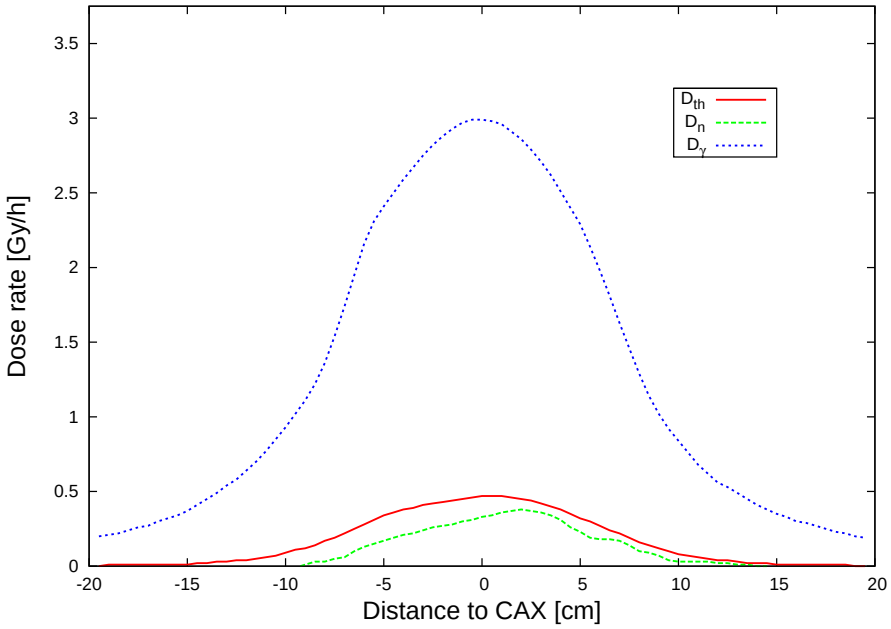

Figure 5.3: In-plane profiles of the 12 cm field at 5 cm depth measured with the triple chamber system. Dose due to: thermal neutrons D_{th}, fast and intermediate neutrons D_{n} and photons D_{γ}.

The isodose scans, that were performed with each of the three chambers, allow for separation of a 2-dimensional dose-rate distribution for thermal neutrons D_{th}, fast and intermediate neutrons D_{n} and photon dose rate D_{γ}. Figure 5.4 shows the horizontal distributions along the central axis.

5.2 Comparison of measured data with published data

Raaijmakers, Konijnenberg and Mijnheer [26] have already published an extensive study of the HB11. They performed measurements in a $30 \times 30 \times 30\,\mathrm{cm}^3$ water phantom with a 0.6 cm PMMA wall. A paired Mg/Ar- and TE/TE-chamber system, as well as activation foils and a PN diode were used as detectors. The phantom-to-beam exit distance was 30 cm, as in the measurements here. Table 5.2 lists the absolute values for ϕ_{th}, D_{γ} and D_{n} at a reference depth of 3 cm for a 12 cm field in comparison to the measured data here. The values (and uncertainties) from Raaijmakers *et al.* were determined from tables and graphs of [26].

	ϕ_{th} [10^8 n cm^{-2} s^{-1}]	D_{γ} [Gy h^{-1}]	D_{n} [Gy h^{-1}]
Raaijmakers *et al.* [26]	7.21 ± 4 %	2.80 ± 4 %	0.52 ± 4 %
this work	8.401 ± 5 %	2.79 ± 10 %	1.06 ± 20 %

Table 5.2: Comparison of absolute measured dose components with data from Raaijmakers *et al.* [26] for all three dose components at a reference depth of 3 cm for a 12 cm field. Uncertainties for this work are estimations taking all statistical and systematic uncertainties into account.

The absolute thermal fluence is 15 % less for Raaijmakers data in comparison to the work here, while the absolute gamma doses are the same within the overall uncertainty. For the fast neutron dose component a very large deviation is present. The measured neutron dose in this work is twice as high as the dose measured by Raaijmakers [26] in 1997.

Figure 5.5 shows the relative comparisons of the percentage depth dose (PDD) curves for all three dose components for a 12 cm field. Each dose component was normalised to its maximum value.

Taking the quoted errors into account, the measured data in this work for the relative thermal fluence is, at least in the high flux region, in accordance with the data from Raaijmakers. The measured percentage gamma depth dose shows a shift of approximately 1 cm to larger depths in comparison to Raaijmakers data indicating a higher mean photon energy. The relative distribution of the fast neutron dose for both is the same within the uncertainty up to 5 cm depth. At larger depths, Raaijmakers obtained a lower gradient.

However, some differences in the measurement conditions of this work and Raaijmakers exist: The absolute thermal neutron fluence at the reference point in Raaijmakers *et al.* is approximately 15 % less than in this work, which can also be expected for the epithermal neutron

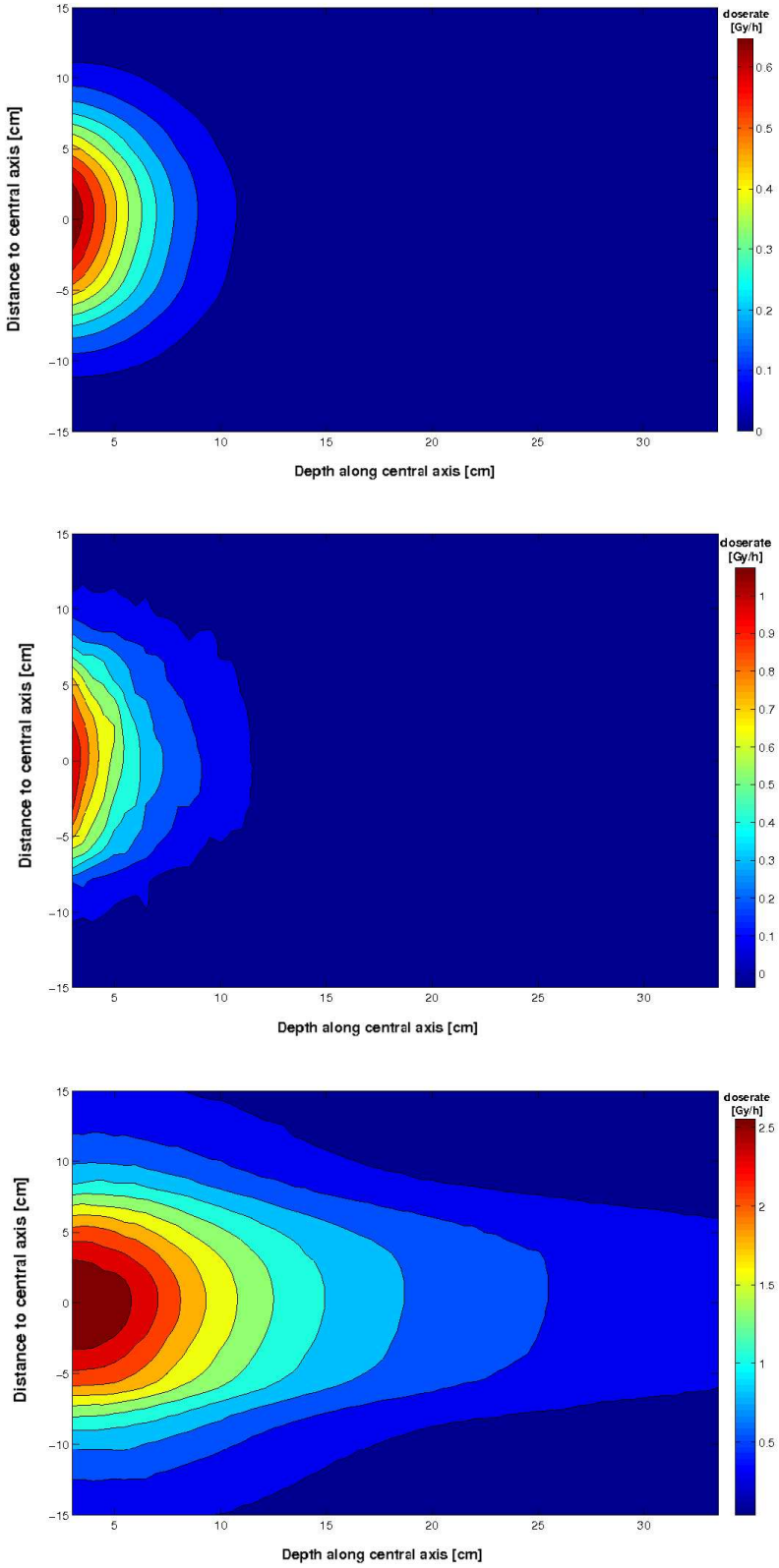

Figure 5.4: 2-dimensional dose-rate distributions due to thermal neutrons (top), intermediate and fast neutrons (middle) and photons (bottom) for a 12 cm field in Gy/h measured with the triple chamber system.

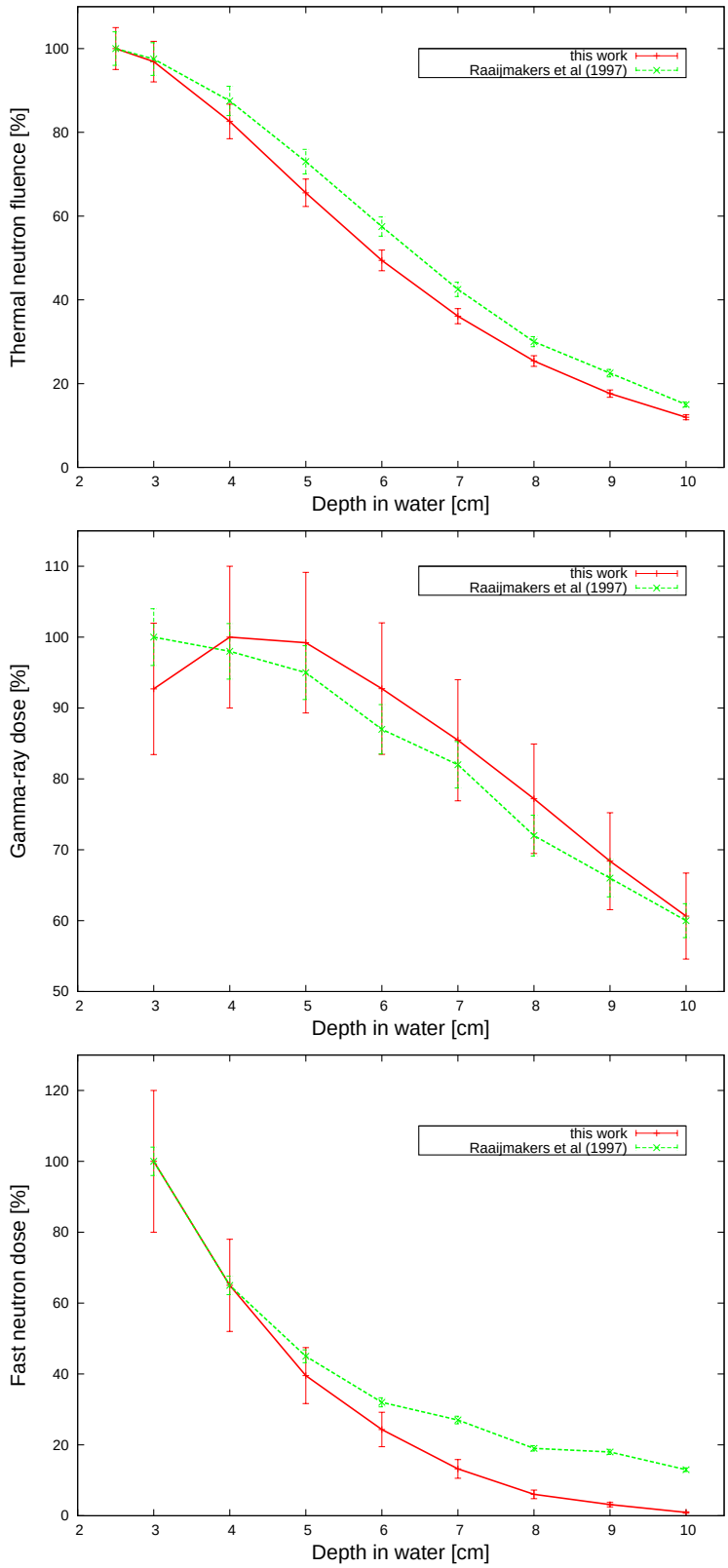

Figure 5.5: Comparison of data from this work with data from Raaijmakers *et al.* [26]. The PDD is shown for the thermal neutron fluence (top), for the gamma dose D_γ (middle) and the fast neutron dose D_n (bottom). Each dose component was normalised to its maximum value.

fluence leading to a higher fast neutron dose. A further reason for a higher fast neutron dose component could be the use of different neutron KERMA factors. In this work dose to muscle tissue is calculated. In Raaijmakers *et al.* it is not specified but it is assumed dose to brain tissue, as the BNCT therapy is mainly used for therapy of brain tumours. The KERMA factors for muscle and brain for the present beam differ by about 4 - 5 % (Raaijmakers *et al.* [21]). Furthermore, Raaijmakers *et al.* applied relative small i-values for the TE/TE and Mg/Ar chambers (see Table 5.3), which they obtained experimentally for their chambers. Higher i-factors for TE/TE and Mg/Ar chamber lead to a larger value of D_{n}.

	$i_{\mathrm{TE/TE}}$	$i_{\mathrm{Mg/Ar}}$
Raaijmakers *et al.* [26]	1.49 ± 0.03	0.48 – 1.26 ± 0.03
this work	2.47 ± 0.6	2.41 ± 0.6

Table 5.3: Comparison of i-values used by Raaijmakers *et al.* [26] and used in this work. Raaijmakers *et al.* studied different Mg/Ar chamber and the range of the determined i-values is given here.

As the thermal neutron distribution can also be considered as a part of the photon source due to the capture process in hydrogen, the gamma dose component is also influenced by a higher thermal neutron fluence. The higher the thermal neutron fluence, the higher is the induced and therefore the total gamma-ray dose component. Additionally the PMMA wall of Raaijmakers' phantom is thinner than that of the phantom used here (0.6 cm to 1.5 cm). Due to the smaller contribution of hydrogen in PMMA compared to water (8.05 to 11.19), the neutrons will thermalise at larger depths and the dose maximum of D_{γ} will be shifted to larger depths (Raaijmakers *et al.* [27]). This is evident as a shift of the measured PDD here to the data of Raaijmakers (see Figure 5.5).

Furthermore, the reactor fuel was changed from highly (93 %) to low enriched (19 %) uranium in between the measurements of Raaijmakers and this measurements and this will probably have an influence on all dose components. Monte Carlo simulations for the specific used set up were performed by the Petten group and first data were provided here. The simulation does not include changes in the reactor source spectrum used for the simulations that might be due to the fuel change from highly to low enriched.

5.3 Comparison of measured data with Monte Carlo simulations

Monte Carlo simulations with MCNPX were performed by the Petten group and the results are used here. The measured data for the depth-dose distribution of all three dose components of this work was compared to simulation data. The comparison is shown in Figure 5.6.

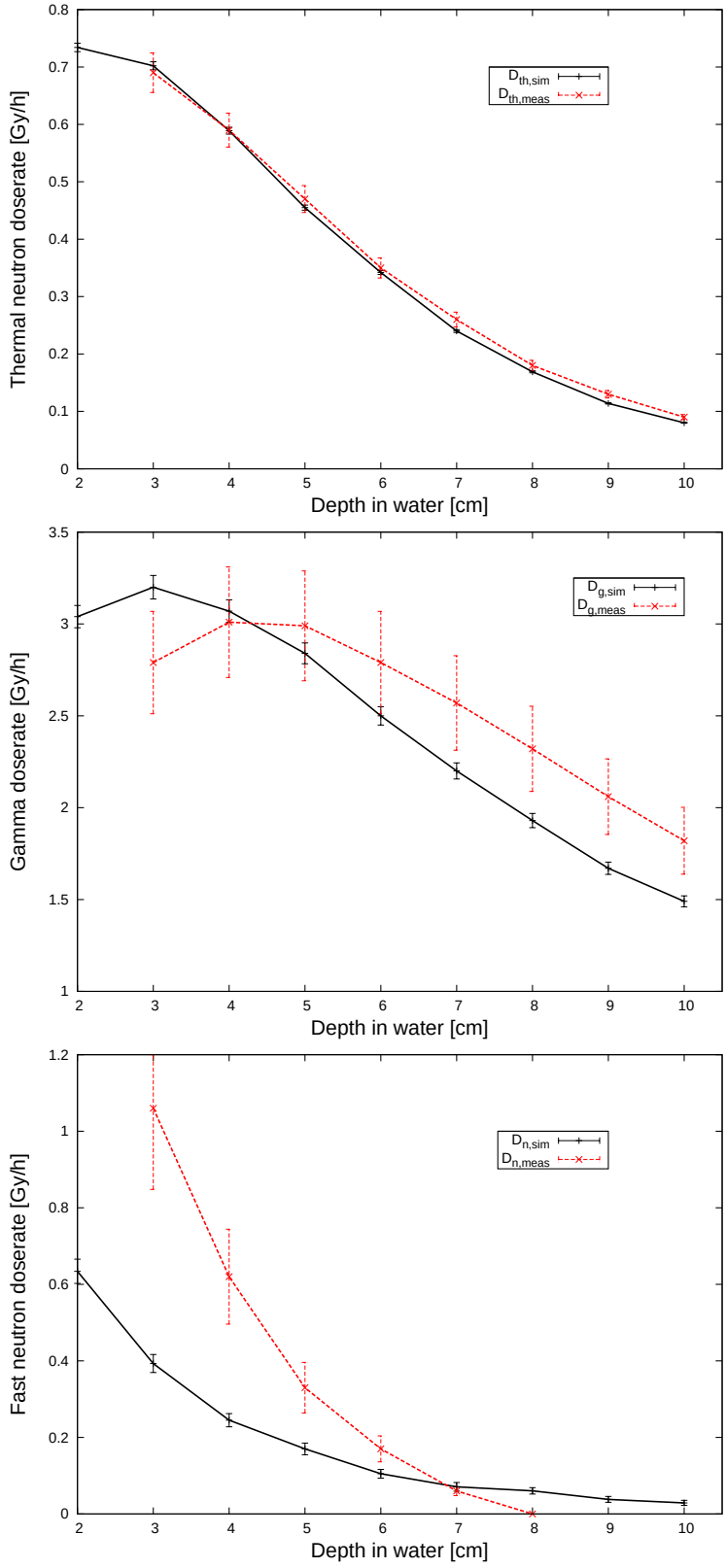

Figure 5.6: Comparison of the absolute measured thermal neutron dose (top), the gamma-ray dose (middle) and the fast/epithermal neutron dose (bottom) of this work with MC simulation data provided by the Petten group.

The measured *thermal* neutron dose agrees well with the simulation data (within 7 %). However, the deviation for the *fast/epithermal* neutron dose is significant. The measured gamma dose shows the same shift as the comparison with the published data from Raaijmakers *et al.*

Calculated and measured fast/epithermal neutron dose and gamma dose have then been summed to a collective dose $D_{\mathrm{n},\gamma}$ for both, simulated and measured data. The comparison is shown in Figure 5.7.

Both curves show the same gradient, however, the measured dose is higher by a constant factor. This indicates a false assumption for the h- and k-factors used here. The k-values have not been provided by Waterman *et al.* [14] for the energy range of the HB11. The published factor from Waterman *et al.* for 1 MeV is used here, even though the mean energy for the HB11 is less. Therefore the uncertainty of the applied k-factor delivers the largest component to the total error.

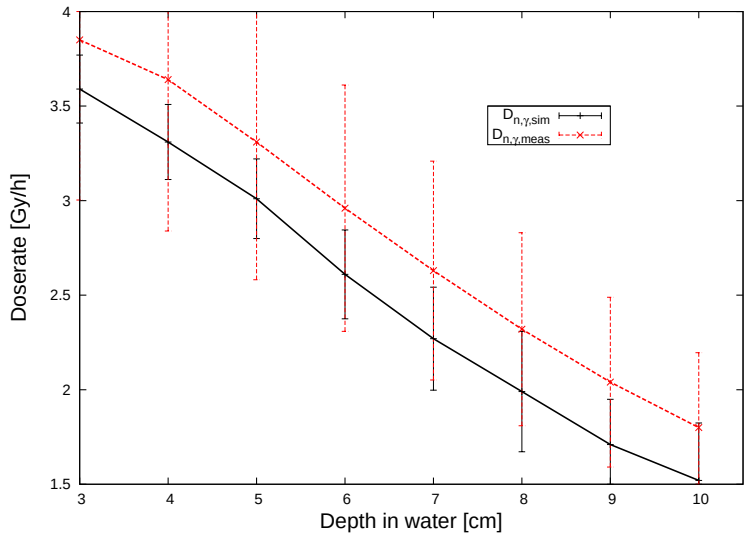

Figure 5.7: Comparison of the measured and simulated collective dose $D_{\mathrm{n},\gamma}$.

In this chapter the triple chamber system utilising TE/TE, Mg/Ar and MgB/Ar chamber was applied to separate the three dose components (thermal neutron dose, fast/epithermal neutron dose and gamma dose) in an epithermal neutron beam and to verify the calibration data that was applied. The beam is used at the HFR in Petten, The Netherlands, for BNCT. The exact knowledge of the thermal neutron dose is essential, because the tumorous tissue is enriched with ^{10}B to capture the thermal neutrons for a precise destruction of the tumour cells. The application of a high loaded (92 % ^{10}B) borated ionisation chamber is a new approach in BNCT dosimetry.

A very fast and easy measurement is possible with the triple chamber system. The thermal neutron component can be separated very accurately by the borated Mg chamber and the chamber is expected to be a helpful dosimeter for further characterisations of BNCT beams. However, the determined fast/epithermal neutron dose as well as the gamma dose differ sig-

nificantly from published and simulated data. The determination of the h- and particularly of the k-factors is obviously not satisfactory. Gamma and fast/epithermal neutron dose have not been determined accurately, although a total error of $\pm 20\,\%$ for the determination of D_{n} and a total error of $\pm 10\,\%$ for the determination of D_{γ} was assumed.

Possible reasons should be found by a more comprehensive characterisation of the present beam. This is currently performed by the BNCT group in Petten, including measurements with different dosimetric equipment and computer simulations. Changes in the photon and neutron spectra due to the fuel change from highly to low enriched uranium in the year 2005 have to be identified exactly. Obviously other k-values should be applied. Moreover, very accurate Monte Carlo simulations of the internal chamber geometries are required.

The cross check of the calibration data revealed reliable results for the thermal neutron calibration. However, it will be shown in the following section that this calibration is not suitable for the determination of the dose from photoneutrons in a high-energy photon field at a medical linear accelerator.

6 Neutrons in high-energy photon beams

A common way of treating deep seated tumours is the use of high-energy photons (e.g. 15 MV) as a higher penetrative quality, a lower skin dose, steeper dose gradients, and a better dose conformation are achieved in contrast to beams with lower photon energies. For photon beams at linear accelerators, the cross section for photoneutron production increases for energies above a threshold of approximately 7 MeV. Neutrons are produced in several high-Z materials of the accelerator head. The undesired radiation is not calculated and not considered for in the radiotherapy treatment planning process. For the conventional treatment techniques the contamination is relatively low and therefore acceptable by most clinicans [3]. However, radiation treatment delivery techniques like intensity modulated radiotherapy (IMRT) are being rapidly implemented. IMRT is based on the concept that the radiation beam intensity is varied inside the treatment field. One method of IMRT uses small segments by attenuating large portions of the primary photon beam. Therefore many segments are required to deliver the dose to a large treatment area. This leads to longer beam-on time to cover the same treatment area. The increased beam-on time results in increased scattered radiation and increased secondary neutron production. Moreover, with the IMRT technique steeper dose gradients can be achieved. Therefore it has been possible to increase the tumour dose by 5 – 10%, thus increasing the potential neutron dose even further. It is presumed that the additional neutron dose to the patient is a function of the beam-on time, but only a few direct measurements have been reported.

A few authors have already studied the neutron contamination, especially those of the 15 MV photon mode of a Siemens PRIMUS, either through direct measurements [28, 29] or Monte Carlo simulations [30–32]. The experimental determination of the neutron contamination is difficult, since at a linac the ratio of ϕ_γ/ϕ_n is of the order of 10^5 inside the open field. In addition leads the pulsed-beam nature to pulsed pile-up effects in the radiation detector and noise problems prevent the separation of the neutron signal. Nevertheless, measurements could already be performed with Bonner spheres, bubble detectors or foil activation techniques [33–37]. All these techniques are very time consuming, not all can be used inside the open field as their neutron sensitivity is too low or they cannot account for the patient or phantom geometry.

Therefore, the suitability of the triple ionisation chamber system (see Chapter 3.3.2) for photoneutron detection in a therapeutical used high-energy photon field should be investigated during this work. The system can be handled like other ionisation chambers and is therefore easy to use. In addition its small size allows pointwise continuous measurements, and the high thermal neutron sensitivity allows measurements inside the clinically used photon field. As the fast neutron dose component at the linac is very small and the detector signal to these fast neutrons cannot be separated correctly, the ionisation chamber system was reduced to a paired system utilising Mg/Ar and MgB/Ar chamber. This paired chamber system detects the thermal neutron component only and therefore the already determined calibration factors

cannot be applied to obtain the total neutron dose. A calibration of detector signal to Monte Carlo simulated total neutron dose is performed.

The Siemens PRIMUS machine with the treatment room at the University Medical Center Hamburg-Eppendorf was investigated in its 15 MV photon mode. It has been studied in detail by Monte Carlo methods by J. Becker [38]. Results are presented in Chapter 6.1. The Monte Carlo code MCNPX version 2.5.0 was used to model the geometry and the set up was verified by checking calculated photon depth-dose curves and beam profiles in a water phantom against measurements. The neutron distribution was calculated inside the treatment room.

With the help of these and further detailed simulations, the general suitability of the ionisation chambers to detect the produced photoneutrons was investigated with a special albedo technique and is described in Chapter 6.2. The measurements were compared to MC simulations and measurements with the TL detector system described in Chapter 3.3.4.

In the next section measurements, performed in an open field, are compared to MC calculated neutron dose. With the ionisation chamber system depth and crossplane dose distributions could be recorded in a water phantom and the field size dependency of the signal was studied. The results are shown in Chapter 6.4. In Chapter 6.5 several special clinical treatment techniques for prostate patients were studied in a solid water phantom to estimate the equivalent neutron dose for a whole treatment series of a patient.

Finally, in the last section of Chapter 6, the suitability of system to measure neutron contamination in a photon beam was verified at another linac and the obtained data was compared to the previous measured data of the Siemens PRIMUS.

6.1 Monte Carlo Simulations of the PRIMUS linac features

The Siemens PRIMUS was modeled in its 15 MV mode with MCNPX 2.5.0 in the diploma thesis of J. Becker [38] and the results were published in [16].

The Monte Carlo method simulates individual particles and records specific aspects (tallies) of their average behaviour. The individual probabilistic events that comprise a process are simulated sequentially. The probability distributions governing these events are statistically sampled to describe the total phenomenon. The statistical sampling process is based on the selection of random numbers.

MCNPX is a Monte Carlo radiation transport code that tracks almost all particles at nearly all energies. In MCNPX the space is divided into user specified cells, which are created by boolean combinations of surfaces. MCNPX knows several primitive surfaces (e.g. plane, sphere, cone etc.) and macrobodies (e.g. box, cylinder, etc.), which can be combined with boolean operators (union, intersection, etc.) to form complex cells. All cells together form the geometry of a calculation. The code uses an input file in which the problem is separated in three parts: The first section specifies the geometrical cells used in the calculation. The second section defines all surfaces and marcobodies used for cell definition and the third section specifies all other data necessary (e.g. the source specifications, the kind of output, variance

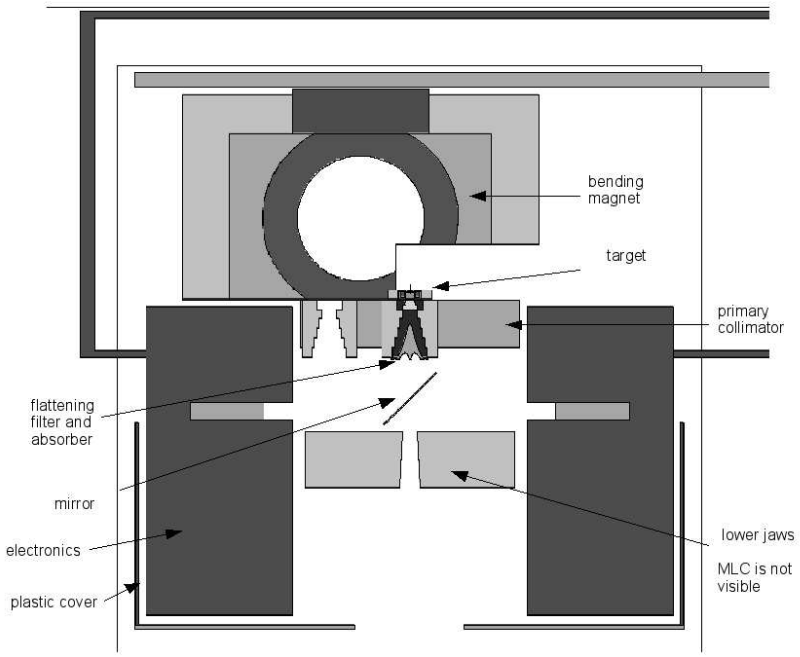

Figure 6.1: MCNPX plot of the linac head geometry.

reduction methods).

For the simulations the most recent available cross section were used wherever possible (ENDF/ B.VI-8 for photon, ENDF/B.VI for most neutron cross sections). The photonuclear data is a subset of the IAEA Coordinated Research Project (CRP) on photonuclear data. Cross sections not provided by this library were taken from the Nuclear Physics Group (T-16) at Los Alamos National Laboratory. Thermal scattering cross sections for water and graphite from ENDF/B.VI-3 were used where appropriate.

The geometry data of the studied Siemens PRIMUS was provided by Alfredo Siochi [39]. However, the gold target specified there has been replaced by the actual tungsten target of the present Siemens PRIMUS. In contrast to pure photon simulations of the linac, additional components have a significant influence on the simulation outcome and are also included in the simulations. The following elements of the treatment head were included: tungsten target, electron absorber, primary collimator, flattening filter, jaws, MLC, mirror, bending magnet, target slide, 6 MV primary collimator, supportive steel structure (block) housing both collimators, supportive steel plate, steel skeleton of the gantry, electronics, outer steel and lead shielding, outer plastic cover, surrounding air and room walls. The electronics filling the treatment head were approximated as a cylindrical shell of low density ($0.5\,\mathrm{g\,cm^{-3}}$ consisting of 6.4 wt-% hydrogen, 38.4 wt-% carbon, 51.4 wt-% oxygen, 1.8 wt-% iron and 2 wt-% copper). The patient couch out of carbon fiber was also included. A plot of the simulated linac head geometry is shown in Figure 6.1. Parts of the geometry not modeled were the dose chambers, a bending magnet exit window and a 15 MV compensator, as their impact on the neutron production is negligible.

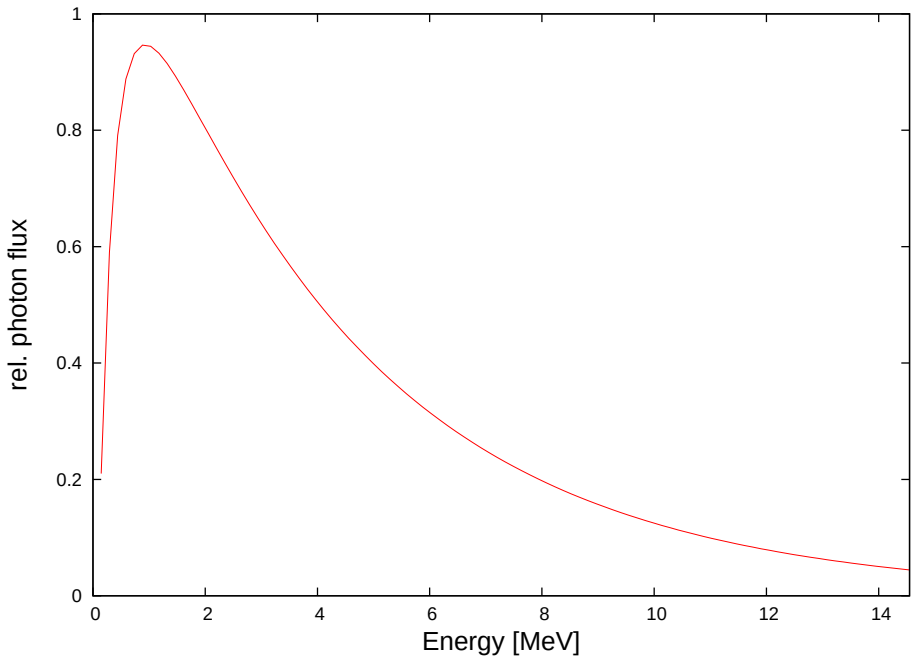

Figure 6.2: Photon spectrum obtained by the MCNPX simulations of the Siemens PRIMUS.

Siemens accelerators of the same nominal energy may differ significantly in the energy of the primary electrons. With the use of the same nominal energy as Pena *et al.* [40] reported, the measured photon depth dose curve for the present Siemens PRIMUS could not be reproduced. To match simulations and measurements of photon percentage depth-dose (PDD) and beam profiles the nominal electron energy was increased to 14.55 MeV and the Gaussian distribution had to be modified in such a way that sampling probability decreased linearly rather than Gaussian for energies below 14.0 MeV and above 15.1 MeV. The spatial distribution was Gaussian with a FWHM of 0.15 cm. A fit of the photon spectrum applied here is presented in Figure 6.2, for more details about the spectrum see [16].

The following MCNPX variance reduction options were used: cell importance, biased bremsstrahlung production, biased photonuclear production, global electron energy cutoff of 200 keV and particle weight cutoff (-0.1 for electrons, -0.2 for photons, -10^{-9} for neutrons). The cell importance was chosen in such a way that photons and electrons which reach the shielding concrete or exceeds a lateral distance of 1 m from the beam axis are terminated. The bremsstrahlung production was biased in graphite and tungsten.

The mean photon energy at a source-surface-distance (SSD) of 100 cm in air is 4.149 MeV. From the fit of calculated PDD and the measured data a 'primary particle-to-100 MU' calibration factor could be derived. This factor was determined to $F_{100\,MU} = (1.522 \pm 0.038) \times 10^{15}$. Values are normalised in such a way that a defined amount of MU leads to 1 Gy dose in the dose maximum of a $10 \times 10\,cm^2$ field in water with a SSD of 100 cm. For the Siemens PRIMUS used here 98.1 MU correspond to 1 Gy, so that the corresponding conversion factor is $F_{1\,Gy} = 0.981 \cdot F_{100\,MU} = (1.494 \pm 0.037) \times 10^{15}$.

Neutrons are produced at multiple locations inside the Siemens PRIMUS machine. Thus, for neutron source characterisations it is essential to know the locations of the neutron production. Table 6.1 shows the contribution to the total photoneutron production of the individual treatment head components.

Location	%	Location	%
Primary collimator	54.85	Steel and lead shield	0.11
MLC and jaws	26.72	X-low collimator	0.07
Target	10.08	Steel skeleton	0.03
Target slide	5.64	Absorber	0.01
Flattening filter	1.74	Steel plate	0.003
Bending magnet	0.61	Electronics	0.001
Steel block	0.13	Other	0.006

Table 6.1: Contribution of individual accelerator components to the overall neutron production determined by MC simulation (10 million produced photoneutrons, requiring 30 million primary particles).

Excluding the target (made of tungsten, copper, steel, water and graphite), components made of tungsten account for roughly 87 %, steel components for roughly 2 % to the total neutron production. The statistical error of the simulations was usually below 1 % except for bins with very few particles where it was below 10 %. The statistical error does not include any error in cross section evaluations or of approximations in physics models of the Monte Carlo code. It is assumed that these systematic errors are in the order of 5 %.

Distinguishing between source spectrum and spectrum at a given location is important. Counting each neutron only once, the source spectrum tallies neutron weight and energy at time of its production. Counting every neutron which transverses the tally volume (voxel of $(10\,\mathrm{cm})^3$) at the isocenter (100 cm distance to the source) delivers the spectrum at this location. The later includes also the neutrons that are backscattered from the treatment room. The source does not produce neutrons with energies below 10 eV. All thermal neutrons tallied at the isocenter originate from scattering reactions throughout the treatment room. Figure 6.3 shows the fit[5] of the calculated source spectrum compared with the calculated spectrum at the isocenter in 3 cm depth RW3. The mean neutron energy was calculated for source neutrons ($\overline{E} = 1.06\,\mathrm{MeV}$) and at the isocenter ($\overline{E} = 0.458\,\mathrm{MeV}$). The most probable energy of source neutrons was $\widehat{E} = 450\,\mathrm{keV}$ and the maximum neutron energy found was $E_{\max} = 8.7\,\mathrm{MeV}$ (see Figure 6.3).

The neutron source strength Q is an important quantity for radiation protection. The neutron

[5]For fit details see [16].

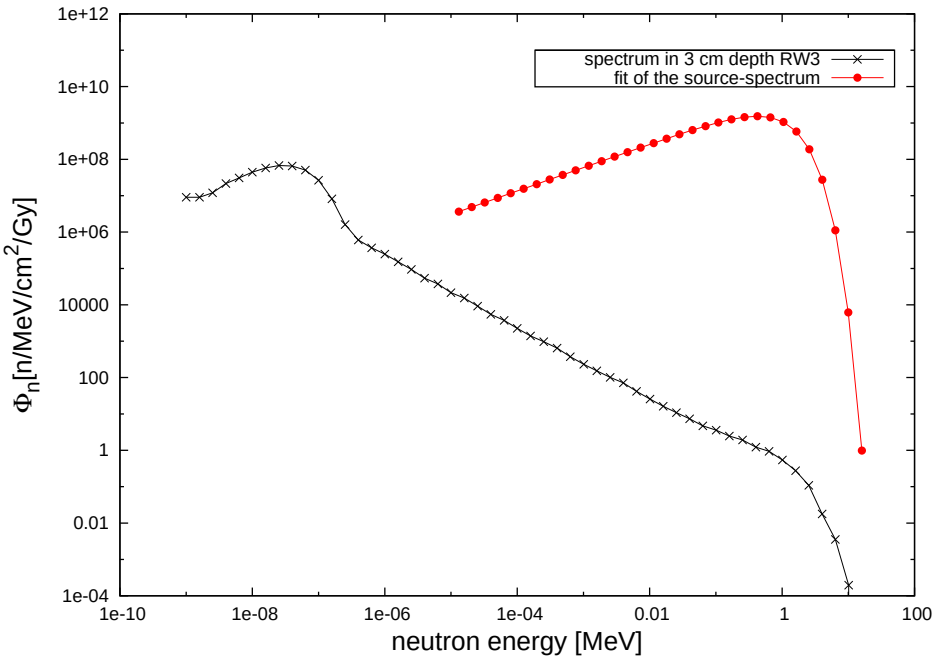

Figure 6.3: MCNPX calculated neutron source spectrum and the neutron spectrum at the isocenter in 3 cm RW3.

flux at a given location from the source can be calculated in the following way [41]:

$$\phi(r) = \frac{aQ}{4\pi r^2} + \frac{5.4aQ}{S} \tag{6.1}$$

where r is the distance to the neutron source, a is the neutron transmission factor for the head shielding and S is the surface area of the treatment room. The first term of the sum considers the neutrons that are transmitted through the treatment head (source), the second term accounts for the room scattered neutron component (albedo component). Radiation protection guidelines for room shielding provided by Siemens assume a source strength of $Q = 0.8 \times 10^{12}\,\mathrm{N\,Gy^{-1}}$, where the normalisation $\mathrm{N\,Gy^{-1}}$ means neutrons per Gray at the depth-dose maximum of a $10{\times}10\,\mathrm{cm^2}$ field in a water phantom with SSD 100 cm (reference conditions). The neutron source strength calculated here is $Q = 0.136 \times 10^{12}\,\mathrm{N\,Gy^{-1}}$. Pena *et al.* [30] calculated a value of $Q = 0.17 \times 10^{12}\,\mathrm{N\,Gy^{-1}}$ from their MCNPX simulations. Both are comparable to the results of the measurements by Followill *et al.* [28] ($Q = 0.12 \times 10^{12}\,\mathrm{N\,Gy^{-1}}$ and $Q = 0.21 \times 10^{12}\,\mathrm{N\,Gy^{-1}}$) and by Lin *et al.* [29] ($Q = 0.20 \times 10^{12}\,\mathrm{N\,Gy^{-1}}$) within the uncertainties and the consideration of different target materials (gold or tungsten, respectively) and treatment room geometries (see dependence on volume V below).

The flux distribution for thermal neutrons ($E_\mathrm{n} < 1\,\mathrm{eV}$), epithermal neutrons ($1\,\mathrm{eV} < E_n < 0.1\,\mathrm{MeV}$) and fast neutrons ($0.1\,\mathrm{MeV} < E_\mathrm{n}$) inside the treatment room was also simulated for a $10{\times}10\,\mathrm{cm^2}$ field. It was observed that the fast neutron distribution followed a $1/r^2$ law with modifications due to the room geometry. The patient table reflects neutrons along the central axis, creating an increased flux above and an decreased flux below the

table. Additionally, neutrons are reflected from the room walls. Absolute peak intensities were 3.17×10^7 n/cm^2/Gy for thermal, 1.67×10^8 n/cm^2/Gy for epithermal and 5.54×10^8 n/cm^2/Gy for fast neutrons. The normalisation is to Gray under reference conditions (dose of 1 Gray in the dose maximum of a 10×10 cm^2 field in water with SSD 100 cm).

The influence of the properties of the surrounding area (volume V and surface S) is demonstrated by the fact, that MCNPX calculated a higher neutron flux for an identical Siemens PRIMUS in a smaller treatment room. This is due to the fact that thermal and epithermal neutron flux have a $1/V$ dependence, as was already shown in literature [30].

6.2 Suitability of the detector systems for photoneutron detection

For a single open field in the 15 MV mode of the Siemens PRIMUS the ratio of $\phi_\gamma/\phi_\mathrm{n}$ is of the order of 10^5. For a first investigation of the general suitability of the paired ionisation chamber system (see Chapter 3.3.2) and the TL detector system (see Chapter 3.3.4) to detect photoneutrons in a photon beam and to obtain a neutron detection limit for both detector systems, a special kind of albedo technique[6] is applied. In fact, as the detector systems are particularly sensitive to the thermal neutron component, the fast photoneutrons produced in the accelerator head have to be moderated to thermal energies before they can be detected.

Therefore the detector systems were exposed (isocentric set up, 10×10 cm^2 field) in 3 cm depth in a RW3 plate phantom (each plate 30×30 cm^2 stacked to a height of 24 cm) with several tungsten plates (each $10 \times 10 \times 1$ cm^3) on top of the phantom. Tungsten is chosen since its combined scattering and absorption cross sections are higher for photons than for neutrons. The neutron energy spectra in a reference depth of 3 cm with and without tungsten on top do not show significant differences (see Figure 6.4). However, the photon component is significantly influenced and the ratio of thermal neutrons to photons is increased. In the isocenter in 3 cm depth, the neutron spectrum is already governed by the thermal neutrons that are backscattered from the treatment room. The tungsten plates and the RW3 in front of the point of measurement serve as a moderator and therefore the fast neutrons thermalise. In addition, an albedo neutron component can be measured due to the RW3 behind the point of measurement. The same set up was simulated with MCNPX 2.5.0.

Measurements with 3, 4, 5 and 6 cm thick tungsten plates on top of the phantom and both types of detector systems were performed. Three TLDs of each type were used for the measurement to have the same physical dimensions as the active volume of the ionisation chambers. Taking into account the individual TLD response and the different response of both TLD types to a pure photon beam, the MCP-600D delivers an additional excess signal that is due to the neutrons. The excess signal of MCP-600D was compared to a measured excess signal of a paired ionisation chamber system consisting of Mg/Ar and MgB/Ar chambers. For the determination of the excess signal of the paired ionisation chambers, a k_rel-factor is necessary

[6] Albedo techniques are used to overcome the difficulty to detect fast neutrons, since most of the solid state detectors are only sensitive to thermal neutrons. Neutrons incident on a body are scattered and moderated by the nuclei of the atoms of the body. The low energy neutrons, called albedo neutrons, leave the body in front of the body. They can be measured and the dose from the original neutrons can be estimated.

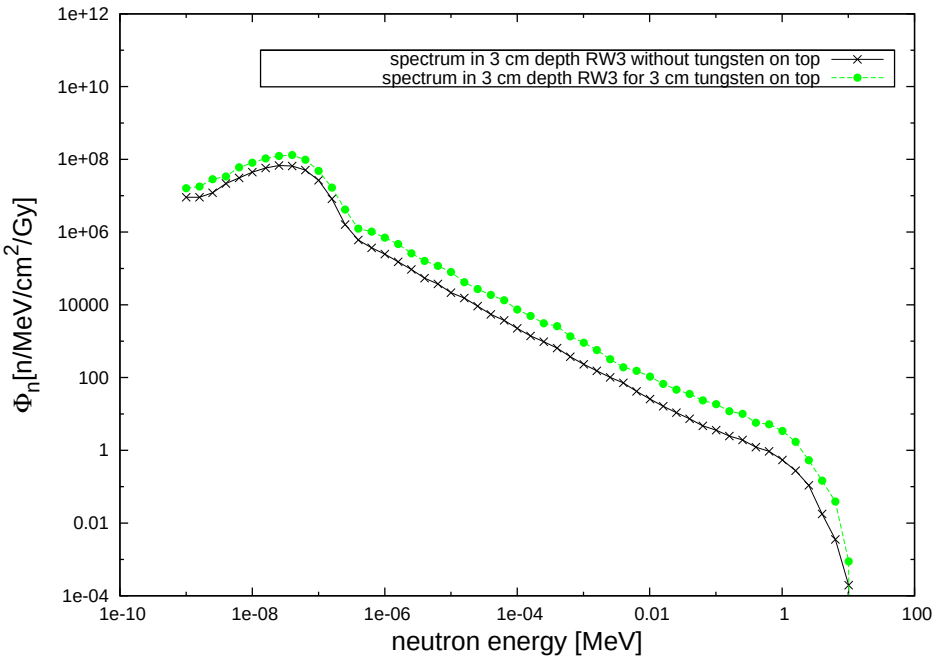

Figure 6.4: MCNPX calculated neutron spectrum in 3 cm depth RW3 with and without tungsten on top of the phantom. No significant differences in the thermal neutron range of the spectra can be found.

to account for the different photon sensitivity of both chambers:

$$\Delta Q = M_{\mathrm{MgB}} - k_{\mathrm{rel}} \cdot M_{\mathrm{Mg}} \tag{6.2}$$

k_{rel} was determined in photon fields not contaminated by neutrons, where $\Delta Q = 0$ per definition. The results are shown in Table 6.2.

photon energy, accelerator	k_{rel}
4 MV, MDX-2	1.006
6 MV, MDX-2	1.011
6 MV, PRIMUS	1.007
mean	1.01 ± 0.03

Table 6.2: k_{rel}-values determined by exposure of MgB/Ar and Mg/Ar chamber to 100 MU at two Siemens linacs in 3 cm depth in RW. The uncertainty includes the statistical uncertainty and systematic errors (e.g. the dependence of k_{rel} on the measurement depth).

The measured photon dose D_γ and the excess charge for both detector systems at the ref-

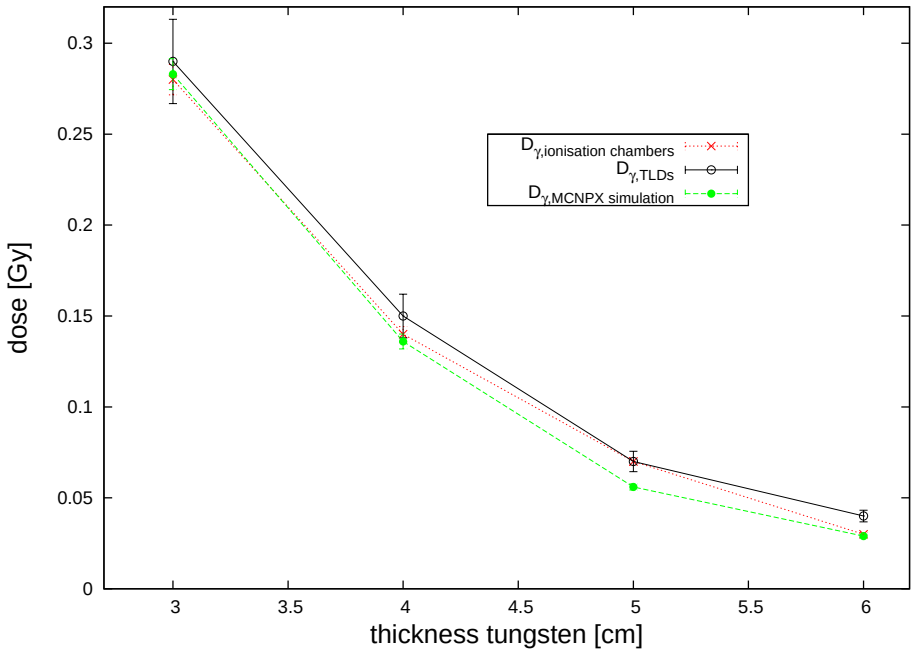

Figure 6.5: The photon dose D_γ measured with the Mg/Ar chamber and with the TL detectors of type MCP-700D in comparison to MCNPX calculated data.

erence point in 3 cm depth were compared to the MCNPX simulation of the set up. The calculated parameters were photon dose and reaction rate in ^{10}B and ^{6}Li, respectively. Figure 6.5 shows the measured and calculated photon dose for different thicknesses of tungsten for an irradiation with 100 MU. Measured data were determined from the detector response of the MCP-700D and the Mg/Ar chamber.

For 3 and 4 cm thick tungsten the measured and calculated photon dose agree well within error margins, whereas for 5 and 6 cm thick tungsten the difference is larger. However, a similar decrease with increasing tungsten thickness can be observed.

The number of detected neutrons decreases if more tungsten is placed on top of the phantom, because neutrons are scattered out of the central axis by the additional material. So the excess signal of both detector systems decreases with increasing material thickness. At the measurement point, a ratio of $\phi_\gamma/\phi_\mathrm{n}$ of the order of 10^3 to 10^4 was estimated. Figure 6.6 shows the relative excess signal measured with the TLD system and the ionisation chamber system in comparison to the relative signal of the reaction rate in ^{10}B and ^{6}Li calculated with MCNPX. The reaction rate was tallied in 3 cm depth of the RW3 phantom (flat cylinder with $z = 0.4$ cm, $r = 2.5$ cm, center at 3 cm depth) without detector presence.

The agreement between the reaction rate in ^{10}B and the experimental data obtained with the ionisation chamber system is within the uncertainty (except 6 cm tungsten). The measurements with the TL detector system do not reproduce the reaction rate in ^{6}Li. Other components in the TL detector have obviously a non-negligible energy-dependent influence on the detector signal.

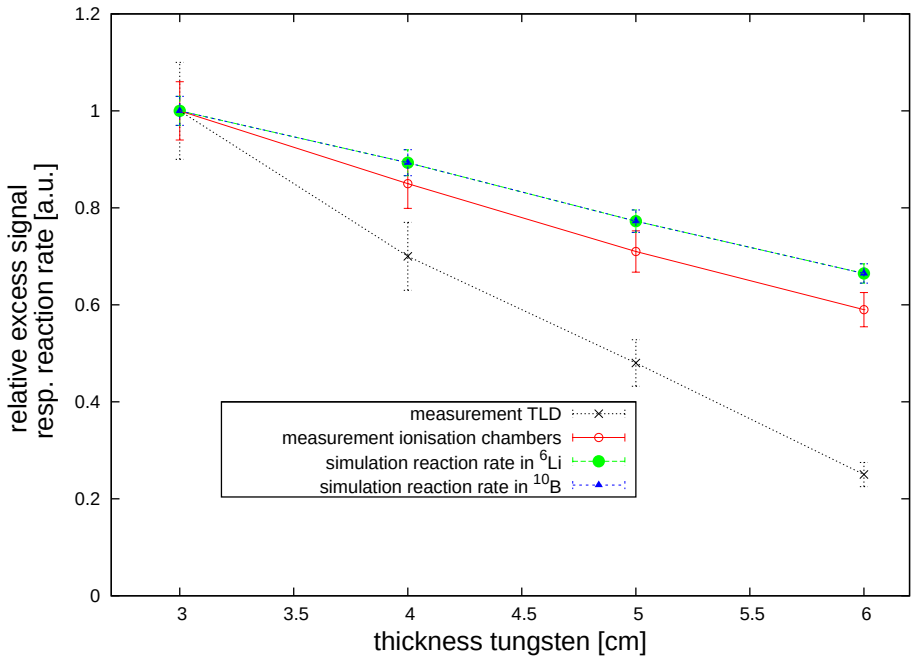

Figure 6.6: The relative excess signal as a function of tungsten thickness measured with the TLD system and the ionisation chamber system in comparison to the relative signal of the reaction rate in ^{10}B and ^{6}Li calculated with MCNPX. Normalisation of all data is performed to 3 cm tungsten thickness. Relative reaction rate in ^{10}B and ^{6}Li are identical.

The absolute measurement data (for 3 cm tungsten on top of the phantom) for the ionisation chamber system revealed a relative photoneutron sensitivity that is four times higher than that of the TLD system (see Table 6.3). The mean energy of the detected thermal photoneutrons was estimated from the Monte Carlo simulated neutron spectrum and is approximately 50 meV. The cross sections of ^{10}B and ^{6}Li for an energy of 50 meV are approximately 2710 b and 665 b, respectively and confirmed the sensitivity difference.

detector	ΔQ_γ [nC]	ΔQ_n [nC]	$\Delta Q_\mathrm{n}/\Delta Q_\gamma$ [ ]
MCP-600D	0.3	0.03	0.1
MgB/Ar	7.4	2.9	0.4

Table 6.3: The relative photoneutron sensitivity $\Delta Q_\mathrm{n}/\Delta Q_\gamma$ for MCP-600D and MgB/Ar chamber differ by a factor of four.

For both detector systems the photoneutron detection limit in the presence of high-energy photons can be estimated: The photon detection limit for the MgB/Ar chamber in the used set up is 0.3 mGy and is due to the display accuracy of the electrometer. Using the thermal neutron sensitivity obtained in Chapter 4 ($i_\mathrm{MgB} = 24150$), the thermal neutron detection limit for the paired ionisation chamber is 0.01 μGy per 1 Gy photon dose. The TL detector system

has a four times lower sensitivity to neutrons than the ionisation chamber system. Moreover, the poor reproducibility of each TLD leads to a detection limit of only 10 μGy neutron dose per 1 Gy photon dose.

6.3 Measurements under reference conditions in solid water RW3

The general suitability of the paired ionisation chamber system and the TL detector system for photoneutron detection was shown in the preceding section. However, for a conversion of the detector system signal to neutron dose, a calibration under reference conditions is necessary. For the TLD system, the investigations using the albedo technique showed a very low neutron sensitivity in contrast to the ionisation chambers. Therefore attention was focused on the ionisation chambers for further measurements. The obtained calibration from LFR and HFR was validated in the next step by a comparison with MC simulations.

Measurements were performed in the IMRT quality assurance (QA) phantom 'Easy Cube' with a 10×10 cm^2 field and a SSD of 100 cm. Each ionisation chamber was exposed to 15 MV photons with 100 MU and the excess signal of the MgB/Ar chamber was determined. The MgB/Ar chamber is suitable to detect the thermal neutron dose, as the boron coating has a high cross section in this energy range. Thus, the signal was converted to thermal neutron dose using the calibration factor obtained at different neutron sources from Chapter 4.1.2. For a comparison, the total neutron dose was calculated with MCNPX. The obtained values for measurements and simulation in 5 cm depth are listed in Table 6.4.

ΔQ, ionisation chamber	MCNPX calculated D_{n}	calculated $D_{\mathrm{n,th}}$ using chamber calibration
0.66 nC ± 0.04	35.9 μGy ± 1.1	1.7 μGy± 0.1

Table 6.4: Excess signal ΔQ for MgB/Ar ionisation chamber under reference conditions (10×10 cm^2 field, SSD 100 cm) in 5 cm depth RW3 in comparison to simulated and calculated neutron dose. The detectors were exposed to 15 MV photons with 100 MU. The uncertainty for ΔQ results from the statistical uncertainty of the measurements with Mg/Ar and MgB/Ar chamber. The uncertainty for the MCNPX simulations includes the statistical error of the simulations. The uncertainty for $D_{\mathrm{n,th}}$ includes the uncertainties for the determination of ΔQ and the uncertainty resulting from the applied calibration.

The comparison shows that the total neutron dose is significantly higher as the dose calculated from the excess charge of the MgB/Ar chamber. Obviously there is a contribution from faster neutrons which are not detected by the ionisation chamber system. The use of the calibration data from Chapter 4.1.2 does not lead to the total neutron dose.

Therefore a new conversion of measured excess signal to MCNPX calculated total neutron depth dose (see Figure 6.7) is necessary and will be performed next.

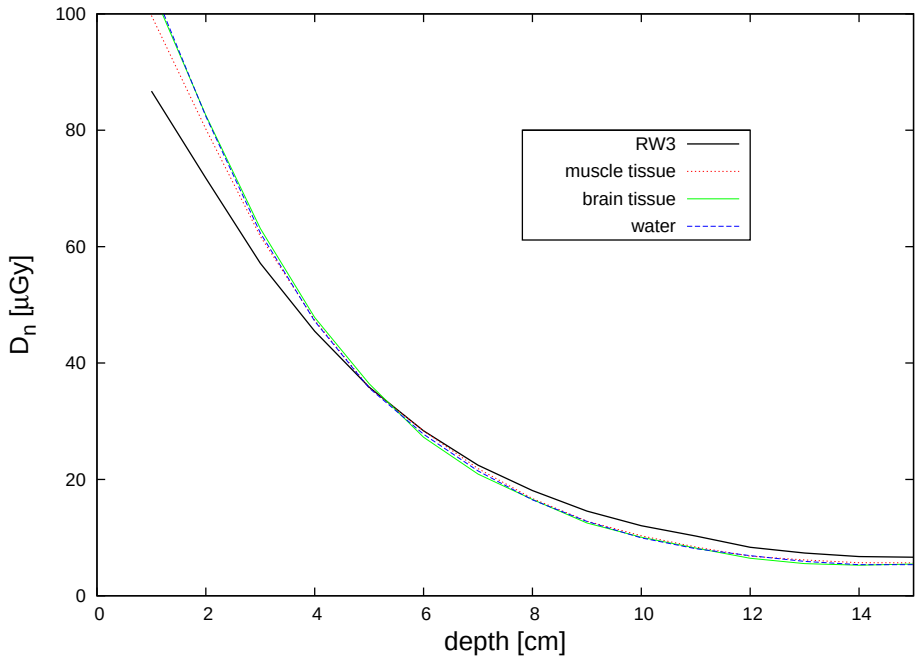

Figure 6.7: The total neutron depth dose per 100 MU ($10\times10\,\mathrm{cm}^2$ field) in different materials calculated with MCNPX.

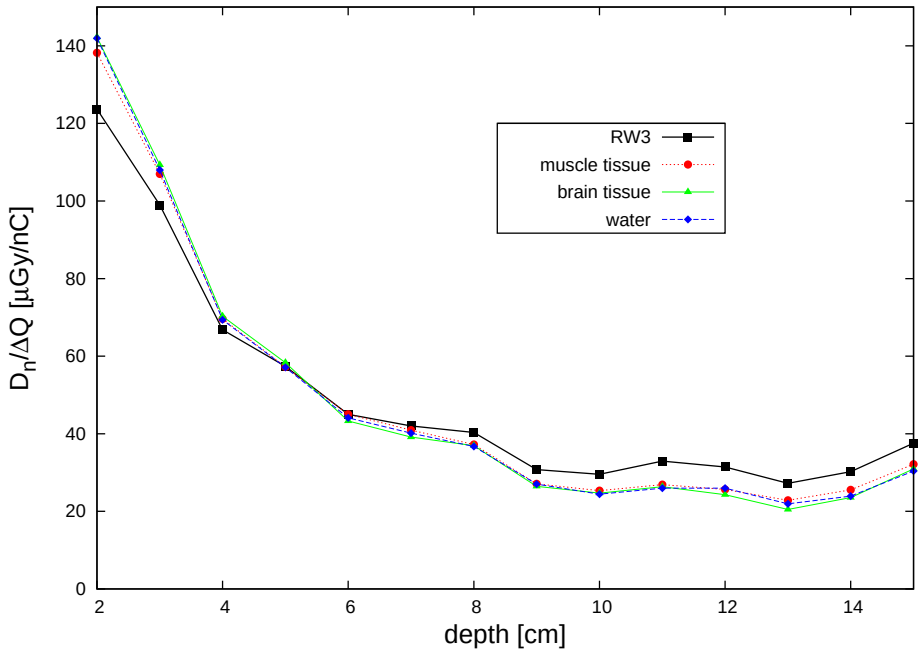

Figure 6.8: Conversion factor to convert excess signal measured in RW3 with the paired ionisation chamber system into total neutron dose in different materials as a function of depth.

As already described in Chapter 3.4 the reference material in neutron dosimetry, in contrast to photon and electron dosimetry, is not water. For neutrons, dose is normally given as dose in muscle tissue, in BNCT as dose in brain tissue. Additionally, RW3 is not water equivalent for neutrons. To convert the excess charge ΔQ measured in RW3 into neutron dose of muscle tissue, brain tissue or water, respectively, the material specific neutron dose D_{n} (see Figure 6.8) was calculated with MCNPX simulations. To obtain the calibration the following procedure was performed: Measurements with the paired chamber system utilising Mg/Ar and MgB/Ar chambers were performed in the Easy Cube in 1 cm steps along the central axis (CAX) of the beam and the excess signal was calculated. MC simulations were done with MCNPX 2.5.0 and the assumed set up was the same as for the measurements. For simulating different materials, again the same input was used with a replacement of the RW3 with muscle tissue, brain tissue or water, respectively.

It can be observed that both, neutron dose as well as excess signal, decrease rapidly with increasing depth. The fast neutrons that yield the major part of the dose, but are not detected by the borated Mg chamber, thermalise and can then be detected. At a depth of 8 cm a nearly constant ratio of $D_{\mathrm{n}}/\Delta Q = 30\,\mu$Gy/nC is reached. The conversion allows to measure in a RW3 phantom and to estimate the neutron dose for different tissues or water for any desired set up.

6.4 Depth and crossplane distributions, field size dependency in a water phantom

The photoneutron contamination of the 15 MV photon field at the Siemens PRIMUS was studied in more detail inside a water phantom. Depth dose distributions and field profiles were studied for different field sizes with the paired chamber system consisting of Mg/Ar and MgB/Ar chamber. The phantom has dimensions of 64.5 cm × 67.5 cm × 56 cm and can be filled with water to a height of 49.5 cm. The PMMA walls of the phantom are 1.5 cm thick. The water phantom was irradiated from the top (gantry angle of 0°) and a SSD of 100 cm. The excess signal was determined taking into account the different sensitivity of each chamber to a pure photon beam by using the k_{rel} factor.

Measurements were performed for field sizes[7] of $0\times0\,\mathrm{cm}^2$, $5\times5\,\mathrm{cm}^2$, $10\times10\,\mathrm{cm}^2$ and $20\times20\,\mathrm{cm}^2$. Figure 6.9 and 6.10 show the obtained depth distribution and the beam profiles in 5 cm depth considering the excess signal of the borated Mg chamber for the four field sizes. For the $0\times0\,\mathrm{cm}^2$ field no signal could be obtained with the Mg/Ar chamber and the excess signal is the raw signal of the MgB/Ar chamber.

The depth distributions of the excess signal show no dependence on the field size for larger depths. For the field sizes $5\times5\,\mathrm{cm}^2$, $10\times10\,\mathrm{cm}^2$ and $20\times20\,\mathrm{cm}^2$ a shift of the beam profiles can be observed at the field edges which is due to the energy dependence of the k_{rel} value, since the mean photon energy differs significantly inside and outside the photon field. This energy dependence also explains the negative excess charge values at small depths. Near the

[7] For a $0\times0\,\mathrm{cm}^2$ the jaws and the MLC of the linear accelerator are completely closed, but with simultaneous photon exposure. Thus, only a transmission component and produced photoneutrons reach the point of measurement.

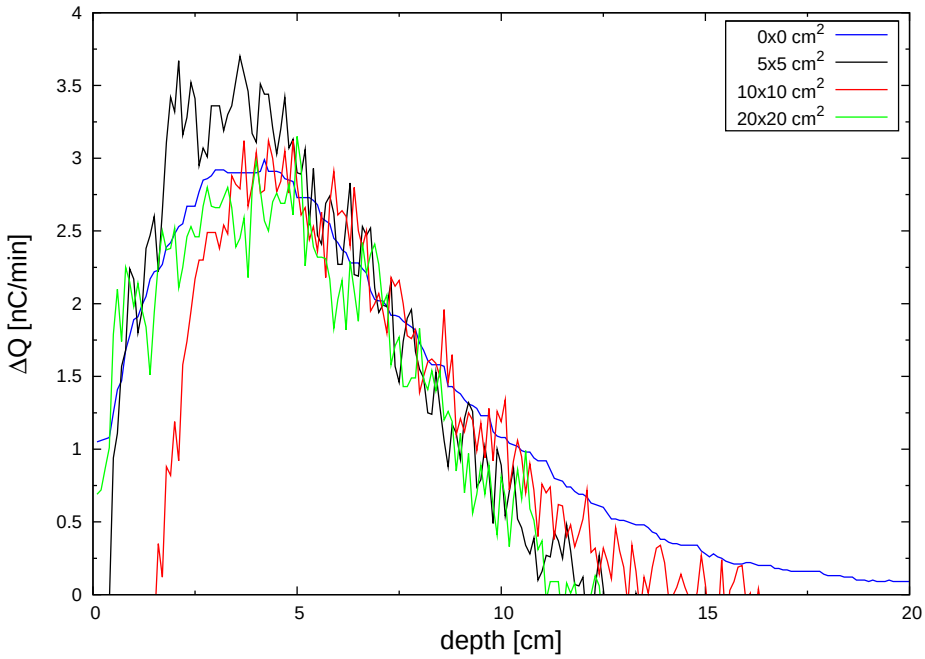

Figure 6.9: The relative excess signal measured in the water phantom along the CAX with the ionisation chamber system for different field sizes.

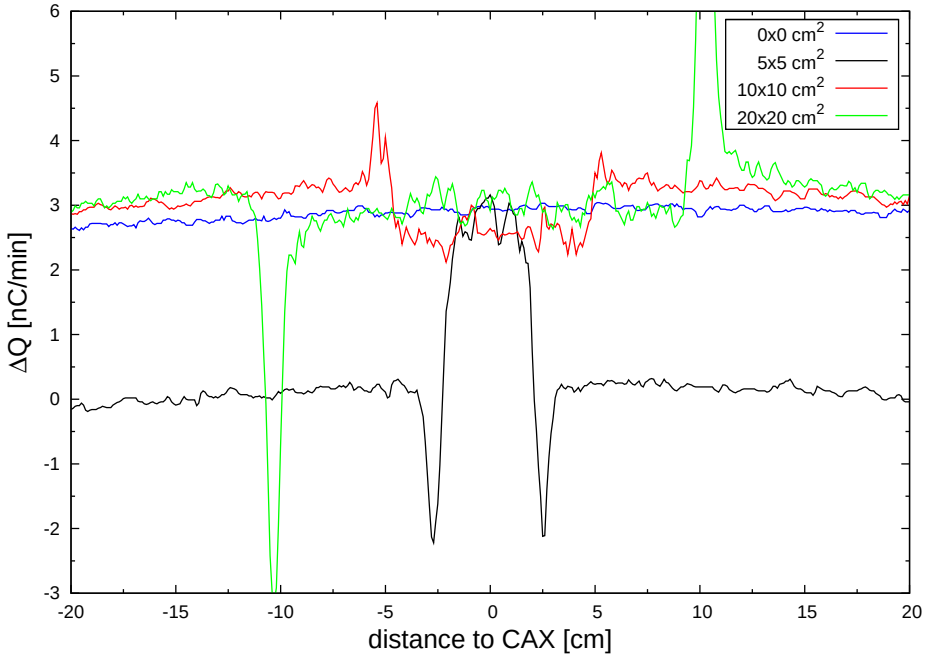

Figure 6.10: The relative excess signal measured in the water phantom along a profile in 5 cm depth with the ionisation chamber system for different field sizes.

water surface secondary electrons and low-energy photons contaminate the beam resulting in a different mean photon energy. The profiles show no dependence on the field size and no field edges. The measurement data for the $0\times0\,\mathrm{cm}^2$ field show that the thermal neutron dose distribution which is detected by the chamber system has a gaseous behaviour and is therefore independent of the field size and the distance from the CAX (inside or outside the field) in the phantom.

6.5 Investigation of several clinical treatment situations

To treat a radiotherapy patient, it is usually necessary to use multiple fields in order to form an accurate dose distribution that covers the whole planning target volume (PTV) that should be treated. The sparing of normal tissue and organs at risk (OAR) leads to a very complex treatment planning process. For the treatment planning process, the neutron contamination of the high-energy photon field is neglected and not calculated. Instead it is predicted that scattering radiation and neutron contamination are a function of the applied monitor units.

The use of high-precision techniques like intensity modulated radiotherapy (IMRT) increases the number of monitor units (MU) and the beam-on time by a factor of 3 – 9. To estimate whether the neutron dose increases with the number of MU per delivered photon dose, different realistic plans for the treatment of prostate cancer have been studied in a phantom. Two standard irradiation techniques and one IMRT plan were adapted to the Easy Cube extended to an abdominal-shaped phantom in this work. Simultaneously measurements with the paired ionisation chamber system were performed [42].

The first treatment plan ('box') is a four-field conventional 3D conformal plan. Conventional 3D conformal treatment delivers radiation in individually shaped fields from multiple gantry angles. The individual field shaping is usually done with the MLC of the accelerator. The gantry angles for the 'box' are 0°, 90°, 180° and 270° (see Figure 6.11, top). The second plan ('cross') is a treatment technique for the prostate that is applied if the patient has metal hip protheses. Irradiation through the metal and the femoral head is usually avoided [43], therefore the field arrangement has the shape of a cross (see Figure 6.11, middle). The IMRT treatment plan ('imrt') is different from the conventional plan. A large number of small segments are delivered instead of one whole field. To cover the same area, a larger beam-on time is therefore necessary. By this kind of intensity modelling steeper dose gradients can be achieved. The treatment plan here uses five different gantry angles with 32 MLC field segments (see Figure 6.11, bottom).

The treatment plans were calculated using the treatment planning system CMS XiO. The system calculates the expected photon dose distribution of each field arrangement on the basis of CT images of the phantom. For all three cases, the same dose in the PTV was delivered accompanied by different dose values to the OAR. Moreover, a different number of MU is necessary to achieve the planned PTV dose in the three different field arrangements. All values are listed in table 6.5 as a sum over all 40 fractions.

Measurements were performed with Mg/Ar and MgB/Ar ionisation chamber in two points

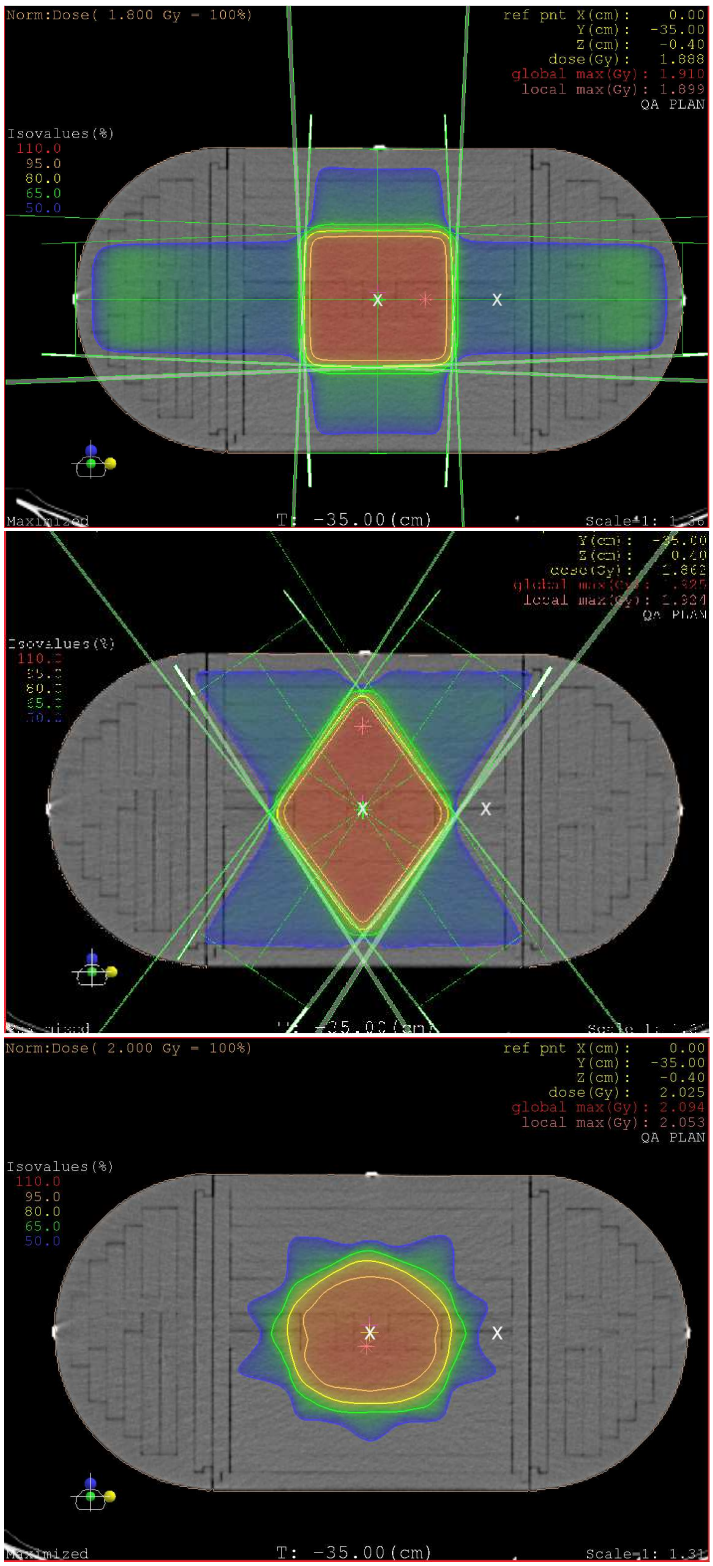

Figure 6.11: Images from the treatment planning system CMS XiO showing the field arrangement and the planned dose distribution for the 'box' (top), 'cross' (middle) and the 'imrt' (bottom) treatment plan. The white crosses mark the two measurement points in the PTV (centre) and the OAR (right). The colouring of the dose distribution is given for the isovalues (in % of the prescribed dose): 110.0, 95.0, 80.0, 65.0, 50.0

plan	frac.	MU	$D_{\mathrm{p,PTV,p}}$ [Gy]	$D_{\mathrm{p,PTV,m}}$ [Gy]	$D_{\mathrm{p,OAR,p}}$ [Gy]	$D_{\mathrm{p,OAR,m}}$ [Gy]	$D_{\mathrm{n,PTV,m}}$ [mGy]	$D_{\mathrm{n,OAR,m}}$ [mGy]
'box'	40	8774	72.0	69.0	38.2	36.7	1.1	1.1
'cross'	40	8118	72.0	68.7	3.9	3.9	1.2	1.0
'imrt'	40	11449	72.0	69.0	29.8	30.0	1.2	1.2

Table 6.5: Calculated and measured dose values for the three plans. All doses are given as a sum over all 40 fractions. The last subscript p indicates dose taken from planning system, the subscript m indicates measured dose. The neutron dose (D_{n}) is given as dose to muscle tissue and was obtained from the excess signal of the MgB/Ar chamber using a conversion factor of 30 μGy/nC. Statistical uncertainties for measured photon dose values are within 3 %, the uncertainties for the neutron dose are estimated to be within 15 %.

inside the phantom for all three plans, one in the PTV and one in the fictitious point of the femoral head as an OAR. The measured photon dose obtained from the signal of the Mg/Ar chamber as well as the planned dose values are listed in Table 6.5. The excess signal of the borated chamber was calculated according to equation 6.2 and a conversion factor for excess charge measured in RW3 to neutron dose (in muscle tissue) of $D_{\mathrm{n}}/\Delta Q = 30\,\mu$Gy/nC (depth of 9 cm RW3) is applied to estimate the extra dose due to the photoneutrons produced during irradiation. Results are also listed in the Table 6.5.

The delivered photon dose to the OAR in the 'cross' technique is very low. However, no difference in the neutron dose to the other techniques can be observed. The measurement data for all three techniques show compatible neutron doses for the PTV and the OAR. This is equivalent to the fact that the neutron dose at a depth of 8 cm is due to thermal neutrons and these neutrons have a gaseous behaviour. No influence on the field size exist and therefore the dose values inside and outside the PTV in the same depth are identical. A slight influence on the applied MU per photon dose can be observed. This is more obvious for the neutron dose in the OAR. Here the measurement uncertainty is less (±10 %) than inside the PTV (±15 %) as the ratio of $\phi_\gamma/\phi_{\mathrm{n}}$ is smaller and the excess signal can be separated more accurately. However, more plans have to be studied for a statistical significance as each plan is very individual. The result is congruent with the predictions of Howell *et al.* [3].

If calculating equivalent doses, the neutron doses are multiplied by quality factors (see Chapter 2.4). Even large factors of 20 Sv/Gy result in equivalent doses of less than 30 mSv, although this dose has to be considered as a total body dose due to the homogeneous neutron distribution. Equivalent neutron doses measured by other authors at other linacs for different prostate treatment plans range from 6 mSv at 1 m distance [44] at a Clinac 23EX to 161/129 mSv isocentric/40 cm distance to the isocenter at a Siemens PRIMUS [45]. Organ-specific neutron doses at a PRIMUS were calculated by other authors to range from 1.4 to 4.7 μSv/MU depending on the organ ($\approx$ 32 mSv in the prostate case) [46] to doses of 80 – 261 mSv depending on the organ [47].

The decision whether this dose is acceptable for the patient has to be taken by the radiotherapist responsible for the treatment.

6.6 Comparison of two accelerator types: Siemens PRIMUS vs Siemens ONCOR

The suitability of the paired ionisation chamber system for use at any desired linac to determine the photoneutron dose shall be investigated next. For this purpose, the chamber system was applied to another type of linac, the Siemens ONCOR. The Siemens ONCOR has the same geometry (except a MLC with more leaves than the one of the Siemens PRIMUS) and its photon dose output is matched[8] to that of the Siemens PRIMUS. Therefore depth dose distributions and beam profiles are identical also for the 15 MV photon mode. This mode was studied and the data was compared to that obtained for the PRIMUS.

It is assumed that the neutron energy spectrum is the same for Siemens PRIMUS and Siemens ONCOR, even though their treatment room geometries differ. This may be a potential source of error (see Chapter 6.1, dependence on volume V and surface S). The calibration of measured excess charge to neutron dose that was obtained for the Siemens PRIMUS, is nevertheless applied.

As a first step, the Easy Cube was exposed to a $10\times10\,\mathrm{cm}^2$ field. The SSD was 100 cm and measurements were performed with the paired ionisation chamber system in the middle of the phantom (9 cm depth). The excess signal was calculated according to equation 6.2 and a conversion factor of excess charge measured in RW3 to neutron dose (in muscle tissue) of $D_\mathrm{n}/\Delta Q = 30\,\mu\mathrm{Gy/nC}$ (depth of 9 cm RW3) is applied to estimate the extra dose due to the photoneutrons produced in this dose delivery. Table 6.6 shows the results in comparison to the data of the Siemens PRIMUS. The excess signal refers to the same *measured* photon dose of 1.0 Gy for both linacs. The data shows a slightly higher value for the Siemens ONCOR which is, however, in the measurement uncertainty.

In the next step, the phantom was irradiated according to the three treatment plans already used at the Siemens PRIMUS. Again, the excess signal was calculated and converted to neutron dose using the conversion factor above. The signal was related to the same measured photon dose of 72 Gy (40 fractions of 1.8 Gy each) in the PTV. Table 6.7 shows the comparison of the measurement data of the three plans for both linac types.

The Siemens ONCOR delivers a slightly higher photon dose to the OAR than the Siemens PRIMUS. However, for the Siemens ONCOR the neutron dose in the OAR is less than the PTV neutron dose. For the determination of the neutron dose in the PTV and OAR ($D_\mathrm{n,PTV}$ and $D_\mathrm{n,OAR}$) an uncertainty of 15 – 20 % is assumed. Within these uncertainties the data for Siemens PRIMUS and Siemens ONCOR are in full agreement.

The data obtained here are in accordance with published data. Hill and Parsai [48] studied the Siemens ONCOR in a 18 MV photon mode. They determined a source strength of Q

[8] The dose output delivers the same depth-dose distributions and beam profiles.

$= 0.27 \times 10^{12}\ \mathrm{N\,Gy^{-1}}$. Hill [49] compared the source strength to a Siemens PRIMUS in a 18 MV mode, obtaining compatible results, although, the Siemens ONCOR showed a slightly smaller source strength. The authors suppose that this is due to the different room structure, resulting in a different scatter and thermal neutron component (see also Chapter 6.1).

linac type	ΔQ [nC]	D_n [μGy]
Siemens ONCOR	0.53 ± 0.03	16.0 ± 3.2
Siemens PRIMUS	0.52 ±0.03	15.7 ± 2.4

Table 6.6: Excess signal of the MgB/Ar ionisation chamber under reference conditions ($10\times10\,\mathrm{cm^2}$ field, SSD 100 cm, 1 Gy photon dose) in 9 cm depth RW3 for an exposure at the Siemens ONCOR in comparison to Siemens PRIMUS. Uncertainties for ΔQ results from statistical uncertainties, the uncertainties for D_n are estimations taking all systematic errors into account.

linac type	plan	frac.	$D_\mathrm{p,PTV}$ [Gy]	$D_\mathrm{p,OAR}$ [Gy]	$D_\mathrm{n,PTV}$ [mGy]	$D_\mathrm{n,OAR}$ [mGy]
PRIMUS	'box'	40	72.00	38.30	1.15	1.15
ONCOR	'box'	40	72.00	39.20	1.10	0.96
PRIMUS	'cross'	40	72.00	4.07	1.25	1.04
ONCOR	'cross'	40	72.00	4.40	1.10	0.76
PRIMUS	'imrt'	40	72.00	31.10	1.25	1.25
ONCOR	'imrt'	40	72.00	31.84	1.26	1.12

Table 6.7: Comparison of the data for the three treatment techniques for Siemens ONCOR and Siemens PRIMUS. Neutron dose (D_n) is given as dose in muscle tissue and was determined from the excess signal of the MgB/Ar chamber using a conversion factor of 30 μGy/nC.

Concluding, in this chapter the photoneutron contamination of a medical linear accelerator was studied with experimental methods. The idea to use a triple chamber detection system for the dose separation of photons, fast neutrons and thermal neutrons has already been proposed by Schmidt and Hess [5] for a therapeutical fast neutron beam. The ability of a boron coated detector for the determination of the thermal neutron component has been realised by Luedemann *et al.* [6]. Thus, the usage of a detector system utilising three ionisation chambers (TE/TE, Mg/Ar and MgB/Ar chamber) for the application investigated here seemed to suggest itself. However, the fast neutron dose component at a medical linear accelerator is very small and its contribution to the detector response cannot be separated correctly. Therefore the ionisation chamber system was reduced to a paired detector system utilising Mg/Ar and MgB/Ar chamber. This paired chamber system detects the thermal neutron component only. Therefore the calibration factors determined in Chapter 4 cannot be used to obtain the *total*

neutron dose. It was shown that with the paired chamber system (consisting of Mg/Ar and MgB/Ar ionisation chamber) or a TLD system, consisting of two detectors, a detection of photoneutrons in the presence of high-energy photons is generally possible using an albedo technique. The determined neutron detection limits per 1 Gy photon dose are 0.01 μGy for the ionisation chambers and 10 μGy for the TLDs. The poor reproducibility and the low sensitivity of the TLD system prevent reliable measurements in an open field. The sensitivity of the paired chamber system is high enough to measure an excess signal of the MgB/Ar chamber with an accuracy of $\pm 6\,\%$ which is due to thermal neutrons. A Monte Carlo simulation was used to convert the excess signal into total neutron dose. This conversion depends on the penetration depth into the phantom. For large depths (deeper than 8 cm) the conversion factor saturates at a constant value. The neutron dose in several materials can be determined from the excess signal and the MC-simulation assisted procedure with an uncertainty of approximately 20 %.

The paired chamber system allows pointwise measurements. From measurements in a water phantom, it could be deduced that the thermal neutron component measured by the system is field size independent and has a gaseous behaviour. The comparison of different treatment techniques showed no influence on the point of measurement and a dependence on the applied MU per delivered photon dose.

The paired ionisation chamber system was tested at another linac, the Siemens ONCOR. The results are identical with the results for the Siemens PRIMUS. For a total radiotherapy treatment a whole body extra dose due to neutrons of less than 30 mSv was estimated. However, the *relative* neutron dose in the OAR is more significant, because the photon dose is relatively low in these regions. The neutron contamination at low depths (obtained using MC simulations) is also more significant and reaches a value of 0.5 – 1 % of the photon dose.

A possibility to reduce the neutron contamination at a linac was studied by J. Becker [38]. He studied the influence of boron- and lithium-enriched plastic covers for the linac on the neutron distribution by Monte Carlo Simulations. A 20 % or 35 % decrease in the total neutron flux was observed using shieldings with lithium or boron, respectively.

A second idea is to use thermal neutrons for therapeutic purposes by a kind of boron neutron capture. This approach was already suggested by Bevilacqua *et al.* [50] and would require some modifications of the linac by a moderator. Also higher photon energies would be useful then to achieve a sufficient neutron fluence.

Whether the neutron dose of 30 mSv in addition to the therapeutical dose is acceptable for a radiotherapy treatment with 15 MV photons has to be decided by the radiotherapist, considering that even for a total body CT scan 20 mSv are delivered. However, it has to be also considered that other medical linear accelerators can deliver a substantial higher neutron dose (one order of magnitude), especially if higher photon energies are applied (e.g. GE Saturne 43, $Q = 2.4 \times 10^{12}\ \mathrm{N\,Gy^{-1}}$) [28].

The lifetime cancer mortality risk is age-dependent for a lot of organs. This risk is very high for young people and decreases with the age [51]. Therefore it is very important to consider the additional neutron dose in a high-energy photon treatment for young people. Furthermore

for neutrons there is still an ongoing discussion about the biological effectiveness. One must keep in mind that the majority of neutron dose is deposited by the neutrons of relatively high energies. For neutrons of 1 – 2 MeV the NCRP has reported weighting factors of up to 100 [1]. Dennis [52] has summarised experimental neutron RBE data and found maximum values (for low doses) in between 6.44 and 71. Thus, interpretation of neutron equivalent dose is associated with considerable uncertainties.

7 Influence of metal implants

The number of patients with hip protheses undergoing radiotherapy is more and more increasing. It is estimated that 1 – 4 % of all radiotherapy patients have metal prosthetic devices which could affect their therapy. The Task Group 63 of the American Association of Physicists in Medicine (AAPM) identified all problems that are caused by the metal implants in their report [43]. They also turned attention to the neutron production during radiotherapy as the use of photon beams with a maximum energy above 10 MeV is common for the treatment of pelvic tumours. However, the report focuses only on the additional dose from thermal neutron capture processes in the metal protheses. They estimated the extra photon dose due to the protheses to be 0.5 % of the delivered treatment photon dose and therefore clinically negligible. The Task Group Report completely disregards the potential neutron production by the metal protheses if located in the beam path. Wheter the neutron production by implants is indeed negligible, shall be investigated next by Monte Carlo simulations and phantom measurements.

The very common material for hip protheses is titanium. Figure 7.1 (top) shows the cross section of ^{48}Ti for photoneutron production. It can be seen that some photons in the spectrum of the Siemens PRIMUS have an energy above the (γ,n) reaction threshold energy of 11.63 MeV. Therefore there is a probability for the production of additional neutrons in a hip protheses of titanium if the photon beam passes it. ^{48}Ti was selected as its isotopic abundance is 73.8 %. Even though the (γ,n) reaction threshold energy of ^{47}Ti (8.88 MeV) and ^{49}Ti (8.14 MeV) is less, their isotopic abundance is only 7.3 % resp. 5.5 % (see Figure 7.1, middle and bottom) and the contribution to the neutron production for both isotopes is negligible.

In this work, a simplified phantom set-up was used in the measurements performed to model a typical clinical case. This specific set up was also assumed in the Monte Carlo simulations.

Monte Carlo simulations

For the MC simulations, a cylindrical titanium insert with a diameter of 1 cm and a length of 16 cm was included in the RW3 phantom Easy Cube. The middle of the insert was positioned in 5.5 cm depth and the SSD was 91 cm. For the material of the insert, pure ^{48}Ti was assumed. The simulation using MCNPX 2.5.0 code was performed for a $10\times10\,\mathrm{cm}^2$ field with a gantry angle of 0°. A schematic plot of the set up is shown in Figure 7.2. The simulation was performed with the described set up at the Siemens PRIMUS, with the titanium insert and with a set up where the titanium insert was replaced by a RW3 insert. The total neutron dose was tallied in both cases along the central axis and the difference was calculated to estimate the additional neutron dose that is due to the Ti-insert only. The simulation uncertainty is estimated to be ±5 %.

The results plotted in Figure 7.3 show that the included Ti-insert delivers an additional dose component having its maximum close to the insert and falling rapidly with the distance to

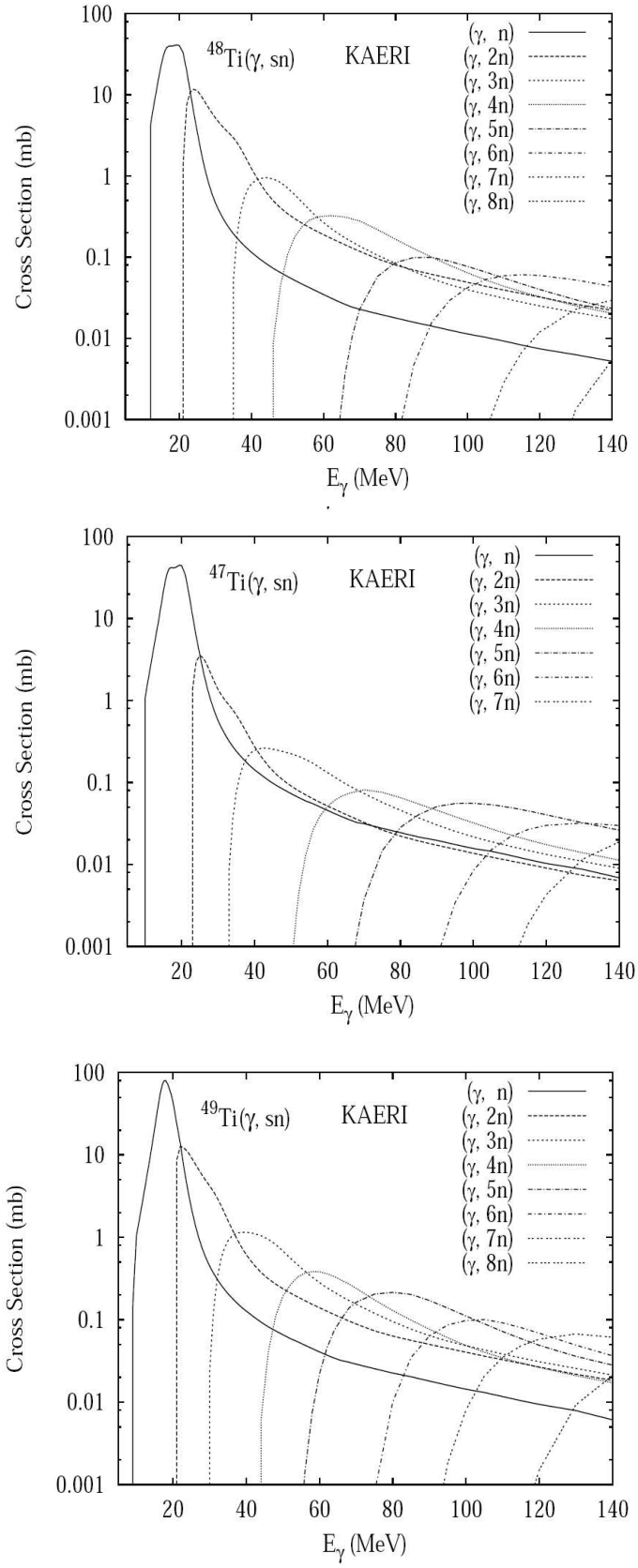

Figure 7.1: Cross sections for photoneutron production in ^{48}Ti (top), ^{47}Ti (middle) and ^{49}Ti (bottom) [53].

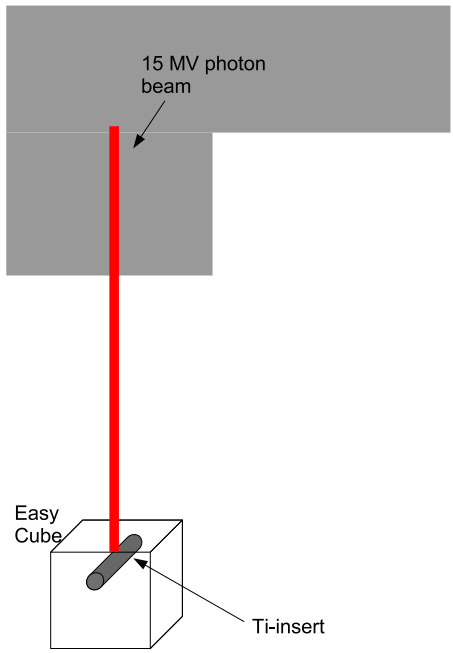

Figure 7.2: Set up of the Easy Cube with included Ti-insert.

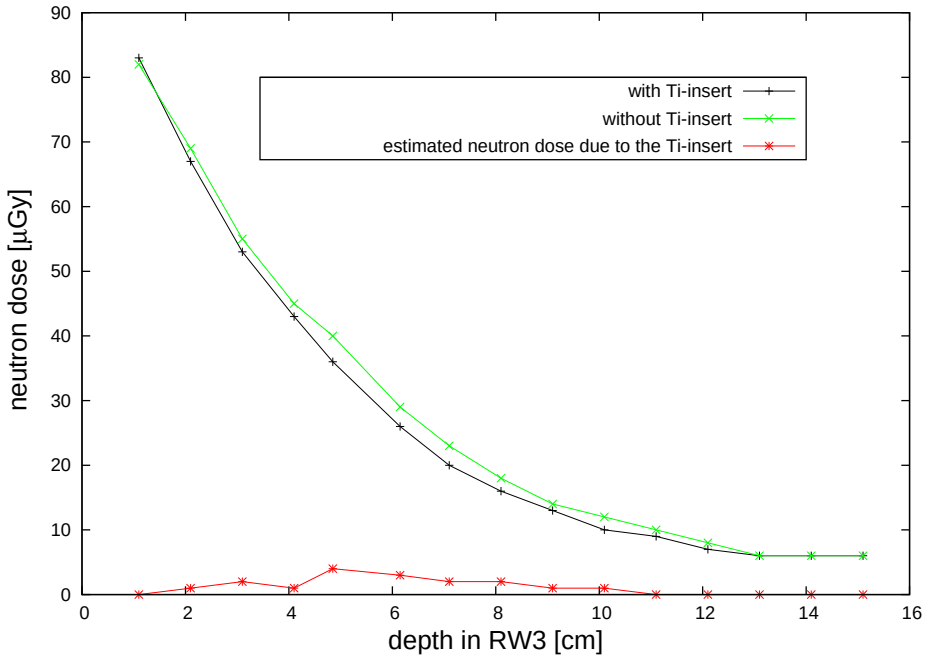

Figure 7.3: Results of the MC simulations. Dose is given as neutron dose in RW3.

the insert. However, the total neutron dose is only increased by approximately 12 % or 4 μGy per 100 MU photon dose. The additional relative neutron dose is 0.0004 % of the photon dose.

Whether this neutron dose can be confirmed by measurements with the paired chamber system was investigated in the next step.

Measurements

The same set up as for the simulations was used for the measurements at the Siemens PRIMUS. However, the Ti-insert used for the measurements has a diameter of 1.6 cm. Measurements were performed with the paired ionisation chamber system in 1 cm distance to the insert. The MC simulations predicted an additional dose due to the insert of 1.5 – 2.4 μGy. The measurements were done using both chambers in the same way as in the simulations.

Neither in front nor behind the insert any additional signal was detected by the ionisation chambers. The signal was within the uncertainty of the measurement and the produced neutrons had obviously energies higher than thermal and could not be detected by the borated Mg chamber.

The result is in accordance with the study of Schneider *et al.* [54]. They studied the additional neutron dose due to metal implants for different materials in a photon and a proton field and observed no influence on the dose detected by CR-39 etch track detectors.

8 Summary and Outlook

This thesis focused on the dosimetry in mixed n,γ fields. The separation of the dose components is common in fields where both, neutron and gamma component, are in the same order of magnitude. In cases where neutrons only contaminate the photon field, the discrimination of both is difficult. In this thesis a dosimetry device for the detection of the photoneutrons in a high-energy photon field at medical linear accelerators was developed, which is usable for mixed n,γ fields with fluence ratios of $\phi_\gamma/\phi_\mathrm{n} \sim 10^3 ... \ 10^5$.

Only a few measurement devices exist for the determination of the neutron component in presence of a substantial higher photon component. In this thesis the suitability of two detector systems was investigated: (i) a triple ionisation chamber system, consisting of a TE/TE, a Mg/Ar and a similar Mg/Ar chamber coated with ^{10}B, and (ii) a paired TLD system, using LiF:Mg,Cu,P TL material enriched with ^{6}Li or ^{7}Li, respectively. Each detector in each system has a different sensitivity to photons and neutrons, but their combination allows for the dose separation in a mixed neutron/photon field.

The ionisation chamber system was calibrated at different photon and neutron sources and the calibration [15] was verified in a study at an epithermal neutron beam of the HFR (Petten, The Netherlands) used for BNCT. In this verification, the borated Mg/Ar ionisation chamber showed a very good suitability for the accurate determination of the thermal neutron component. This chamber is expected to be a useful device for further BNCT dosimetry.

For the photoneutron studies at the linear accelerator, the triple chamber system was substituted by a paired chamber system omitting the TE/TE detector, since the fast neutron component was too low to be separated in the TE/TE detector signal. Using a set up based on a special albedo technique, the neutron detection limits for the paired chamber system and the TLD system were obtained to be 0.01 μGy per 1 Gy photon dose and 10 μGy per 1 Gy photon dose, respectively. The poor reproducibility and the low sensitivity of the investigated TLD system prevent the further use of the system in open high-energy photon fields at a linac [22].

Detailed Monte Carlo simulations of a specific medical linear accelerator, the Siemens PRIMUS, were performed and used as a reference for the experimental investigations with the paired ionisation chamber system at this linac. A source strength of $Q = 0.136 \times 10^{12}$ N Gy^{-1} was determined in these simulations [16].

The neutron calibration of the ionisation chambers obtained at several neutron sources could not be used for the experimental determination of the additional photoneutron dose. Instead a calibration to neutron dose obtained with Monte Carlo simulations was performed. The fast neutron component delivers the highest contribution to the total dose. However, the detector response to these neutrons is very low, the chamber system can detect the thermal

neutron component only. This fact is accounted for in the Monte Carlo simulation based calibration [42]. The use of this calibration allows for the determination of the neutron dose inside the photon field with an uncertainty of 20 % in depths deeper than 8 cm.

The neutron distribution in a water phantom was studied in detail for the Siemens PRIMUS. The chamber system allowed continuous measurements of depth-dose distributions and beam profiles. The measured thermal neutron component showed a gaseous behaviour and is therefore independent of the position. Furthermore the neutron dose showed no dependence on the field size. The study of realistic treatment plans revealed that for the Siemens PRIMUS an additional equivalent neutron dose of less than 30 mSv occurs for a total photon dose of 72 Gy. For a second studied linac, the Siemens ONCOR, identical results were obtained. The neutron dose increases with the number of monitor units per applied photon dose.

The developed paired chamber system can be used at any linac in radiotherapy. Without information about the neutron spectrum, the measurements should be restricted to larger depths in a measurement phantom (albedo technique). There, almost only thermal neutrons are present. This technique allows for fast measurements of the neutron contamination. The recommended measurement depth depends on the used photon energy.

In addition to the linac head components, metal implants of patients inside the beam path give rise to the produced neutrons. The additional dose resulting from metal protheses (e.g. hip protheses) was calculated by Monte Carlo simulations. The neutron dose was found to be less than 0.0005 % of the delivered photon dose and could not be measured with an ionisation chamber system in an experimental verification.

Whether the additional neutron dose of 30 mSv for a total treatment is acceptable for a radiotherapy patient has to be decided by the radiotherapist, evaluating the additional profit and the risk by using a higher photon energy. However, there is an ongoing discussion about the biological effectiveness of neutrons [1], [52] which might be substantial higher than assumed. Thus, the interpretation of neutron equivalent dose is associated with substantial uncertainties. Moreover, the importance increases to determine easily the neutron dose and the need for a suitable detection system becomes larger. Alternatively, one may consider options to reduce the neutron contamination as discussed in [38] or to use the neutrons for therapy as suggested in [50].

To achieve a higher accuracy in the determination of photoneutron doses utilising the paired chamber system, the concept of Bonner spheres could be applied to obtain the whole neutron spectrum at the point of measurement. The Bonner sphere system is a moderated active detector system using several polyethylene spheres of different sizes with detectors (normally paired TLDs) placed in the centre. The spheres are designed to thermalise the faster neutrons before they reach the detector. The use of spheres with different size allows for the discrimination of several energy levels. However, unlike the proposed detector system here, the actual target geometry cannot be accounted for in the Bonner sphere approach and the actual spectrum has to be estimated beforehand.

During proton radiotherapy, secondary neutrons are produced by nuclear interactions in the material in the beam line before and after entering the patient. The neutron contamination

for a spot scanning technique is reported to be a factor of two larger than during photon treatment [55]. The determination of the additional neutron dose in proton therapy, as well as in the radiotherapy with photons, is of vital interest particularly in the organs at risk. A further field of application for the developed detector system could be the neutron detection in proton fields used for therapeutical purposes.

Appendix A

Characteristics of the investigated ionisation chambers

Three ionisation chambers of type IC-30 from Wellhofer Dosimetry, Schwarzenbruck/Germany were used in this work (see Figure A.1): a tissue-equivalent chamber flushed with 1 litre per hour of TE-gas (64.4 vol% CH_4, 32.4 vol% CO_2, 3.2 vol% N_2), a Mg chamber and a boron-coated Mg chamber, both flushed with 1 litre per hour of argon gas. They are denoted as TE/TE, Mg/Ar and MgB/Ar chamber, respectively. All three chambers have a sensitive volume of 0.3 cm^3 and are watertight. The wall thickness of the TE/TE chamber is 2.5 mm, the one of the Mg/Ar and MgB/Ar chamber is 2.0 mm. The MgB/Ar chamber is a modified IC-30 Mg/Ar chamber in which the inner surface is coated with a 3 μm thick boron layer (0.7 mg cm^{-2}) with an isotopic abundance of 92 % ^{10}B (see Figure A.2).

The boron coated Mg chamber was studied by T. Matzen in detail in [56]. No influence of the voltage polarity has been found for the response of the MgB/Ar chamber. Flushing the chamber with argon instead of nitrogen yields a 50 % higher response. The dependence of the chamber response with argon flushing on the voltage shows a plateau in the range of 100 to 250 V. Therefore the chambers are operated with an electrometer with a negative voltage of 250 V for charge collection.

Figure A.1: The three used gas flushed ionisation chambers: TE/TE, MgB/Ar and Mg/Ar chamber. All three chambers are of similar design and dimensions.

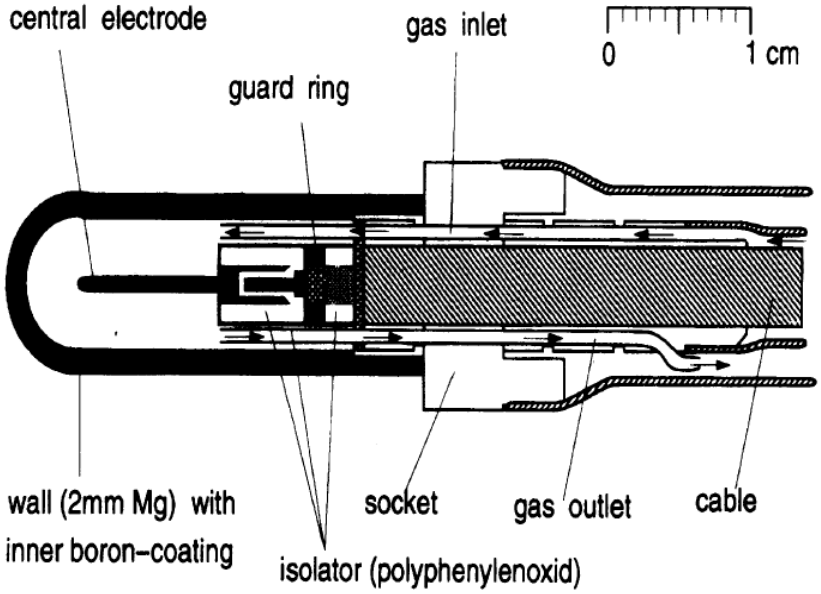

Figure A.2: Cross section of the borated Mg ionisation chamber [6].

Appendix B

Characteristics of the investigated TL detectors

Two TLD types from TLD Poland (Krakow, Poland) were used for the investigations of this thesis. Both have dimensions of 1 mm × 1 mm × 6 mm (square rods) and are named as 'MCP-600D' respectively 'MCP-700D' (see Figure B.1). The names refer to their composition of ^{6}LiF:Mg,Cu,P and ^{7}LiF:Mg,Cu,P, respectively. Table B.1 lists the abundance of ^{6}Li and ^{7}Li for both TLD types. The TL detector materials have an effective atomic number of Z_{eff} = 8.2 and are therefore nearly tissue equivalent ($Z_{eff} \approx 7$).

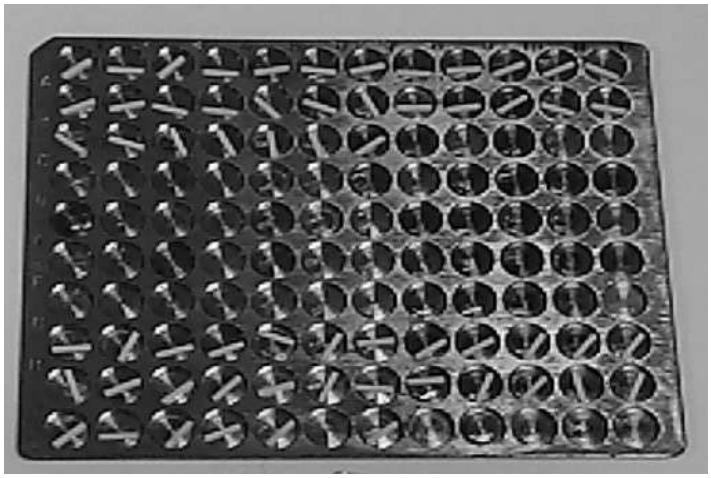

Figure B.1: The TL detector types MCP-600D and MCP-700D from TLD Poland in a stainless steel annealing plate. The dimensions of each TLD are 1 mm × 1 mm × 6 mm.

Detector	^{6}Li (%)	^{7}Li (%)
MCP-600D	95.6	4.4
MCP-700D	0.01	99.9

Table B.1: Composition of ^{6}Li and ^{7}Li for both TLD types.

The TLDs have been characterised in detail during this work and the results were published in [22]. The investigations and their results are also summarised here.

For the determination of the detector signal, the TLDs have to be pre-heated in an oven first (see Chapter 3.3.4). For pre-irradiation and pre-readout annealing of the TLDs, the computer-controlled heating oven PTWO by PTW-Freiburg, Germany was used. Pre-readout heating is performed to delete the low temperature peaks, pre-irradiation heating is done to be sure that there is no signal remaining on the TLD after readout. The oven has three levels to hold annealing plates. Schmuhl *et al.* [57] described a signal variation occurrence dependent on the used level and position on the plate for annealing due to different heating conditions. Therefore only the level in the middle of the oven was used. The TLDs were fixed in holes that are drilled in a stainless steel annealing plate. A maximum of 120 TLDs can be housed at the same time. The position of each TLD on the plate was kept identical for the whole study. A maximum annealing temperature of 240 °C has not been exceeded, since the manufacturer reports a potential sensitivity loss otherwise. The recommended temperature for pre-readout heating was 100 °C and was therefore used here. After cooling down to 42 °C in pre-irradiation and pre-readout heating, the plates were removed from the oven and put on an aluminium plate for further rapid cooling to room temperature. The reading of the detectors were carried out by a computer controlled Harshaw 5500 reader (Thermo Scientific, Waltham, Maryland, USA). The entire TLD signal was integrated to obtain the detector response.

The TLDs were exposed to photon radiation in order to investigate individual response, batch homogeneity, reproducibility, dose linearity, and energy dependence. The irradiations were performed at two Siemens linear accelerators at the University Medical Center Hamburg-Eppendorf. The Siemens MEVATRON MDX-2 delivers photons with a maximum energy of 4 and 6 MeV, the Siemens PRIMUS delivers 6 and 15 MV photons. The detectors were exposed in phantoms made of RW3 (see Chapter 3.4) or PMMA (polymethyl methacrylate, $\rho = 1.170\,\mathrm{g/cm^3}$, H(8.0 %), C(60.0 %), O(32.0 %)). The TLDs were mounted in parallel drilled lines in a horizontal plate perpendicular to the beam axis. Depending on the measurement several plates with dimensions of 30 cm × 30 cm × 1 cm (stacked to a height of 24 cm) or the multipurpose phantom Easy Cube (18 cm × 18 cm × 18 cm, Euromechanics medical GmbH/Schwarzenbruck, Germany) were used.

Glow curve

All 150 TLDs of each type that were used in this study have never been used before and passed first an initialisation procedure of several consecutive irradiation and annealing cycles. The optimal time-temperature profiles (TTP) for reading have been obtained thereafter. With the optimal TTP, the glow curve should be reproducible and all peaks should be displayed in the effective range.

The following time-temperature characteristics were obtained for the reading procedure: pre-heating for 5 s at 150 °C, heating rate 6 °C/s for 15 s and a maximum reading temperature of 240 °C. An external preheating for 10 minutes at 100 °C is performed after irradiation (pre-readout) and an external annealing for 10 minutes at 240 °C after read out (pre-irradiation). For higher heating rates the peaks diffused, the maximum was shifted to lower temperatures, and the glow curve was widened. The use of a higher pre-heating temperature led to a lower pre-peak. With the TTP mentioned above, the best results were obtained. All peaks were displayed and a good reproducibility of the glow curves over several irradiation cycles was achieved. Figures B.2 and B.3 show a typical glow curve for one TLD of each type.

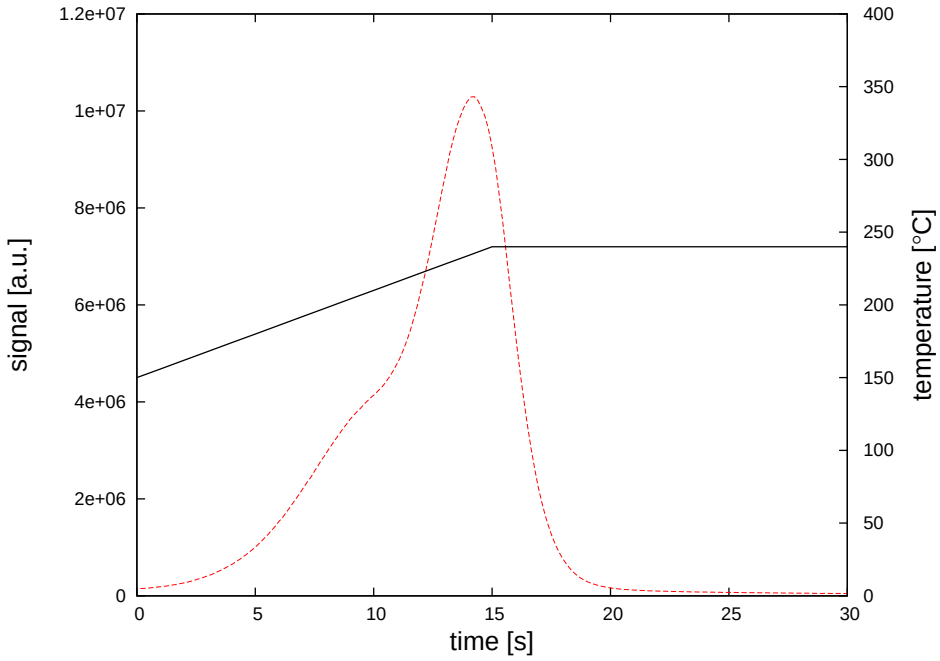

Figure B.2: A typical glow curve for a TLD of type MCP-600D (dashed line). The temperature history is given by the solid line.

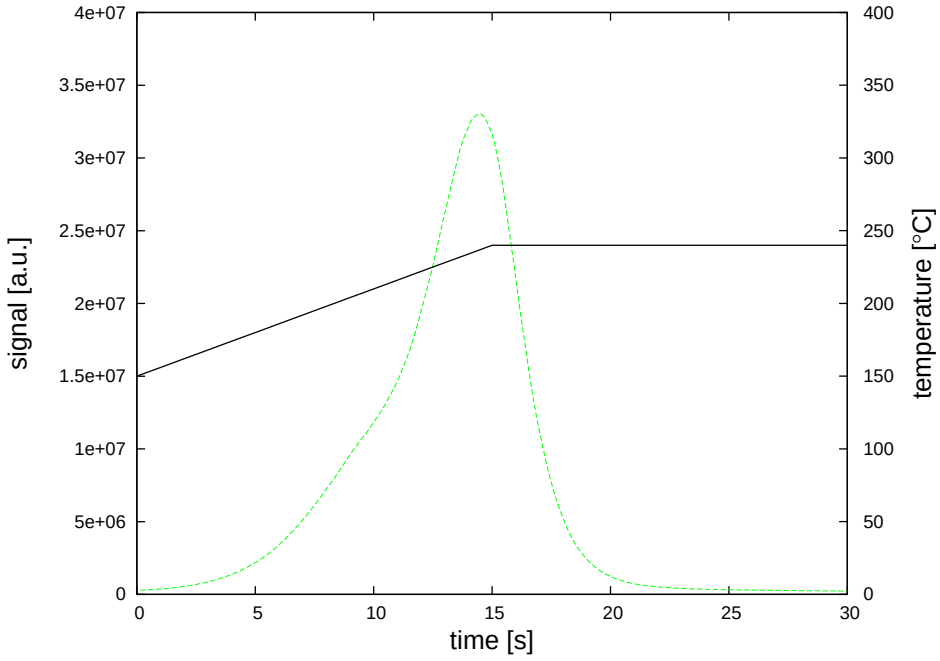

Figure B.3: A typical glow curve for a TLD of type MCP-700D (dashed line). The temperature history is given by the solid line.

Individual response, batch homogeneity and reproducibility

To assess the variability and spread of the responses of the individual detectors, all TLDs were exposed to the same photon dose at 5 cm depth in the plate phantom. 6 MV photons and a $16\times16\,\mathrm{cm}^2$ field were used for irradiation. All TLDs were placed in the middle of the field in the homogeneous dose region. An absolute and a reference ionisation chamber were used to record dose fluctuations. The individual response was determined for each TLD to obtain the batch homogeneity. Due to the wide spread, the individual response was applied as a correction factor to the detector raw data for all further measurements. The irradiation history of each TLD was recorded for several identical irradiation cycles in the PMMA phantom to assess the reproducibility.

The batch homogeneity is within 14 % for MCP-700D and within 22 % for MCP-600D ($2\,\sigma$). Figure B.4 shows the response variations of both TL detector types. The response is normalised to the mean value. The mean value and the value with a confidence level of $2\,\sigma$ for each TLD type are marked.

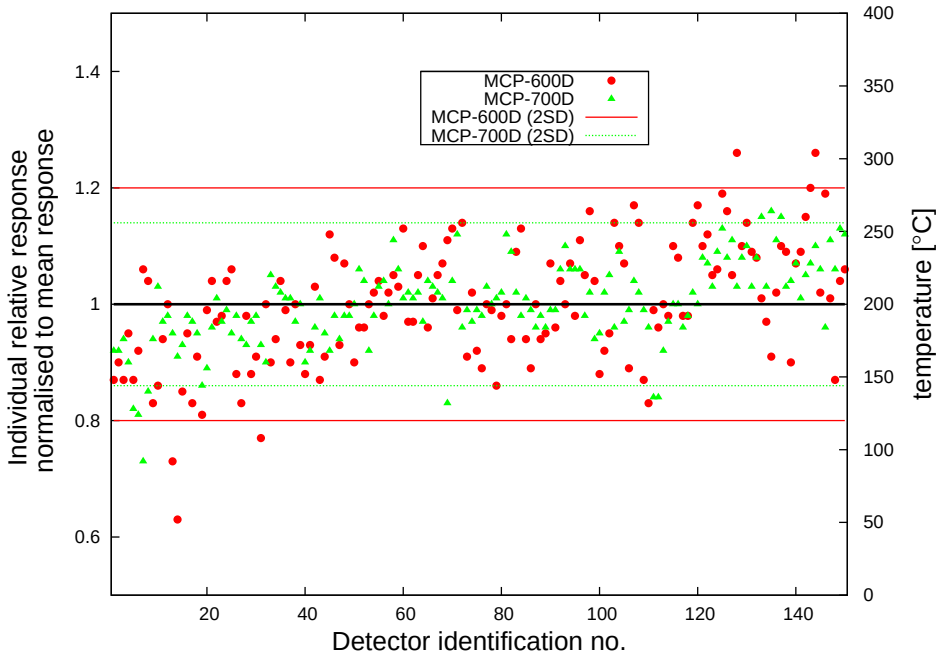

Figure B.4: Relative response of each TLD normalised to the mean value (black solid line) of the type batch. For each type, the value of two standard deviations is marked by two lines.

The reproducibility of the detector signal is defined as the mean value of the standard deviations for all TLDs of one type over several irradiation cycles, taking the individual response of each TLD into account. It was determined to be 5 % and 4 %, respectively, for MCP-600D and MCP-700D, respectively ($1\,\sigma$).

Dose linearity and photon energy dependence

The linearity of the detector response was investigated in a photon dose range up to 4 Gy for 6 MV photons. A subset of 10 TLDs was used for each dose level and the irradiation was performed with the same set up as used for the determination of the individual response. The energy dependence of the detector signal was studied for 4, 6 and 15 MV photons in 5 cm depth in the Easy Cube. A $10 \times 10\,\mathrm{cm}^2$ field was used for the irradiation of 10 TLDs for each energy level. For both checks of dose linearity and energy dependence, the signal of each TLD was corrected for its individual response using the obtained correction factors. Photoneutrons are generated in the accelerator head above a threshold of approximately 7 MeV. The TLD response to these few neutrons can be neglected with respect to the TLD reproducibility. Therefore, for a 15 MV photon field, it was assumed that the response of the MCP-600D is only due to photons.

For both TLD types, the detector response is linear up to 4 Gy. Figures B.5 and B.6 show the TLD signal over the dose D for each TL detector type. A linear relationship of TLD signal and dose can be seen for the measurement data obtained with 6 MV photons. Therefore, for both TLD types, no correction for nonlinearity of the detector response was needed. An obtained signal for 4 and 15 MV photons for one dose value each is also shown in Figures B.5 and B.6 for illustration of the energy dependence. The signal was related to a calibration irradiation at 6 MV taking the individual response of each detector into account. The energy dependence for the MCP-700D is linear within 2 %, for MCP-600D it is within 2 % for 4 and 6 MV. A higher response of 10 % was determined for 15 MV for the MCP-600D. However, large fluctuations from TLD to TLD were present.

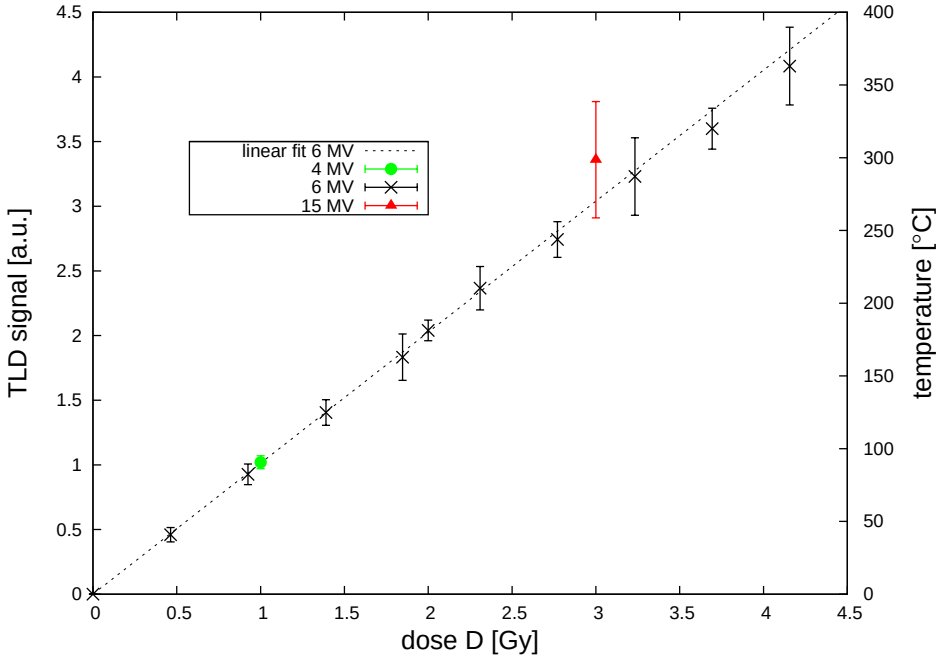

Figure B.5: TLD signal over dose D for MCP-600D. The detector response is linear up to 4 Gy. The energy dependence is within 2 % for 4 and 6 MV and within 10 % for 15 MV.

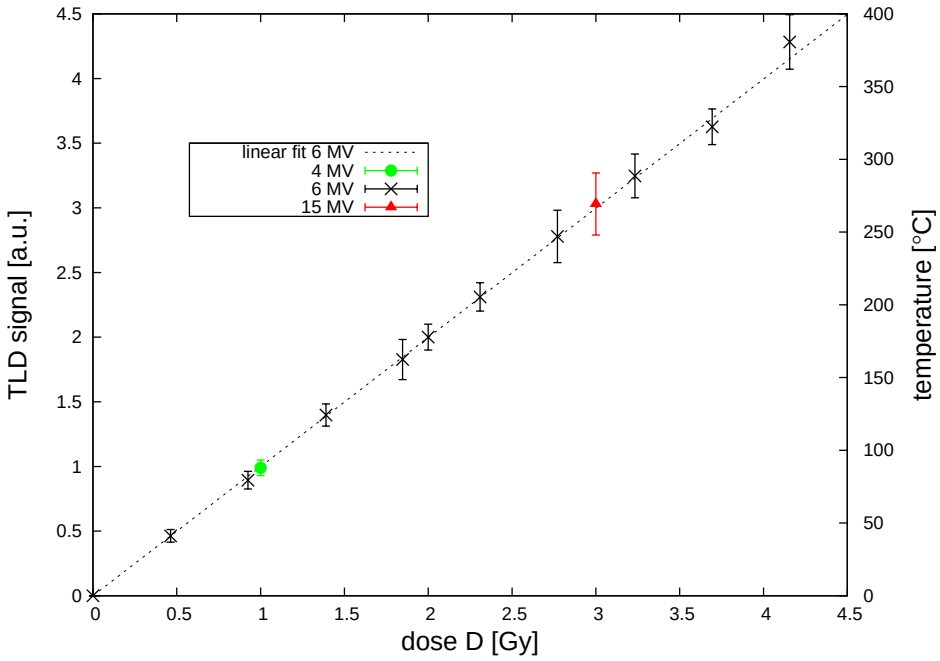

Figure B.6: TLD signal over dose D for MCP-700D. The detector response is linear up to 4 Gy. The energy dependence is within 2 % for 4, 6 and 15 MV.

Bibliography

[1] X.G. Xu, B. Bednarz, and H. Paganetti. A review of dosimetry studies on external-beam radiation treatment with respect to second cancer induction. *Phys Med Biol*, 53(13):R193–R241, Jul 2008.

[2] E.B. Podgorsak. *Radiation Oncology Physics: A Handbook for Teachers and Students*. International Atomic Energy Agency, 2005.

[3] R.M. Howell, M.S. Ferenci, N.E. Hertel, and G.D. Fullerton. Investigation of secondary neutron dose for 18 MV dynamic MLC IMRT delivery. *Med Phys*, 32(3):786–793, Mar 2005.

[4] D.S. Followill, F. Nuesslin, and C.G. Orton. Point/counterpoint. IMRT should not be administered at photon energies greater than 10 MV. *Med Phys*, 34(6):1877–1879, Jun 2007.

[5] R. Schmidt and A. Hess. Triple chamber technique for thermal neutron dose measurements in fast neutron beams. *Strahlentherapie*, 158(10):612–615, Oct 1982.

[6] L. Luedemann, T. Matzen, M. Matzke, R. Schmidt, and W. Scobel. Determination of the thermal neutron flux in a fast neutron beam by use of a boron-coated ionization chamber. *Med Phys*, 22(11):1743–1747, Nov 1995.

[7] W.F.A.R. Verbakel and F. Stecher-Rasmussen. Determination of the gamma-ray component of a neutron beam for medical irradiation applications at the HFR in Petten. *Nuclear Instruments and Methods in Physics Research A*, 451:676–684, 2000.

[8] Joint Research Center European Commission, Directorate-General. High Flux Reactor (HFR) Petten - Characteristics of the installation and the irradiation facilities. Technical report, 2005.

[9] EXFOR database, Nuclear Energy Agency. Nuclear data services database access. http://www.nea.fr/html/dbdata/databases.htm.

[10] International Commission on Radiation Measurements and Units (ICRU). Neutron dosimetry for biology and medicine, Report 26. Technical report, 1976.

[11] International Commission on Radiation Measurements and Units (ICRU). Tissue substitutes in radiation dosimetry and measurements, Report 44. Technical report, 1989.

[12] G. Christ. White polystyrene as a substitute for water in high energy photon dosimetry. *Med Phys*, 22(12):2097–2100, Dec 1995.

[13] P. Andreo, D.T. Burns, K. Hohlfeld, M.S. Huq, T. Kanai, F. Laitano, V. Smyth, and S. Vynckier. Absorbed Dose Determination in External Beam Radiotherapy: An International Code of Practice for Dosimetry based on Standards of Absorbed Dose to Water. Technical report, international atomic energy agency, 2004.

[14] F.M. Waterman, F.T. Kuchnir, L.S. Skaggs, R.T. Kouzes, and W.H. Moore. Energy dependence of the neutron sensitivity of C–CO2, Mg–Ar and TE–TE ionisation chambers. *Phys Med Biol*, 24(4):721–733, Jul 1979.

[15] J. Becker, E. Brunckhorst, A. Roca, F. Stecher-Rasmussen, R. Moss, R. Boettger, and R. Schmidt. Set-up and calibration of a triple ionization chamber system for dosimetry in mixed neutron/photon fields. *Phys Med Biol*, 52(13):3715–3727, Jul 2007.

[16] J. Becker, E. Brunckhorst, and R. Schmidt. Photoneutron production of a Siemens Primus linear accelerator studied by Monte Carlo methods and a paired magnesium and boron coated magnesium ionization chamber system. *Phys Med Biol*, 52(21):6375–6387, Nov 2007.

[17] C.P. Raaijmakers, M.W. Konijnenberg, H.W. Verhagen, and B.J. Mijnheer. Determination of dose components in phantoms irradiated with an epithermal neutron beam for boron neutron capture therapy. *Med Phys*, 22(3):321–329, Mar 1995.

[18] S. Wanwilairat, R. Schmidt, T. Vilaithong, V. Lorvidhaya, and W. Hoffmann. Measurement of the dose components of fast and thermal neutrons and photons from a 0.1 mg 252Cf source in water for brachytherapy treatment planning. *Med Phys*, 27(10):2357–2362, Oct 2000.

[19] R. Boettger, H. Friedrich, and H. Janen. The PTB Thermal Neutron Reference Field at GeNF. Technical report, PTB-N-47, Physikalisch-Technische Bundesanstalt, 2004.

[20] C. Vroegindeweij, F. Stecher-Rasmussen, and R. Huiskamp. A thermal neutron facility for radiobiological studies. *Ann Nucl Energy*, 23:12291238, 1996.

[21] C.P. Raaijmakers, P.R. Watkins, E.L. Nottelman, H.W. Verhagen, J.T. Jansen, J. Zoetelief, and B.J. Mijnheer. The neutron sensitivity of dosimeters applied to boron neutron capture therapy. *Med Phys*, 23(9):1581–1589, Sep 1996.

[22] E. Brunckhorst, X. Sheng, M. Todorovic, J. Becker, and F. Cremers. Characterisation of MCP-600D and MCP-700D thermoluminescence detectors and their applicability for photoneutron detection. *Radiation Protection Dosimetry*, doi: 10.1093/rpd/ncn251, 2008.

[23] W.P. Voorbraak and H. Jaervinen. Recommendations for the Dosimetry of Boron Neutron Capture Therapy (BNCT), Report 21425/03.55339/C. Technical report, NRG, Petten, 2003.

[24] R.D. Rogus, O.K. Harling, and J.C. Yanch. Mixed field dosimetry of epithermal neutron beams for boron neutron capture therapy at the MITR-II research reactor. *Med Phys*, 21(10):1611–1625, Oct 1994.

[25] J. Burmeister, C. Kota, M. Yudelev, and R. L. Maughan. Paired Mg and Mg(B) ionization chambers for the measurement of boron neutron capture dose in neutron beams. *Med Phys*, 26(11):2482–2487, Nov 1999.

[26] C.P. Raaijmakers, M.W. Konijnenberg, and B.J. Mijnheer. Clinical dosimetry of an epithermal neutron beam for neutron capture therapy: dose distributions under reference conditions. *Int J Radiat Oncol Biol Phys*, 37(4):941–951, Mar 1997.

[27] C.P. Raaijmakers, E.L. Nottelman, and B.J. Mijnheer. Phantom materials for boron neutron capture therapy. *Phys Med Biol*, 45(8):2353–2361, Aug 2000.

[28] D.S. Followill, M.S. Stovall, S.F. Kry, and G.S. Ibbott. Neutron source strength measurements for Varian, Siemens, Elekta, and General Electric linear accelerators. *J Appl Clin Med Phys*, 4(3):189–194, 2003.

[29] J.P. Lin, T.C. Chu, S.Y. Lin, and M.T. Liu. The measurement of photoneutrons in the vicinity of a Siemens Primus linear accelerator. *Appl Radiat Isot*, 55(3):315–321, Sep 2001.

[30] J. Pena, L. Franco, F. Gomez, A. Iglesias, J. Pardo, and M. Pombar. Monte Carlo study of Siemens PRIMUS photoneutron production. *Phys Med Biol*, 50(24):5921–5933, Dec 2005.

[31] O. Chibani and C.-M. Charlie Ma. Photonuclear dose calculations for high-energy photon beams from Siemens and Varian linacs. *Med Phys*, 30(8):1990–2000, Aug 2003.

[32] C. Ongaro, A. Zanini, U. Nastasi, J. Rodenas, G. Ottaviano, C. Manfredotti, and K.W. Burn. Analysis of photoneutron spectra produced in medical accelerators. *Phys Med Biol*, 45(12):L55–L61, Dec 2000.

[33] F. d'Errico, R. Nath, L. Tana, G. Curzio, and W.G. Alberts. In-phantom dosimetry and spectrometry of photoneutrons from an 18 MV linear accelerator. *Med Phys*, 25(9):1717–1724, Sep 1998.

[34] G. Tosi, A. Torresin, S. Agosteo, A. Foglio Para, V. Sangiust, L. Zeni, and M. Silari. Neutron measurements around medical electron accelerators by active and passive detection techniques. *Med Phys*, 18(1):54–60, 1991.

[35] R.M. Howell, M.S. Ferenci, N.E. Hertel, G.D. Fullerton, T. Fox, and L.W. Davis. Measurements of secondary neutron dose from 15 MV and 18 MV IMRT. *Radiat Prot Dosimetry*, 115(1-4):508–512, 2005.

[36] C.S. Reft, R. Runkel-Muller, and L. Myrianthopoulos. In vivo and phantom measurements of the secondary photon and neutron doses for prostate patients undergoing 18 MV IMRT. *Med Phys*, 33(10):3734–3742, Oct 2006.

[37] A. Zanini, E. Durisi, F. Fasolo, L. Visca, C. Ongaro, U. Nastasi, K.W. Burn, and J.R.M. Annand. Neutron spectra in a tissue equivalent phantom during photon radiotherapy treatment by LINACS. *Radiat Prot Dosimetry*, 110(1-4):157–160, 2004.

[38] J. Becker. Simulation of neutron production at a medical linear accelerator. Diploma thesis, Department of Physics, University of Hamburg performed at the University Medical Center Hamburg-Eppendorf, Department of Radiotherapy and Radio-Oncology, Medical Physics, 2007.

[39] A.C. Siochi. Description of the Siemens Primus accelerator with the serial number 3362 for simulation in BEAM. *Siemens Medical Systems*, Eletronic data file, 2001.

[40] J. Pena, L. Franco, F. Gomez, A. Iglesias, R. Lobato, J. Mosquera, A. Pazos, J. Pardo, M. Pombar, A. Rodriguez, and J. Sendon. Commissioning of a medical accelerator photon beam Monte Carlo simulation using wide-field profiles. *Phys Med Biol*, 49(21):4929–4942, Nov 2004.

[41] P.H. McGinley and J.C. Landry. Neutron contamination of x-ray beams produced by the Varian Clinac 1800. *Phys. Med. Biol.*, 34:777–83, 1989.

[42] J. Becker, E. Brunckhorst, and R. Schmidt. Investigation of the neutron contamination in IMRT deliveries with a paired magnesium and boron coated magnesium ionization chamber system. *Radiother Oncol*, 86(2):182–186, Feb 2008.

[43] C.S. Reft, R. Alecu, I.J. Das, B.J. Gerbi, P. Keall, E. Lief, B.J. Mijnheer, N. Papanikolaou, C. Sibata, J. Van Dyk, and AAPM Radiation Therapy Committee Task Group 63. Dosimetric considerations for patients with HIP prostheses undergoing pelvic irradiation. Report of the AAPM Radiation Therapy Committee Task Group 63. *Med Phys*, 30(6):1162–1182, Jun 2003.

[44] S.R. Bose, E.D. Brandner, R.N. Selvaraj, S. Bahri, and A. Wu. Measurement of neutron dose for IMRT plans using 23MV photon beam. *Int J Radiat Oncol Biol Phys*, 60:S588–S589, 2004.

[45] R.M. Howell, N.E. Hertel, Z. Wang, J. Hutchinson, and G.D. Fullerton. Calculation of effective dose from measurements of secondary neutron spectra and scattered photon dose from dynamic MLC IMRT for 6 MV, 15 MV, and 18 MV beam energies. *Med Phys*, 33(2):360–368, Feb 2006.

[46] S.F. Kry, M. Salehpour, D.S. Followill, M. Stovall, D.A. Kuban, R.A. White, and I.I. Rosen. Out-of-field photon and neutron dose equivalents from step-and-shoot intensity-modulated radiation therapy. *Int J Radiat Oncol Biol Phys*, 62(4):1204–1216, Jul 2005.

[47] S.F. Kry, M. Salehpour, D.S. Followill, M. Stovall, D.A. Kuban, R.A. White, and I.I. Rosen. The calculated risk of fatal secondary malignancies from intensity-modulated radiation therapy. *Int J Radiat Oncol Biol Phys*, 62(4):1195–1203, Jul 2005.

[48] T. Hill and E. Parsai. SU-FF-T-339: Neutron Fluence Measurements Around the Siemens Oncor Medical Linear Accelerator Utilizing Gold Foil Activation. *Med. Phys.*, 33 (6):2124–2125, 2006.

[49] T.M. Hill. Neutron Fluence Measurements of the Siemens Oncor Linear Accelerator Utilizing Gold Foil Activation. Master's thesis, Medical University of Ohio, 2005.

[50] R. Bevilacqua, G. Giannini, F. Calligaris, D. Fontanarosa, F. Longo, G. Scian, P. Totaro, K. Vittor, E. Vallazza, M. Severgnini, R. Vidimari, G. Bartesaghi, V. Conti, V. Mascagna, C. Perboni, M. Prest, G. Gambarini, S. Gay, M.A. Valente, A. Mozzanica, A. Monti, A. Ostinelli, L. Azario, A. Fidanzio, A. Piermattei, O. Borla, Elisabetta Durisi, F. Fasolo, U. Nastasi, E. Perosino, A. Zanini, and L. Tommasino. PhoNeS: A novel approach to BNCT with conventional radiotherapy accelerators. *Nuclear Instruments and Methods in Physics Research Section A: Accelerators, Spectrometers, Detectors and Associated Equipment*, 572(1):231 – 232, 2007.

[51] D.J. Brenner and C.D. Elliston. Estimated Radiation Risks Potentially Associated with Full-Body CT Screening. *Radiology*, 232: 735-738:735–738, 2004.

[52] J.A. Dennis. The relative biological effectiveness of neutron radiation and its implications for quality factor and dose limitation. *Program. Nucl. Energy*, 20:133–149, 1987.

[53] IAEA-TECDOC 1178. Handbook on photonuclear data for applications cross-sections and spectra. Technical report, IAEA, 2000.

[54] U. Schneider, A. Fiechtner, J. Besserer, and A. Lomax. Neutron dose from prostheses material during radiotherapy with protons and photons. *Phys Med Biol*, 49(9):N119–N124, May 2004.

[55] U. Schneider, St. Agosteo, E. Pedroni, and J. Besserer. Secondary neutron dose during proton therapy using spot scanning. *Int J Radiat Oncol Biol Phys*, 53(1):244–251, May 2002.

[56] T. Matzen. Experimentelle Untersuchungen zur Separierung der Dosisanteile im therapeutisch genutzen Neutronenfeld. Diploma thesis, Department of Physics, University of Hamburg performed at the University Medical Center Hamburg-Eppendorf, Department of Radiotherapy and Radio-Oncology, Medical Physics, 1995.

[57] T. Schmuhl, R. Schmidt, and L. Luedemann. Temperature profiles of an annealing oven and effects on TL signals. *Radiat. Prot. Dosim.*, 71:147–151, 1997.

List of Figures

List of Tables

Abbreviations

AAPM	American Association of Physicists in Medicine
A150	solid water, water equivalent for neutrons
BNCT	boron neutron capture therapy
CAX	central axis
CMS XiO	name of a treatment planning system
CPE	charged particle equilibrium
D	dose
ΔQ	excess charge in a paired detector system
h_{i},k_{i},i_{i}	relative sensitivities of a detector to photons, fast neutron, thermal neutrons relative to the sensitivity to ^{60}Co
HB11	horizontal beam eleven
HFR	High Flux Reactor
IMRT	intensity modulated radiotherapy
K	kerma factor
k_{rel}	relative photon sensitivity of two detectors
LET	linear energy transfer
LFR	Low Flux Reactor
linac	linear accelerator
M	detector reading
MC	Monte Carlo
MCNPX	Monte Carlo code, Monte Carlo n-particle extended
MLC	multi leaf collimator
MU	monitor units
$N_{\mathrm{D,W}}$	calibration factor of measured charge of a detector to dose to water
NRG	Nuclear Research and Consultancy Group
OAR	organ at risc
PDD	percentage depth-dose
PMMA	polymethyl methacrylat=plexi glass
PTV	planning target volume
QA	quality assurance
R	detector signal
RBE	relative biological effectiveness
RW3	a special german solid water, water equivalent for photons and electrons
TE	tissue equivalent
TL	thermoluminescence
TLD	thermoluminescence detector
TTP	time-temperature profile

Acknowledgments

First of all, I want to keep in mind Prof. Rainer Schmidt†, who gave me the possibility to start this work. Unfortunately he cannot witness the finishing of the thesis.

I want to thank my supervisor Dr. Florian Cremers, for giving me the possibility to finish the thesis and for his helpful comments.

Furthermore, I would like to thank Prof. Peter Schleper for acting as co-referee for this thesis and Prof. Wolfgang Scobel for acting as the co-referee for the disputation. I would like to give a special thank to Prof. Scobel for his detailed comments on this work.

Special thanks go to Julian Becker, who performed many of the Monte Carlo simulations, for the good teamwork, the helpful discussions and the nice time.

I am grateful to Antoaneta Roca, Finn Stecher-Rassmussen and the whole BNCT group in Petten, for the possibility to calibrate our ionisation chambers and Reinhard Böttger, for the possibility to measure at the PTB reference field.

I would like to thank Eva Drud, Anja Bartels, Manuel Todorovic and Marcus Fischer for the very enjoyable time.

Thanks to Dr. Elisabetta Gargioni for proof reading of this thesis and Xiaoyuan Sheng and Wiebke Müller-Wichards for the assistance in the TLD investigations.

I would like to thank Dirk Albers for performing the treatment plans and providing images and basic dosimetry data for the studied linac.

Many thanks also to Thomas Schoch, Klaus Lück, Heiko Hilse, Wolfram Rapp, Jasmin Akhavan, Volker Platz, Horst Thurmann, Dr. Bernd Bodmann, Eckardt Thom, Tobias Gauer, René Werner, Daniela Schmitt, Carsten Grohmann, Dennis Bartels and Jan Sokoll for the good time and always willing to help.

I am most grateful to my parents, my sister Aila and my husband Sven for continuous support and being there for me at every time.